FLOW VELOCITY AND TEMPERATURE MEASUREMENTS OF NATURAL CIRCULATION FLOW IN A (FLINAK) MOLTEN SALT LOOP

A Dissertation

by

WILLIAM MILIJA HEADLEY

Submitted to the Graduate and Professional School of
Texas A&M University
in partial fulfillment of the requirements for the degree of

DOCTOR OF PHILOSOPHY

Chair of Committee,	Yassin Hassan
Committee Members,	Rodolfo Vaghetto
	Duy Thien Nguyen
	Kalyan Annamalai
Head of Department,	Michael Nastasi

December 2021

Major Subject: Nuclear Engineering

ABSTRACT

As we push towards a reduction of carbon emissions without sacrificing reliability and safety, advanced applications of molten-salt technology are currently being considered for use. Many previous studies have focused on the physical properties of the salts along with the heat-transfer characteristics, but in this work for the first time flow visualization techniques will be applied to a flowing molten salt system. High-fidelity flow visualization measurements are used to provide local fluid flow behavior. Laser based visualization techniques, such as Particle Image Velocimetry (PIV), are utilized to generate spatially-resolved fluid velocity profiles, and other local parameters. High-fidelity experimental data is also important to validate advanced computational tools, and to substantiate existing empirical models. Various molten salt compositions are being considered for use in advanced energy production systems such as solar, thermal energy storage, and nuclear power. Due to the extremely high operating temperature of molten-salt systems, the application of laser- based visualization techniques is very challenging. In this work, local flow velocity measurements were successfully conducted for FLiNaK molten salt in a natural circulation flow loop operating at 650°C. In addition to PIV, temperatures of the liquid salt and pipe walls were recorded by a series of thermocouples located at different location within the test section. Two-dimensional fluid velocity profiles were generated, and along with temperature data, used to calculate important fluid parameters. To the authors knowledge, this work is first of a kind, and demonstrates the applicability of laser-based flow visualization techniques in high-temperature environments typical of molten salt systems.

ACKNOWLEDGMENTS

I need to start off by thanking my advisors, Dr. Hassan, Dr. Vaghetto, Dr. Nguyen for their patience and guidance through the last few years. From welcoming into the laboratory as an undergraduate student, to encouraging the transition to graduate school, I appreciate their guidance.

When I look back on my time at the lab, I find it unbelievable the group of students that I have had the pleasure to share this space with. It's been a blast to work with so many great folks who have not only helped my development as a professional, but more importantly as a person. Some of my greatest friends came from this experience, and I will always cherish that. I need to thank Dr. Nolan Goth, Dr. Mason Childs, Dr. Nicolas Quintanar, Dr. Se Ro Yang, and Dr. Robert Muyshondt.. and the soon to be Drs. Ojasvin Arora, Blake Maher, Noah Sutton, Daniel Orea, and Rey Chavez. I couldn't have done it without y'all.

I would not be where I am, or who I am without my family. In particular, I need to start with my parents Rick and Dorothy Headley, and my brother Rich. My grandmother Dosta Dudich continues to be one of the strongest and most important people in my life, she inspires me every single day. And finally my uncles George Dudich and Mike Stolte. All of y'all have helped me along this journey. Thank you for being my role models, I love y'all.

CONTRIBUTORS AND FUNDING SOURCES

Contributors

This work was supported by a dissertation committee chaired by Professor Yassin Hassan of the Departments of Nuclear Engineering and Mechanical Engineering, consisting of Professors Duy Thien Nguyen, and Rodolfo Vaghetto of the Department of Nuclear Engineering and Professor Kalyan Annamalai of the Department of Mechanical Engineering.

Data collection was performed by the student and assisted in part by Se Ro Yang, a Postdoctoral Researcher in the Department of Nuclear Engineering. All other work, including data analysis and discussion was completed by the student independently.

Funding Sources

Graduate study was supported by a research assistantship from the Department of Nuclear Engineering at Texas A&M University.

NOMENCLATURE

Acronyms

2D2C	Two-Dimension Two-Component
AHTR	Advanced High-Temperature Reactor
ANP	Aircraft Nuclear Propultion
ARE	Aircraft Reactor Experiment
CFD	Computational Fluid Dynamics
CMOS	Complimentary Metal-Oxide-Semiconductor
CO2	Carbon Dioxide
DAQ	Data Acquisition
DOE	U.S. Department of Energy
DFT	Discrete Fourier Transform
DNS	Direct Numerical Simulation
DWO	Discrete Window Offset
FLiNaK	Ternery Eutectic Salt Mixture of LiF-NaF-KF
FLiBe	Eutectic Salt Mixture of LiF-BeF
FFT	Fast Fourier Transform
FHR	Fluoride-Salt-Cooled High-Temperature Reactor
GEN-IV	Generation 4 reactor concepts
HTGR	High-Temperature Gas-Cooled Reactor
LES	Large-Eddy Simulation
LMFBR	Liquid Metal Fast Breeder Reactor
LOCA	Loss of Coolant Accident
LWR	Light water Reactor

MIR	Matched-Index of Refraction
MSR	Molten Salt Reactor
MSRE	Molten Salt Reactor Experiment
NRC	Nuclear Regulatory Commission
ORNL	Oak Ridge National Laboratory
PIV	Particle Image Velocimetry
POD	Proper Orthogonal Decomposition
PRANA	PIV Research and Analysis
PSD	Power Spectrum Density
RPC	Robust Phase Correlation
RAM	Random Access Memory
RANS	Reynolds-averaged Navier-Stokes
RMS	Root-Mean-Square
SAM	System Analysis Module
SFR	Sodium Fast Reactor
TRACE	TRAC/RELAP Advanced Computational Engine
UOD	Universal Outlier Detection
V&V	Verification & Validation

Variables

L	Characteristic Length
D_H	Hydraulic Diameter
KE	Kinetic Energy
ρ_f	Fluid Density
ρ_p	Particle Density
A_F	Flow Area
tau_f	Fluid Response Time
tau_p	Particle Response Time
N_Ω	Vortex Population
$I_n(x)$	Image Intensity Field
μ_A	Mean of Vortex Area
σ_A	Standard Deviation of Vortex Area
ν	Kinematic Viscosity
Re	Reynolds Number
St	Stokes Number
μ	Viscosity
$\boldsymbol{\omega_z}$	Vorticity in the z-plane
$u_i(x_i, t)$	Instantaneous Velocity Field
$\omega_i(x_i, t)$	Instantaneous z-vorticity Field
e_x	PIV Statisitcal Uncertaity of x
$\mathbf{x}$	Spatial Discretization Vector

TABLE OF CONTENTS

Page

ABSTRACT ii

ACKNOWLEDGMENTS iii

CONTRIBUTORS AND FUNDING SOURCES iv

NOMENCLATURE v

TABLE OF CONTENTS viii

LIST OF FIGURES x

LIST OF TABLES xiv

1. INTRODUCTION 1
   - 1.1 Motivation 1
   - 1.2 Previous Work & Literature Review 3

2. SCOPE AND OBJECTIVES 5

3. TEST FACILITY 6
   - 3.1 Flow Loop 7
   - 3.2 Test Section 11
   - 3.3 Instrumentation 16
   - 3.4 Salt Operations 18

4. EXPERIMENTAL METHODS 21
   - 4.1 Analysis Techniques & Governing Equations 21
     - 4.1.1 Reynolds Decomposition 23
     - 4.1.2 Proper Orthogonal Decomposition 24
     - 4.1.3 Frequency Analysis 25
     - 4.1.4 Vortex Characterization 26
   - 4.2 Particle Image Velocimetry 26
     - 4.2.1 Convergence 28
     - 4.2.2 Measurement Uncertainty 29
   - 4.3 Workflow 30
     - 4.3.1 Data Collection 30

4.3.2 Pre-Processing 31
4.3.3 Processing 31

5. MEASUREMENTS 33

5.1 Data Set 3 36
5.1.1 Data Set 3.1 Steady State, Onset of flow instability 36
5.1.2 Data Set 3.2 Transient Evolution 39
5.1.3 Data Set 3.3, Established Unstable Flow 42
5.1.4 Data Set 3 Combined Results 45
5.2 Data Set 4 51
5.2.1 Data Set 4.1 Initially Steady 51
5.2.2 Data Set 4.2 Evolution 54
5.2.3 Data Set 4.3 Established Unstable Flow 57
5.2.4 Data Set 4 Combined Results 60
5.3 Data Set 5 66
5.3.1 Data Set 5.1 Initially Steady 66
5.3.2 Data Set 5.2 Evolution 69
5.3.3 Data Set 5.3 Established Unstable Flow 72
5.3.4 Data Set 5 Combined Results 75

6. CONCLUSIONS 82

REFERENCES 83

LIST OF FIGURES

FIGURE Page

3.1 An overview of the entire experimental setup, (a) The laser and traverse system, (b) the test loop, (c) the camera and traverse setup. 6

3.2 (a) The flow loop prior to trace heating installation and insulation, (b) and the bare melting chamber. 7

3.3 Trace heating installation prior to insulation. 9

3.4 (a) The visualization window closed with insulation and (b) shows the insulation configuration during imaging. 10

3.5 Visualization test section shown (a) disassembled, (b) the quartz penetration in the bored through fitting, and (c) the probe insertion for TP4 and TP5. 12

3.6 Failed test section mounting variations, (a) Initial clamping method, (b) new test section, addition of clamps, (c) adjustable metal bands added. 14

3.7 Final mounting configuration, (a) Test Section, with trace heating, lower clamp, and flexible upper connection. The flexible pipe connection used shown bare (b), and (c) with trace heating. The adjustable lower mounting clamp (d) 15

3.8 The positions and labels of the thermocouple probes shown on (a) insulated loop. and (b) a simplified model of loop with arrows depicting direction of the flow 17

3.9 Model of PIV component configuration (a) planar laser, (b) test section, (c) the camera 18

3.10 The progression of the FLiNaK preparation. (a) Powdered FLiNaK components and the tube of borosilicate particles, (b) the FLiNaK powder loaded into crucibles and placed in oven, (c) the resulting FLiNaK ingot and porcelain crucible, (d) FLiNaK ingots in the melting chamber. 19

5.1 Summary of the data sets and the various cases included in this dissertation. 33

5.2 Full facility temperature probe response for entire test test on 02-03-2021 34

5.3 Velocity and Vorticity fields for data set 3.1 averaged over a 0.25s span. 5.3a begins at insulation removal, and 5.3b, 5.3c show different times during the video. 36

5.4 ω_z vorticity field reconstruction using N POD modes, shown with the original instantaneous vorticity snapshot at $t = 50.125s$ for Data Set 3.1. 38

5.5 RMS u and v velocity components and Reynolds Shear Stress for Data Set 3.1. 39

5.6 Velocity and Vorticity fields for data set 3.2 averaged over a 0.25s span. 5.6a begins at insulation removal, and 5.6b, 5.6c show different times during the video. 40

5.7 ω_z vorticity field reconstruction using N POD modes, shown with the original instantaneous vorticity snapshot at $t = 50.125s$ for Data Set 3.2. 41

5.8 RMS u and v velocity components and Reynolds Shear Stress for Data Set 3.2. 42

5.9 Velocity and Vorticity fields for data set 3.3 averaged over a 0.25s span. 5.9a begins at insulation removal, and 5.9b, 5.9c show different times during the video. 43

5.10 ω_z vorticity field reconstruction using N POD modes, shown with the original instantaneous vorticity snapshot at $t = 50.125s$ for Data Set 3.3. 44

5.11 RMS u and v velocity components and Reynolds Shear Stress for Data Set 3.3. 45

5.12 Temperature probe response for dataset 3, which was taken as a subset of the test on 02-03-2021 46

5.13 POD mode energy distribution for Data Set 3. 5.13a shows the cumulative energy as a function of POD mode, while 5.13b shows the kinetic energy spectrum of the POD modes. 47

5.14 PSD computed from the POD temporal coefficients $\zeta_1, \zeta_2, \zeta_3$ and the $-\frac{5}{3}$ power dissipation slope shown for the ω_z vorticity fields obtained for Dataset 3 48

5.15 Vortex centroid locations for Data Set 3 49

5.16 Vortex area distribution for Data Set 3 50

5.17 Velocity and Vorticity fields for data set 4.1 averaged over a 0.25s span. 5.17a begins at insulation removal, and 5.17b, 5.17c show different times during the video. 52

5.18 ω_z vorticity field reconstruction using N POD modes, shown with the original instantaneous vorticity snapshot at $t = 50.125s$ for Data Set 4.1. 53

5.19 RMS u and v velocity components and Reynolds Shear Stress for Data Set 4.1. 54

5.20 Velocity and Vorticity fields for data set 4.2 averaged over a 0.25s span. 5.20a begins at insulation removal, and 5.20b, 5.20c show different times during the video. 55

5.21 ω_z vorticity field reconstruction using N POD modes, shown with the original instantaneous vorticity snapshot at $t = 50.125s$ for Data Set 4.2. 56

5.22 RMS u and v velocity components and Reynolds Shear Stress for Data Set 4.2. 57

5.23 Velocity and Vorticity fields for data set 4.3 averaged over a 0.25s span. 5.23a begins at insulation removal, and 5.23b, 5.23c show different times during the video. 58

5.24 ω_z vorticity field reconstruction using N POD modes, shown with the original instantaneous vorticity snapshot at $t = 50.125s$ for Data Set 4.3. 59

5.25 RMS u and v velocity components and Reynolds Shear Stress for Data Set 4.3. 60

5.26 Temperature probe response for dataset 4, which was taken as a subset of the test on 02-03-2021 61

5.27 POD mode energy distribution for Data Set 4. 5.27a shows the cumulative energy as a function of POD mode, while 5.27b shows the kinetic energy spectrum of the POD modes. 62

5.28 PSD computed from the POD temporal coefficients $\zeta_1, \zeta_2, \zeta_3$ and the $-\frac{5}{3}$ power dissipation slope shown for the ω_z vorticity fields obtained for data set 4 63

5.29 Vortex centroid locations for Data Set 4 64

5.30 Vortex area distribution for Data Set 4 65

5.31 Velocity and Vorticity fields for data set 5.1 averaged over a 0.25s span. 5.31a begins at insulation removal, and 5.31b, 5.31c show different times during the video. 67

5.32 ω_z vorticity field reconstruction using N POD modes, shown with the original instantaneous vorticity snapshot at $t = 50.125s$ for Data Set 5.1. 68

5.33 RMS u and v velocity components and Reynolds Shear Stress for Data Set 5.1. 69

5.34 Velocity and Vorticity fields for data set 5.2 averaged over a 0.25s span. 5.34a begins at insulation removal, and 5.34b, 5.34c show different times during the video. 70

5.35 ω_z vorticity field reconstruction using N POD modes, shown with the original instantaneous vorticity snapshot at $t = 50.125s$ for Data Set 5.2. 71

5.36 RMS u and v velocity components and Reynolds Shear Stress for Data Set 5.2. 72

5.37 Velocity and Vorticity fields for data set 5.3 averaged over a 0.25s span. 5.37a begins at insulation removal, and 5.37b, 5.37c show different times during the video. 73

5.38 ω_z vorticity field reconstruction using N POD modes, shown with the original instantaneous vorticity snapshot at $t = 50.125s$ for Data Set 5.3. 74

5.39 RMS u and v velocity components and Reynolds Shear Stress for Data Set 5.3....... 75

5.40 Temperature probe response for data set 5, which was taken as a subset of the test on 02-03-2021 76

5.41 POD mode energy distribution for Data Set 5. 5.41a shows the cumulative energy as a function of POD mode, while 5.41b shows the kinetic energy spectrum of the POD modes. 77

5.42 PSD computed from the POD temporal coefficients $\zeta_1, \zeta_2, \zeta_3$ and the $-\frac{5}{3}$ power dissipation slope shown for the ω_z vorticity fields obtained for data set 5 78

5.43 Vortex centroid locations for Data Set 5 79

5.44 Vortex area distribution for Data Set 5 80

LIST OF TABLES

TABLE Page

3.1 Heating elements and power control methods used to provide power to loop.......... 10

3.2 Physical Properties of FLiNaK over experiment temperature span..................... 20

4.1 Quantities used to calculate the Stokes number for the experiment..................... 28

4.2 PRANA PIV processing settings 32

5.1 Fluid data for datasets 3,4,5 35

5.2 Statistical results vortices identified from PIV velocity vectors for Data Set 3 49

5.3 Uncertainty of first and second order statistics for data set 3........................... 51

5.4 Statistical results vortices identified from PIV velocity vectors for Data Set 4 62

5.5 Uncertainty of first and second order statistics for data set 4........................... 66

5.6 Statistical results vortices identified from PIV velocity vectors for Data Set 5 79

5.7 Uncertainty of first and second order statistics for data set 5........................... 81

1. INTRODUCTION

This chapter aims to introduce the concepts that are covered in this dissertation. The motivation for the demonstration of non-intrusive flow visualization techniques is presented in Section 1.1. The relevant literature is reviewed in Section 1.2 and includes the early work in the field of molten salt research, along with current efforts.

1.1 Motivation

With the current society wide push towards the reduction in CO2 emissions, development of advanced clean energy technologies is accelerating. Since nuclear power has reliably and safely contributed a dominant portion of the clean electricity in the United States for decades, a new generation of nuclear power systems commonly referred to as Generation-IV (Gen-IV) are being designed with additional design parameters such as; high outlet temperatures, increased thermal efficiency, and passive safety. Molten Salt Reactors (MSR) systems are currently among the most promising, and actively researched to accomplish these goals[1][2]. The most common fluids used in contemporary reactor systems are water, helium, and liquid sodium. Traditional water systems require pressurized systems, and have modest top-end temperatures, and required significant pressurization. The Westinghouse AP1000 is currently the most advanced light water reactor (LWR) being built in the United States of America (USA) and the design outlet temperature of the primary coolant is 321°C, at a pressure of 2250 psia [3], whereas the Advanced High-Temperature Reactor (AHTR) concept is designed to provide 750°C and 1000°C heat for electricity and industrial applications at atmospheric pressure [4]. High-Temperature Gas Reactor (HTGR) systems also reach these extreme temperatures but like LWR systems they must be highly pressurized which dramatically increases the cost associated with construction, and challenges the push towards passive safety. Liquid Metal Fast Breeder Reactors (LMFBR), specifically Sodium Fast Reactors (SFR) offer another alternative owing to their elevated temperature output and atmospheric pressure, but elemental sodium is violently reactive with air, and this greatly complicates the design phase to ensure safe operation.

In order to effectively bring MSR's to market, the industry must be able to demonstrate both the safety and economics of these systems. The economic forces driving the deployment of nuclear reactors do not follow any predictable or logical behavior, and therefore will be covered in this dissertation. The comprehensive safety analysis is regulated by the US Nuclear Regulatory Commission (NRC), which relies on many computational tools to verify the performance of the proposed reactor designs. The analysis of thermal-hydraulic performance uses both system level codes such as Argonne National Laboratory's (ANL) System Analysis Module (SAM), and the NRC's TRAC/RELAP Advanced Computational Engine (TRACE), or increasingly demanding computational fluid dynamics (CFD) models such as large-eddy simulations (LES) or even direct numerical simulation (DNS) to understand decreasing sized phenomena[5]. These advanced models of the fluid behavior provide high-spatial resolution of their numerical solutions but need to undergo a validation and verification (V&V) process to confirm the applicability of the models to the real-world. This is typically accomplished by performing benchmark experiment, modeling the situation, and then updating the empirical models. Unfortunately, there exists large gaps in the experimental data leaving existing computational tools not well suited to model the MSR systems. This work aims to advance experimental capability in support of efforts to improve tools such as SAM or TRACE for complex flow phenomenon, specifically molten salt applications [6][7][8],

Experimental determination of a flow field is commonly achieved using PIV, a non-intrusive optical measurement allows for the identification and study of coherent turbulent structures in the flow [9]. This method has been successfully deployed in a variety of nuclear reactor related geometries including LWR rod lattices, pebble-beds, and wire-wrapped rods for LMFBR's, [10][11][12], and advanced heat exchanger studies such as sphere-packed pipe and helical-coil steam generator [13][14]. Since PIV is an optical measurement, visual access to the test-region must be maintained. To facilitate this, most studies are performed at room temperature with optically clear test sections made of glass or plastic and fluids are selected such that the index of refraction matches, allowing PIV to produce high-fidelity field data for complex flows, including sub-channels.

1.2 Previous Work & Literature Review

The work at Oak Ridge National Laboratory (ORNL) beginning in the early 1950s with the Aircraft Nuclear Propulsion (ANP) program which sought to develop a molten salt reactor for aircraft. The ANP culminated in 1954 with operation of the Aircraft Reactor Experiment (ARE) [15]. The ARE was a liquid fluoride salt (NaF-ZrF-UF_4) cooled system that operated at 2.5 MW_{th}, and provided fuel outlet temperatures up to 882 °. The reactor heat was fed into a helium gas-cooled secondary side, much of the work . Following the successful operation of the ARE, a larger system called the Molten Salt Research Experiment (MSRE) was designed and constructed[16]. The MSRE utilized a different salt mixture (LiF-BeF_2-ZrF-UF_4), which is the commonly researched salt mixture FLiBe, with trace amounts of ZrF. The secondary for the MSRE was a FLiBe loop, so the development of salt-salt heat exchangers was begun for the MSRE program. Between 1965 and 1969, the MSRE operated for nearly 1.5 years at an operating temperature of 650 °. A third reactor, the Molten Salt Breeder Reactor (MSBR) was designed but never operated. Unfortunately, the molten-salt program was cancelled in 1973, and this effectively ended the 20 years of molten salt work at ORNL, which would resume in a few decades.

Recent work on the development of Molten Salt technologies has enjoyed large interest in a variety of fields, and is well introduced in a comprehensive review published at the beginning of the resurgence of molten salt systems[17]. The application of natural convection systems to nuclear reactors has been studied for decades [18][19][20][21], and the thermo-physical properties of properties of fluoride molten salts allow for their use in natural circulation heat-transfer systems. Due to the very high temperature environment that these salts require, most of the experimental natural circulation studies have used temperature measurements to infer the fluid velocity, and the heat-transfer quantities[22][23]. Visualization studies have been performed using molten salts initially being static cells that either studied the freezing and melting behavior of the salts, or enclosed cells that studied the fluid convection [24][25]. Since molten salts are being explored for both primary reactor applications as well as secondary applications, the design and study of molten salt heat exchangers is also a vibrant field [26][27]. To support the design and optimization of heat removal systems, the fluid properties of molten salts including; corrosion, mass transfer, and heat transfer, have been extensively studied with both experimental and computational tools[28][29][30][31][32].

Innovative studies have been performed at Texas A&M University where a forced convection loop has been outfitted with a fiber-optic measurement system that has been leveraged to measure the transient fluid wave-front shape, along with the fluid velocity[33]. In addition to the natural circulation loop covered in this dissertation, to the authors knowledge the only two-phase molten salt visualization loop is also at Texas A&M, where researched built a facility that introduces helium into a static column of FLiNaK molten salt, and PIV is used to study the bubble behavior in the salt column[34].

2. SCOPE AND OBJECTIVES

This experimental work outlines a method for novel data collection, and characterizes a non-isothermal transient flow condition in a molten salt natural convection loop. This study supports the design and improvement of molten salt systems by providing velocity field data for a molten salt under flow conditions using well established 2D2C PIV. This field data may be utilized for the validation of system level codes, or advanced computational tools such as CFD. The primary objectives of this work are summarized as:

1. Design and construct a flow loop, to provide flow optical access to FLiNaK molten salt in a natural circulation flow condition.

2. Using lessons learned, develop a repeatable preparation and mounting procedure allowing for the successful installation and use of a glass pipe-section in a metal flow loop.

3. Demonstrate the applicability of PIV on a high-temperature flow loop by collecting full-field velocity measurements, and characterizing the fluid flow.

4. Perform analysis to characterize complex flow phenomenon and identify experimental improvements for future studies.

An iterative process was followed to modify the initial design of the mounting and installation procedure to the point where the glass test-section could survive the 650°C temperature gradient. Experimental data was produced for a dramatic thermal transient, showing complex flow phenomenon.

The analysis of the experimental data produced shows the applicability of the PIV method to molten salt systems, and will allow for future studies to be undertaken which study more prototypical flow conditions. This will aid in the design of reactor systems, heat-exchangers, and other systems such as solar and thermal energy storage.

3. TEST FACILITY

This chapter includes a description of the experimental facility and the iterative process of construction and shakedown testing, some of the experimental challenges associated with the experimental conditions, and a discussion on the fluid used in the loop and its selection. Figure 3.1 shows the installed experimental facility, with the laser, camera and the insulated loop.

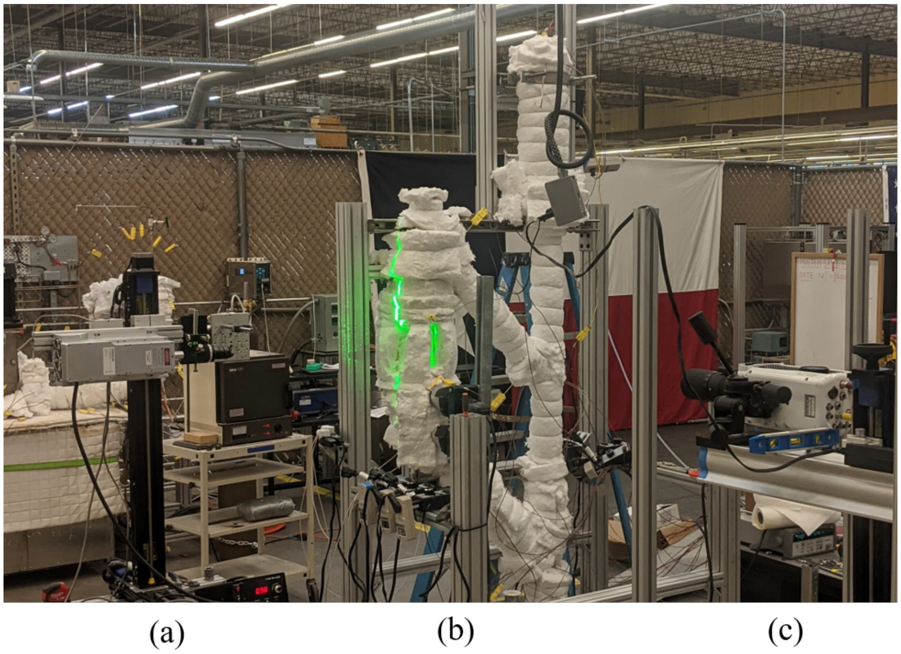

Figure 3.1: An overview of the entire experimental setup, (a) The laser and traverse system, (b) the test loop, (c) the camera and traverse setup.

Section 3.1 provides a description of the overall flow loop, along with the filling and draining equipment. The visualization test section is explored in Section 3.2, which also includes the development of the mounting methodology. The instrumentation used in this study is reviews briefly in Section 3.3. The procedure for the salt preparation, and its material properties is considered in Section 3.4.

3.1 Flow Loop

The flow loop shown in Figure 3.1(b), is equipped with a melting chamber, drain valve, distributed trace heating, and localized heat guns below the test section. and in a visualization region on a vertical leg. The loop consists of 1/2" sch 40, 316 stainless steel piping welded into a rhombus shape, and each of these legs is 2 ft long. The angled piping is at 45° angles, and this is accomplished by welding 45° pipe elbow on each side of the diagonal sections to vertically oriented pipe tees. Figure 3.2(a) shows the main flow loop with the insulation removed.

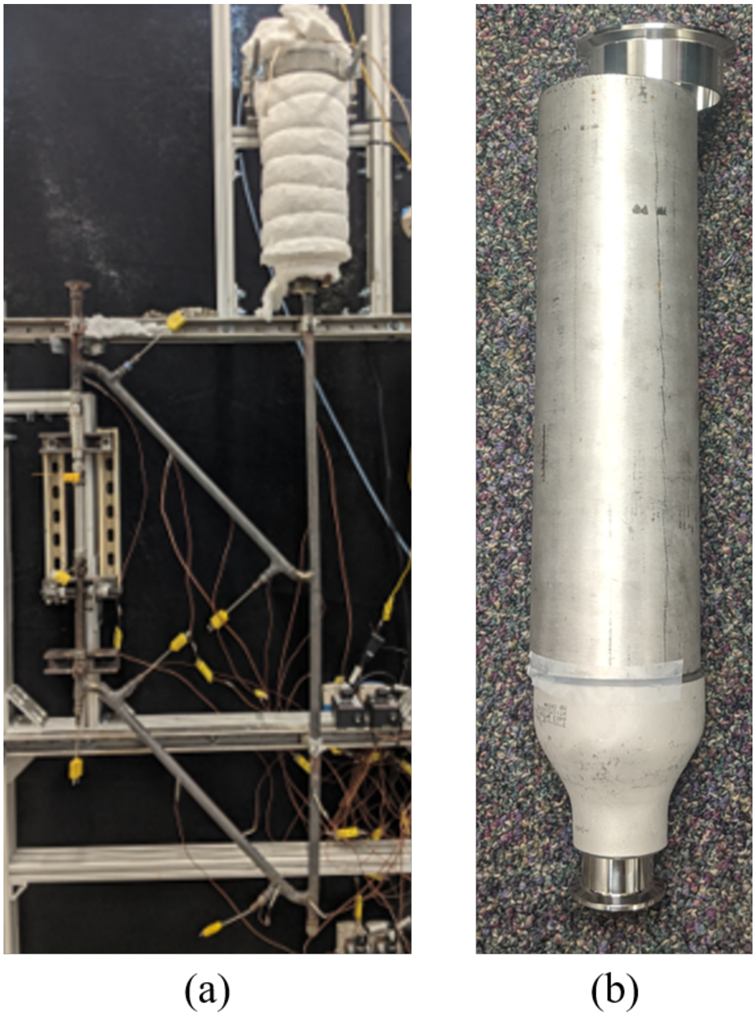
(a) (b)

Figure 3.2: (a) The flow loop prior to trace heating installation and insulation, (b) and the bare melting chamber.

At the top of the loop, two pipes extend and terminate at the same level. Each have 1 ½” sanitary Tri-Clamp adapters welded to the ends of them. In this study, all of the Tri-Clamp connections in the system utilize a custom cut vermiculite gasket to accommodate the high temperature in lieu of the standard elastomer gasket material. The longer of these two pipes, located opposite the visualization region serves as the connection point for the melting chamber and is used to fill the loop. The vertical extension above the test section allows for venting of the argon fill gas during the loop flooding. Since both sides extend above the highest point in the flow path, the loop allows for extra salt to be loaded during operation. This guarantees that the system is fluid solid, and since the free surfaces are at atmospheric pressure. Since the corner tees are oriented vertically, there are two more ports on the bottom of each joint. A compression fitting was welded to the open end of the tees. The port under the test section was used for another 1/8” k-type thermocouple probe (TP3), and the final remaining tee, being the lowest point in the loop was used as a drain valve.

The melting chamber is constructed of 3" schedule 40 316 stainless steel pipe welded to a conical reducer. On the open end of the 3" pipe, a 3" Tri-Clamp adapter is welded. The Tri-Clamp cap is then customized by welding four compression fittings, which were used to install two k-type thermocouples, an argon injection port/vent, and 1 extra port which was capped. On the bottom of the conical reducer, a 1 1/2" Tri-Clamp adapter was welded. The Tri-clamp melting chamber to loop connection allowed for a modular system and is shown in Figure 3.2. By having a clamp-on system, the melting chamber could be removed and maintained without disassembling the rest of the loop.

The loop is primarily heated by helically wrapping heating tapes around each leg, and attaching them by spot welding strips of stainless steel foil around the heating tapes to the pipe. The test section was wrapped similarly to the other pipe legs except near the glass where the tape was passed behind the test section. The bare loop, with the heating tapes installed is shown in Figure 3.3. Each section of the loop is independently managed with a power controller, and the heating equipment used is outlined in Table 3.1. The independent control of the sections allowed for the loop to be differentially heated, which allowed for natural circulation.

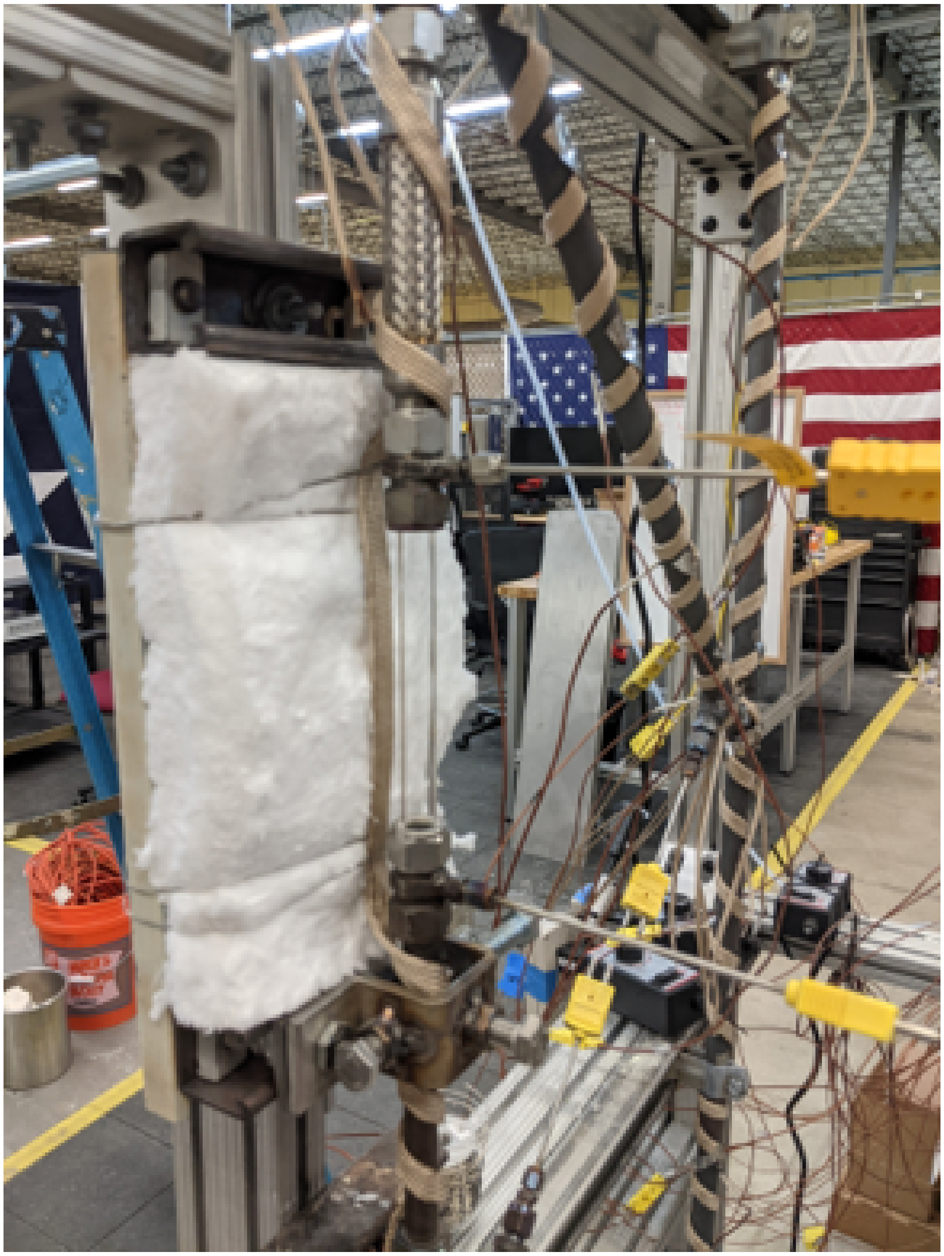

Figure 3.3: Trace heating installation prior to insulation.

The entire system was well insulated in order to achieve the desired temperatures, and the test section required additional considerations. Due to the large mounting structure, a the insulation did not tightly fit to the region, leaving a dead volume of air. Also, to collect the optical data required for PIV, the insulation around the test section was removed during recording so that viewing

Heating Element	Installed Location	Rated Power	Make	Power Control
4ft heating tape	Each leg of loop	312 W	HTS/AMPTEK	Manual
8ft heating tape	Melting Chamber	624 W	HTS/AMPTEK	Manual
Heat Gun (x2)	Below Test Section	1750 W (each)	Steinel	On-board

Table 3.1: Heating elements and power control methods used to provide power to loop.

windows could be exposed. Figure 3.4a shows the insulation condition when visual data was not being recorded, opening these viewing windows as seen in Figure 3.4b,


(a) (b)

Figure 3.4: (a) The visualization window closed with insulation and (b) shows the insulation configuration during imaging.

causes a significant loss of heat. To help offset the large heat loss, two 1750 W heat guns were added below the visualization region and can be seen extending into the insulation in Figure 3.4.

The digital control on the heat guns allowed users to more effectively control the heat output than the manual power controllers with the heating tapes. This increased control was beneficial during start-up so the heat-rate of the glass could be managed and hopefully preserve glass integrity. The insulation used on the entire loop was covered with at least two layers of 1" thick Aluminum Silica ceramic blanket. The insulation was manually fixed to the loop using stainless steel wire.

3.2 Test Section

Most commonly, plastics are used for PIV test facilities, but the temperature demands required glass to be used. 16mm OD, 12mm ID Fuzed-Quartz tubing was selected after a lengthy trial and error period. The length of the glass section was nominally 162mm. Initially thinner quartz was explored, but it simply could not survive the stresses induced installation and heating. An extensive effort was spent exploring the applicability of Sapphire as a possible material, but due to a chemical reaction with Fluoride salts that render sapphire opaque, Quartz was selected.

The primary challenge in this experimental campaign was connecting the glass tubing in such a way that the glass does not break during the heat-up, or when molten salt floods the loop proved to be a major challenge. Through trial and error, researchers learned that each successfully installed glass region would only survive a single test, and in-fact, unless the glass was installed correctly it would not even survive the heat-up. The single cycle lifespan required the glass test section to be changed following each test. In addition to being replaceable, the connection method needed to be liquid-tight at temperatures up to 700°C. Due to the time constraints and funding status of the project, exotic custom solutions were not feasible, so modifications were made to off-the-shelf components for the test section. The connectors were were 16mm Swagelok compression fittings, which were then bored-through to allow the glass free expansion the axial direction. Additionally, the a 1/8" compression fitting for thermocouples was welded at the axial midplane, to allow for temperature measurements at the inlet and outlet of the test section. Figure 3.5 shows test section assembly.

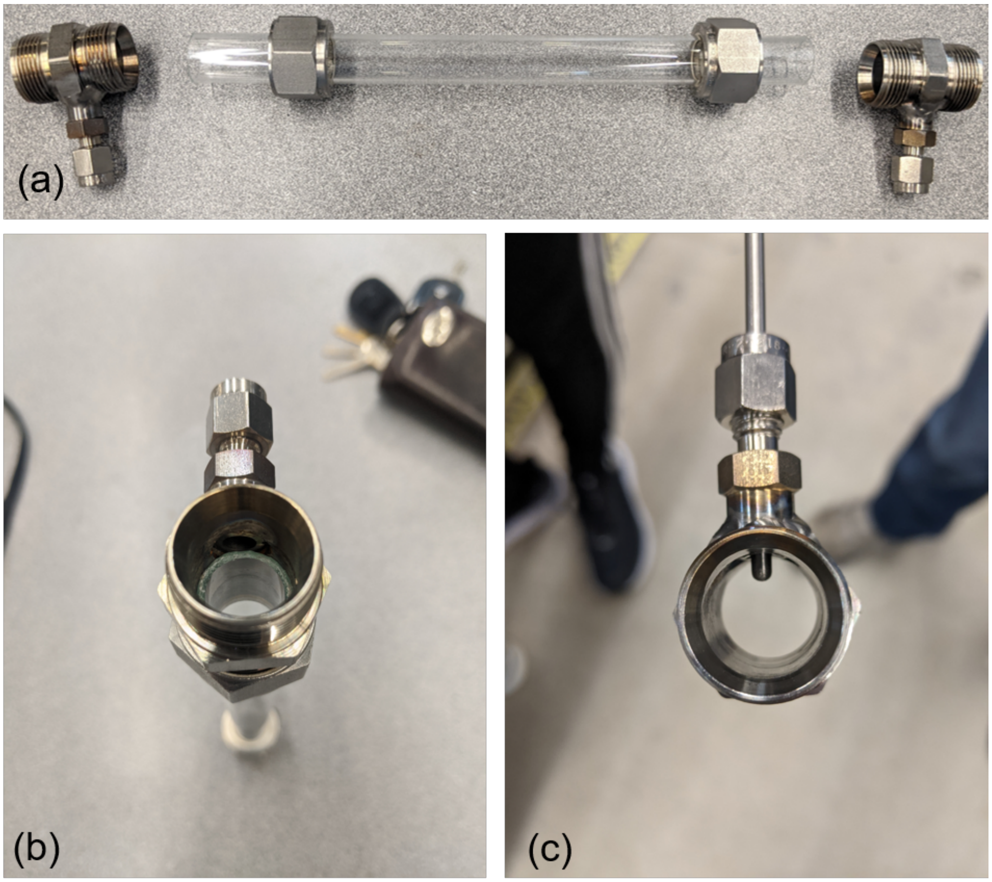

Figure 3.5: Visualization test section shown (a) disassembled, (b) the quartz penetration in the bored through fitting, and (c) the probe insertion for TP4 and TP5.

Figure 3.5(a) shows the exploded view of the primary test section. Figure 3.5(b) shows the Quartz test section inserted into the connector. Figure 3.5(c) illustrates the thermocouple probe insertion into the thermocouple fitting. The glass sized axially such that it did not physically touch the thermocouple, the main fitting was bored out so the glass could freely slide, and any axial restriction was avoided. Typically, when installing these compression type fittings onto stainless tubing, metal ferrules are utilized to provide the seal between the fitting and the tube. The stainless-steel ferrules commonly shattered the glass test sections before the fitting was even hand-tight, which is not even close to tight enough to set those ferrules into a liquid-tight configuration. To remedy this, graphite ferrules were utilized. Graphite ferrules provided multiple benefits including;

high temperature application, being slick so that while sliding up and down the tube the surface finish was not damaged in anyway, and being flexible. The flexibility was the key parameter for the ferrules, so that when the nut is tightened, the ferrule will slightly deform. This helps to prevent the glass from shattering, the system was found to be liquid-tight at a tightness which reliably did not break the glass. The glass tubing used in the experiment was manually cut, ground, and polished by researchers.

The test section mounting and support system system was also designed in an iterative fashion towards a successful solution. The liquid tight metal-glass connection discussed above needed to be supported such that the deflection caused by the temperature increase would not shatter the rigid glass. Another key consideration, was the alignment of the upper and lower connection, since glass is not flexible, if the inlet and outlet are out of alignment, when the fittings are tightened, the glass will break from the stress. Figure 3.6 shows the early progression of the mounting solution for the test section.

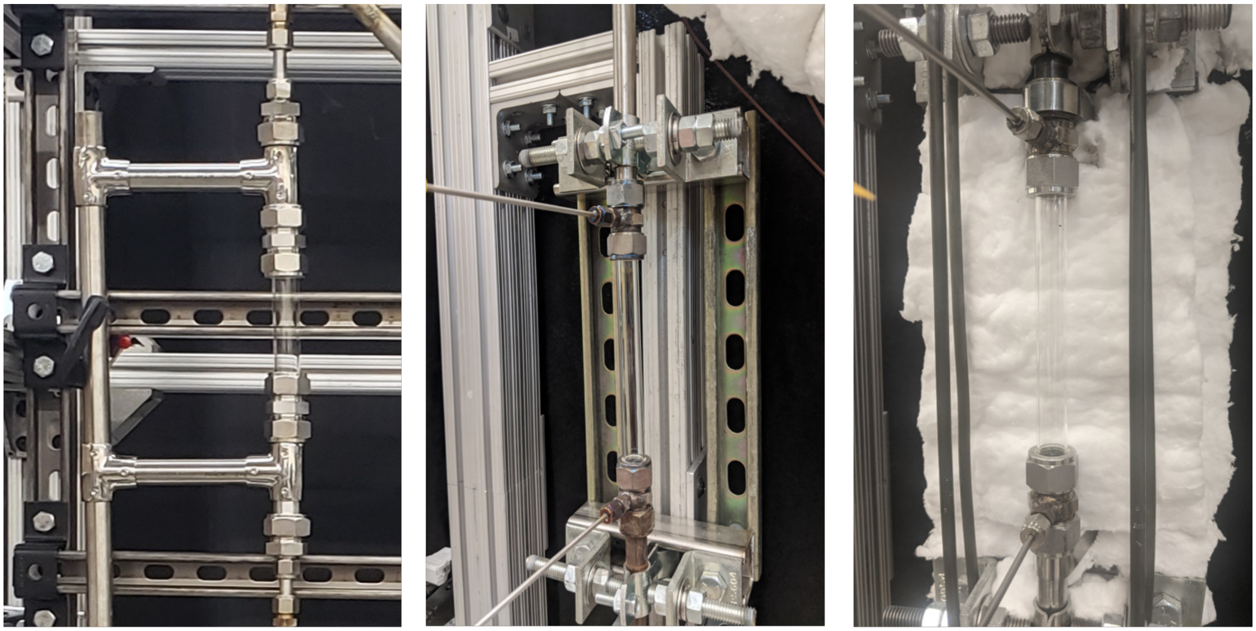

(a) (b) (c)

Figure 3.6: Failed test section mounting variations, (a) Initial clamping method, (b) new test section, addition of clamps, (c) adjustable metal bands added.

Figure 3.6(a) shows the first attempt, which relied on long pipe clamps. The pipe-clamp solution in Figure 3.6(a) did not provide any aid for the alignment and such was abandoned quickly. Figure 3.6(b) shows a mounting system which uses brackets and threaded rod to make adjustable mounting clamps. These aided with fine alignment, and rigidly holding the facility, but there was no was to move the fittings towards or away from the structure. This flaw was addressed in the improvement to the bracket found in Figure 3.6(c). Each step in this process made significant improvements, but the operational requirement that the test section was reliably replaceable was not met. The tolerance required in the alignment was very difficult to achieve with upper, and lower rigid mounts without re-designing the entire experiment.

To address the replacement issue in the test section, the upper pipe connection was replaced with a flexible corrugated stainless-steel pipe section. A piece of 16mm tubing was welded to the end so the compression fitting could connect to it, and the upper mount was removed. By proving a flexible member, any slight misalignment could be relieved, along with any thermally generated warp or twist in the pipe section. Figure 3.7 shows the final configuration used for the test section mounting procedure.

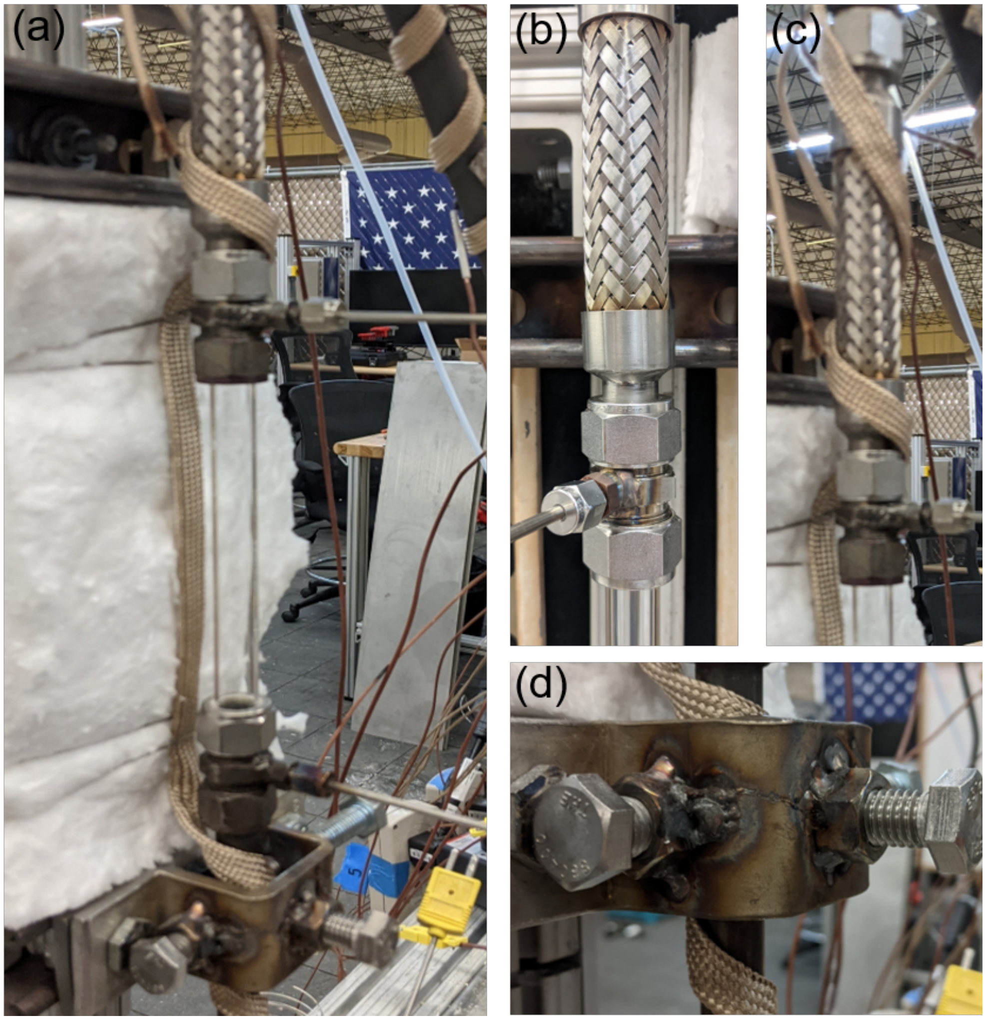

Figure 3.7: Final mounting configuration, (a) Test Section, with trace heating, lower clamp, and flexible upper connection. The flexible pipe connection used shown bare (b), and (c) with trace heating. The adjustable lower mounting clamp (d)

Figure 3.7(a) shows the test section installed with the heating tape in place, while Figure 3.7(b) is a close up of the stainless flexible tube, commonly referred to as flex hose. Figure 3.7(c) is a closeup of the flex hose with the heating tape wrap. The lower bracket from Figure 3.6(c) was replaced to allow for more insulation behind the test section, so the Figure 3.7(d) is the final version of the lower mount used.

3.3 Instrumentation

To measure the temperature the loop was equipped with 7 temperature probes that were installed into ports located along the flow and labeled TP1→TP7, and can be seen in Figure 3.8. Figure 3.8(a) shows the insulated loop with the approximate thermocouple positions superimposed with a color code that will be used throughout this document, and Figure 3.8(b) is a simplified model of the loop with the same TP coloring scheme, and will be included along side temperature plots as a reference. The inlet and outlet of the test section were TP4 and TP5, respectively, and the loop ΔT was defined as (TP6-TP1). Additionally, two thermocouples were inserted into the melting chamber, but these were not used in any analysis that follows, they simply were used to control the salt temperature prior to filling the loop with molten salt. In addition to the temperature probes, 15 wall thermocouples were welded to the outside of the loop, distributed evenly along the non-visualization leg piping. All thermocouples used in both probe and wall configuration were k-type, and had an accuracy of 0.4% of the total reading. These were connected to a mechanical Keysight 34972A data acquisition (DAQ) system. The temperature data was recorded at 1.1 Hz for the duration of the test. The distribution of the temperature probes along the flow path was important not only for thorough data collection, but also power control. The system needed to maintain a temperature differential to facilitate natural circulation. The ΔT causes a density gradient in the system, which drives the natural circulation.

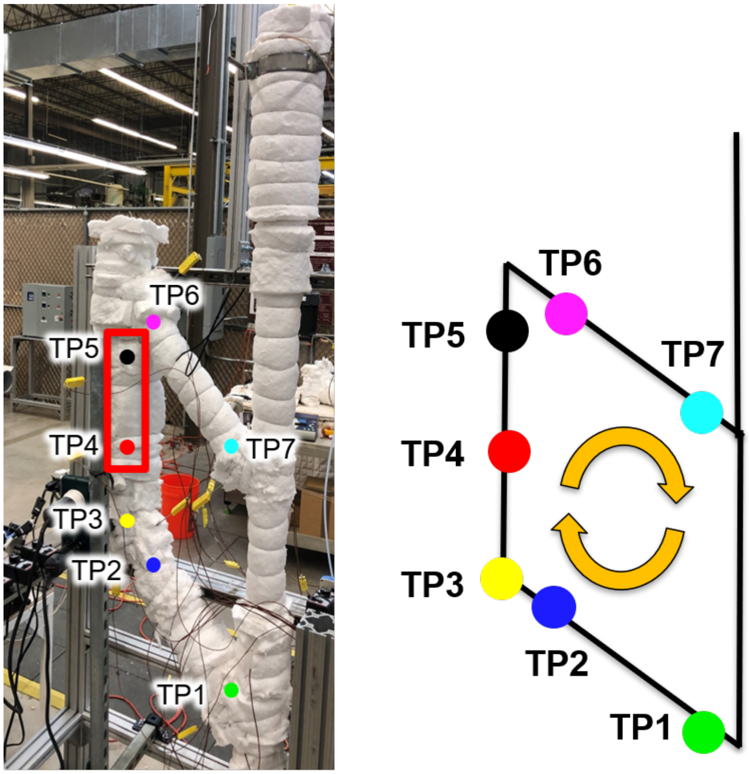

(a) (b)

Figure 3.8: The positions and labels of the thermocouple probes shown on (a) insulated loop. and (b) a simplified model of loop with arrows depicting direction of the flow

Like the temperature instrumentation, PIV equipment setup is rather straightforward. The geometry of interest was a vertical pipe, and the laser sheet was projected across the middle of the pipe, such that the illuminated region was perpendicular to the camera. Figure3.9 shows the orientation of the camera and laser for the data collection. This geometric configuration is not ideal for PIV. Image distortion is caused from multiple sources included the curved geometry, the change in refractive index between and and molten salt, the large ΔT in the air from the camera and laser to test section, and the inability to do an in-situ calibration. The laser illumination was a continuous 20W, 532 nm laser. Lenses were applied to generate the vertical plane that was passed through the test section. The camera hardware is included in Section 4.3.1, as part of the discussion on the PIV methodology followed.

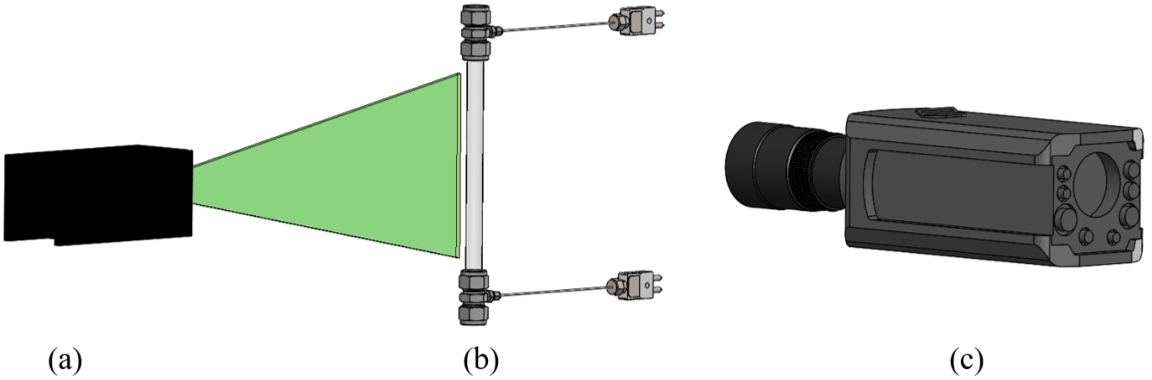
(a) (b) (c)

Figure 3.9: Model of PIV component configuration (a) planar laser, (b) test section, (c) the camera

3.4 Salt Operations

The salt used in this work is a eutectic fluoride salt mixture of LiF-NaF-KF, with mass fractions (0.465-0.115-0.42), and is typically referred to as FLiNaK. To prepare the mixture, the individual fluoride salt components were initially weighed then and mixed in a using an sealed electric mixer. At this point in the preparation the borosilicate seeding particles were added to the salt, . Once the powered FLiNaK was well mixed, it was loaded into porcelain crucibles, and placed into a muffle-top furnace and heated to 600°C for 4-6 hours. The furnace was initially purged with argon, and then continually flushed with a slight flow of Argon gas to reduce oxidation of the salt mixture, and maintain higher purity. The salt filled crucibles were then allowed to cool, and the salt ingots removed to be placed in the melting chamber. Once the salt was loaded into the melting chamber, the facility could begin to heat-up. The entire facility would be pre-heated to the desired operation temperature, and the salt would slowly heat-up and melt. The bottom connection of the melting chamber acted like a cooling fin, and produced a minor salt plug which impaired the steady filling of the loop. To overcome the salt plug, the fill-salt would be heated much higher than its melting point to over 600·C. When the salt plug yielded, the facility was rapidly flooded with the hot salt. To ensure the system was fluid solid, extra salt than what was calculated to clear the top corner added to the melting chamber. A total of 1.4kg of FLiNaK ingots were loaded into the melting chamber. Figure 3.10 shows the various salt preparation steps;

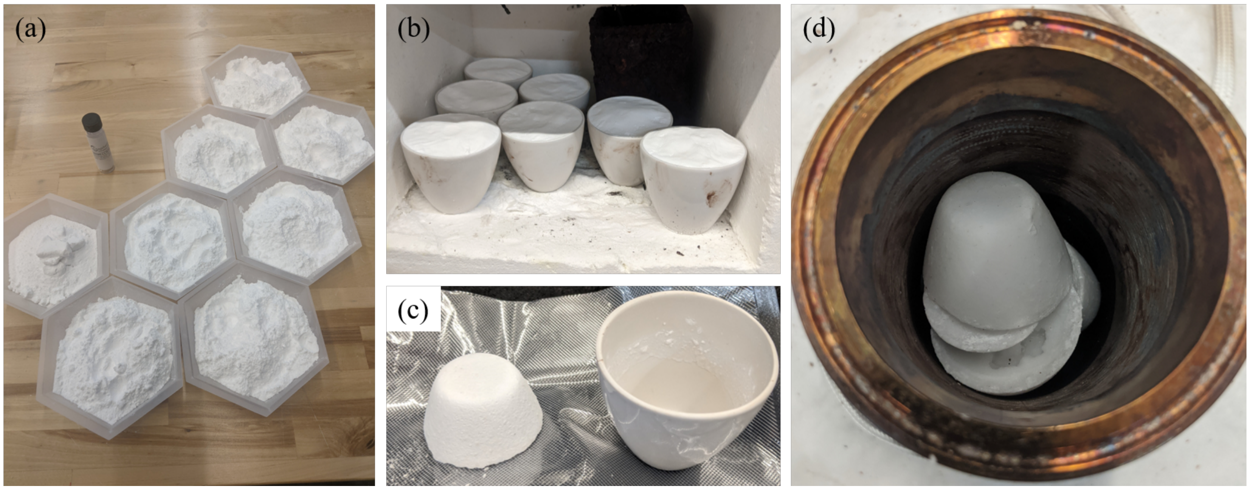

Figure 3.10: The progression of the FLiNaK preparation. (a) Powdered FLiNaK components and the tube of borosilicate particles, (b) the FLiNaK powder loaded into crucibles and placed in oven, (c) the resulting FLiNaK ingot and porcelain crucible, (d) FLiNaK ingots in the melting chamber.

In addition to the salt, one ingot contained the PIV seeding particles with properties that can be found in Table 4.1 were mixed in. Various seeding methods were tested, but likely due to some seeding hangup in the melting chamber, it was found that putting all the particles into one ingot yielded better particle density for PIV during the visualization. Some properties of FLiNaK have a strong dependence on temperature, so to calculate these as a function of temperature, the empirical correlations in 3.1 are used. As with all fluids, many properties have dependencies on temperature are listed in Equation 3.1[35]. Common properties have been calculated for the experiment temperature span and are reported in Table 3.2.

$$\begin{aligned} \rho &= 2573.3 - 0.624(T) \\ \mu &= 2.49 \cdot 10^{-5} \cdot 10^{\left(\frac{1944}{T}\right)} \\ \beta &= \frac{-0.624}{2573.3 \cdot 0.624(T)} = \frac{1}{\rho} \cdot \frac{\partial \rho}{\partial t} \end{aligned} \tag{3.1}$$

Property	Symbol	500°C	600°C	700°C	Units
Density	ρ	2097	2034	1972	kg m^{-3}
Viscosity	μ	0.0081	0.0042	0.0025	Pa s
Prandtl Number	Pr	18.00	9.3	5.5	-
Spec. Heat Capacity	c_p	1880	1880	1800	J (kg °C)$^{-1}$
Th. Conductivity	λ	0.85	0.85	0.85	W m^{-1} °C^{-1}
Thermal Expansion Coef.	β	-0.0003	-0.0003	-0.0003	(1×10^{-3})°C $^{-1}$

Table 3.2: Physical Properties of FLiNaK over experiment temperature span.

4. EXPERIMENTAL METHODS

This chapter includes the experimental workflow, flow visualization, and the data analysis techniques employed to characterize the steady state and transient flow behavior in the natural circulation molten salt loop. To generate the velocity fields PIV was primarily used. The hallmark non-intrusive nature of PIV was leveraged to effectively produce resolved flow-fields in an otherwise inaccessible environment due to the extreme temperatures and corrosive properties of the fluid. The experiment work flow is rather straightforward. Salt was mixed and formed into ingots, loaded in the loop, and melted. A temperature gradient was applied to the loop with differential heating, and natural circulation was established. High-resolution videos of the flow in the visualization region were recorded concurrently with wall and probe temperature measurements. The following sections outline these processes.

4.1 Analysis Techniques & Governing Equations

This section includes the governing equations and brief introduction of the various data analysis techniques of both the temperature and flow velocity data generated in this study. The velocity and vorticity fields were decomposed using Reynolds Decomposition, and Proper Orthogonal Decomposition (POD). By manipulating velocity fields, various insights can be gained into the flow phenomena that are not readily seen in the velocity fields including the coherent turbulent structures [36][37]. These decomposition methods mathematically simplify the flow field and allow for less computational demand when modeling fluid systems. Fast Fourier transform was applied to the POD temporal coefficients to gain insight into the frequency of the dominant flow structures. Finally, an analysis of the distribution of the vortex size and location was completed.

The mathematical framework used for this study begins with the conservation equations. The conservation of mass assuming an incompressible flow where $\frac{\partial \rho}{\partial t} = 0$, reduces to

$$\frac{\partial u_i}{\partial x_i} = 0 \tag{4.1}$$

where x_i is representing the Cartesian coordinates (x,y,z), u_i is simply the velocity vectors (u, v, w), and ρ is fluid density. Equation 4.1 is commonly known as the continuity equation. If we assume no external forces, the Navier-Stokes (NS) equation describing the conservation of momentum is given as

$$\frac{\partial u_i}{\partial t} + u_j \frac{\partial u_i}{\partial x_j} = -\frac{\partial P}{\partial x_i} + \nu \frac{\partial^2 u_i}{\partial x_j^2}, \tag{4.2}$$

where kinematic viscosity ν is derived using ρ and fluid viscosity μ as (μ/ρ). Similar to kinematic viscosity, P is the kinematic pressure which is absolute pressure normalized by density[38].

To aid in the comparison of results and visualization of data, a variable called vorticity is derived from the 2D vector field[39]. The vorticity ω_i is defined as the curl of the velocity field in Equation 4.3,

$$\omega_i = \nabla \times u_i \tag{4.3}$$

and is a pseudovector which shows the local spinning motion of the flow. For the 2D data collected in this study Equation 4.3 expands to,

$$\omega_z = \frac{\partial v}{\partial x} - \frac{\partial u}{\partial y} \tag{4.4}$$

To effectively compare the data generated with other studies, both CFD and experimental, dimensionless numbers are calculated. The Reynolds number (Re) is the primary parameter used to identify which flow regime the flow is currently under: laminar, turbulent, or transition between the two. The Reynolds number is defined by Equation 4.5,

$$Re = \frac{\rho_f \overline{v} D_h}{\mu_f}, \tag{4.5}$$

where ρ_f is the fluid density, $\overline{v}$ is the mean axial velocity taken at the midplane, D_h is the hydraulic diameter which in this case is simply the internal diameter of the pipe, and μ_f is the fluid dynamic viscosity. Another key dimensionless parameter in the study of fluid systems is the Prandtl number (Pr), Prandtl number is defined by Equation 4.6,

$$Pr = \frac{c_p \mu}{\lambda} \tag{4.6}$$

where c_p is the specific heat capacity, μ is the dynamic viscosity, and k is thermal conductivity. Pr is important when considering a fluid for possible heat transfer applications because physically it can be interpreted as the ratio of momentum transport to heat transport.

4.1.1 Reynolds Decomposition

Once the velocity fields were generated with the PIV algorithm, Reynolds decomposition will be applied to data so that it can be used as a comparison tool for computational methods. As flow complexity increases, solving Equation 4.2 becomes extremely computationally difficult because of the non-linearity. To combat this, the flow field is decomposed into its mean velocity field, and the fluctuating component[40]. The time average of a set of T velocity fields is calculated with Equation 4.7.

$$\overline{u_i}(x_i) = \frac{1}{T}\int_0^T u_i(x_i,t)dt. \tag{4.7}$$

With the time-average calculated, the set of instantaneous velocity fields the Reynolds decomposition can be performed

$$u_i(x_i,t) = \overline{u_i}(x_i) + u_i'(t), \tag{4.8}$$

yielding $u_i'(t)$, which is the fluctuating component of velocity. If the decomposed quantities are applied to Equations 4.1 & 4.2, the result is known as Reynolds-Averaged Navier Stokes (RANS), and is shown below.

$$\overline{\frac{\partial u_i}{\partial x_i}} = 0 \tag{4.9}$$

$$\rho\overline{u_j}\frac{\partial \overline{u_i}}{\partial u_j} + \rho\frac{\partial \overline{u_i'u_j'}}{\partial x_j} = -\frac{\partial \overline{p}}{\partial x_i} + \mu\frac{\partial^2 \overline{u_i}}{\partial x_j \partial x_j} \tag{4.10}$$

It is important to note in Equation 4.10, that the time derivative in the original NS equation has be removed by the Reynolds decomposition as it is averaged to zero. A product of this decomposition, is then introduced $\overline{u_i'u_j'}$, which is referred to as the turbulence strength. For the purposes of this study, the variables used were $\overline{u'}$ and $\overline{v'}$ which are the horizontal and vertical components, respectively and translates to the Reynolds shear stress, also called turbulence strength is $\overline{u'v'}$. Due to the statistical nature of the fluctuating component, a simple average cannot be taken over the data-set, so to provide a meaningful quantity for analysis the root-mean square (RMS) of the fluctuating component to be calculated, and is shown below in Equation 4.11

$$u_{i,RMS} = \sqrt{\frac{1}{N}\sum_{n=1}^{N}(u_{i,n} - \overline{u_i})^2}. \tag{4.11}$$

4.1.2 Proper Orthogonal Decomposition

Proper Orthogonal Decomposition (POD) is a mathematical tool that is used to identify flow structures by their relative energy content[41][42]. POD takes a set of spatially and temporally resolved data, and decomposed this data set into spatial basis functions and temporal coefficients. The POD spatial modes represent the large-scale orthogonal flow structures, and are ordered by the relative amount of kinetic energy they each possess. POD has the ability to approximate highly resolved experimental data using lower-order methods. Since a large fraction of the kinetic energy (KE) and flow structure information is contained in the first few modes, we are able to down-scale the complexity of the flow considerably, allowing for easier comparison between simulated results [43][10][44][45].

The application of POD used in this study is known as snapshot POD[46][47]. If an instantaneous field vector (in this case vorticity),$\boldsymbol{\omega}(\mathbf{x}, t)$ is given over a finite time interval $(0 < t < T)$, it can be decomposed into spatial modes and temporal coefficients using Equation 4.12. Where N is the number of vorticity fields, ζ_k are the temporal coefficients, and $\Psi(x)$ are the spatial basis functions, which are simply the eigenvectors of the two-point correlation matrix. The two-point correlation is computed using Equation 4.13, and is denoted by C_{ij}.

$$\boldsymbol{\omega}(\mathbf{x}, t) = \sum_{k=1}^{N} \zeta_k(t)\boldsymbol{\psi}(\mathbf{x}) \tag{4.12}$$

$$C_{ij} = \frac{1}{N} \int \boldsymbol{\omega}(\mathbf{x}, t_i) \cdot \boldsymbol{\omega}(\mathbf{x}, t_j) d\mathbf{x} \tag{4.13}$$

It is useful to define another variable α_{ki} using Equation 4.14, where ν_i^k is the ith element of the eigenvector ν^k. The λ_k eigenvalue of C_{ij} correspond to the eigenvector ν^k.

$$\alpha_{ki} = \frac{\nu_i^k}{\sqrt{N \sum_{m=1}^{N} \sum_{r=1}^{N} \nu_m^k \nu_r^k C_{mr}}} \tag{4.14}$$

$$\boldsymbol{\psi}(\mathbf{x}) = \sum_{k=1}^{N} \alpha_{ki} \boldsymbol{\omega}(\mathbf{x}, t_i) \tag{4.15}$$

Taking α_{ki}, we can the compute the spatial basis functions and the temporal coefficients using Equations 4.15 & 4.16.

$$\zeta_k = \int \boldsymbol{\omega}(\mathbf{x}, t) \cdot \boldsymbol{\psi}(\mathbf{x}) d\mathbf{x} = N \sum_{k=1}^{N} \alpha_{ki} C_{ij} \tag{4.16}$$

.

4.1.3 Frequency Analysis

It is useful to look at the data in the spectral domain when looking at turbulent behavior so the dominant flow frequencies can be identified. Viewing the flow in the specral domain, the kinetic energy dissipation can be observed as the turbulent structures break down into smaller structures[48]. By applying Welch's method [49], we transform the data to the spectral domain and allow for the identification and comparison between the dominant flow frequencies. Welch's method generates the Power Spectral Density (PSD), which describes the magnitude of the signal as a function of frequency. This is accomplished using a Fast Fourier Transform over equal-sized segments of the data known as windows. This partitioning is refereed to as Discrete Fourier Transform (DFT). In Welch's method, the data is broken into a defined number of windows, calculates the periodogram of each window, and averages the whole set together. To minimize the loss of information, these windows are typically overlapped. The window size was selected to be 2048, and the overlap was

512 or 25%. The PSD for the POD temporal coefficients was calculated for each data-set, and is included in the Chapter 5.

4.1.4 Vortex Characterization

In order to quantify the vortex behavior observed in the test section, an identification & tracking procedure was applied to PIV derived vorticity data. Due to the temperature gradient on the test section, an oscillating boundary layer was observed [50][51]. Using vorticity magnitude, vortex structures can be identified [52]. Vortex area (A_Ω) was calculated by multiplying the pixel width by the pixel height of the cutoff. The vortices were defined by a width and length using Equation 4.17 cutoff,

$$A_\Omega = r_{vortex} \cdot l_{vortex} \tag{4.17}$$

where r_{vortex} is the x-dimension of the vortex and actually a radius in physical dimensions because the vorticies are 3-dimensional structures, and the length of the vortex is simply l_{vortex}. The hydraulic diameter of the test section was used for the length of the vortex, $l_{vortex} = D_H$, and one-third pipe radius was used for vortex radius. $r_{vortex} = \frac{1}{3} \cdot r_{pipe}$. Since the PIV generated vectors are calculated on a discrete grid, approximate values were used for the vortex cutoffs. The PIV grid resolution was 0.8mm in the horizontal direction (∂X), and 1.7mm in the vertical direction direction (∂Y). This yields a x-direction cutoff of $\approx$ 2.5 pixels, and y-direction cutoff of $\approx$ 8 pixels, When multiplied this gives a minimum vortex area of 20 pixels, or $\approx$ 34 mm^2

4.2 Particle Image Velocimetry

To generate the velocity data, Particle Image Velocimetry (PIV) was used. By employing the data collection and processing outlined in Sections 4.3.1-4.3.2, a set of images was prepared to be analyzed by the PRANA PIV code within MATLAB [53].PIV scans an image and identifies particles that have been excited by the laser, then compares subsequent images taken after a ΔT, the program identifies where the particle moved to. Using the change in time and displacement a set of instantaneous velocity vectors for the flow field is generated. The particle displacement is estimated using a spatial cross-correlation technique that discretizes the image into smaller "interrogation windows" [54]. To achieve this, the image is interpreted as an intensity field $I_n(x)$, and the intensity value for each pixel can take 2^n, where n is the bit-depth of the image.

To effectively assume that the particle motion closely follows the fluid motion, the density of the fluid and particle are matched as closely as possible to reduce buoyancy forces, and the particle diameter minimized. Seeing particle size though, is dependent on other considerations as well, as the particle size is reduced the reflected light off the surface reduces as well. This effect can counteracted with highly reflective particle coatings, and increasingly powerful laser illumination. Other important considerations include the imaging hardware and optics used in the data collection. Since the PIV algorithm acts on a field of pixels, the particle diameter in pixels is a function of many factors including distance, magnification, particle size, and resolution. The optimal particle size for PIV is 2.2 pixels[55][56].

The deviation of particle motion from the fluid motion can be assessed calculating the Stokes number [57], which is the ratio of the particle response time τ_p to the fluid response time τ_l,

$$\tau_p = \frac{d_p^2 \rho_p}{18\mu}, \tag{4.18}$$

where d_p and ρ_p are the particle diameter and density, respectively, and μ is the fluid viscosity. The fluid response time can also be described as the largest scale eddy turnover time,

$$\tau_f = \frac{L}{\overline{u}}, \tag{4.19}$$

where L is the characteristic length, which in this case is the hydraulic diameter D_H, and $\overline{u}$ is the mean bulk velocity. Equations 4.18 & 4.19 can be combined, which yields the Stokes number (Stk),

$$Stk = \frac{\tau_p}{\tau_f} \tag{4.20}$$

This study is slightly recursive in how this was calculated since there was no flow meter installed, so the PIV processing was required to get the bulk velocity, which was then passed back through to confirm the validity of the particle selection. If $Stk << 1$, we can assume the particle movement accurately represents the fluid behavior [58]. The parameters used to estimate the stokes number are included in Table 4.1, the fluid velocity used in this table is the maximum velocity seen in Table 5.1, and the target temperature of 600°C was used for the viscosity calculation.

Parameter	Value	Unit
Particle Density	2.2	$\frac{g}{cm^3}$
Particle Diameter	38-45	μm
Hydraulic Diameter	12	mm
Viscosity (°C)	4.2	mPa·s
Bulk Velocity	0.0183	$\frac{m}{s}$

Table 4.1: Quantities used to calculate the Stokes number for the experiment.

4.2.1 Convergence

From the PIV analysis, $N_{max} \approx$ 22,000 instantaneous velocity snapshots were taken from the videos. Using these velocity fields, the convergence of the statistical results was computed for each video. The convergence of time-averaged the horizontal and vertical mean velocities, RMS flucuating velocities, and the Reynolds shear stress were calculated with different numbers of the velocity fields. Since the videos contained slightly variable vector field populations, increments of 5000 snapshots were selected, so N_1 = 5000, N_2 = 10,000, N_3 = 15,000, N_4 = 20,000. Using Equation 4.21,

$$\varepsilon_{\tilde{N_j}} = \frac{1}{M}\sum_{i=1}^{M} |(S_i)_{N_j} - (S_i)_{N_{max}}| \tag{4.21}$$

where $\varepsilon_{\tilde{N_{1\to4}}}$ is the spatial average over the entire measurement area of the absolute differences between the statistical results. S_i is the statistical result being studied, and M is the number of spatial grid points in the measurement area[45][44][59][60]. For each video, the convergence results were normalized by the mean vertical velocity component for the whole measurement area.

The convergence for each dataset is in the combined results Sections 5.1.4,5.2.4,5.3.4.

4.2.2 Measurement Uncertainty

There exist many methods to analyze the uncertainty with the PIV methodology and have been detailed in many studies [61][62][63][61]. For this study, a simpler approach was utilized due to the technical complexity of the experiment[64]. The primary sources of uncertainty from PIV come from image distortion which is caused by many factors including test-section geometry and optical equipment. The uncertainty of the mean velocity components $e_{\overline{u_i}}$ was calculated with

$$e_{\overline{u_i}} = \frac{\sigma_{u_i}}{\sqrt{N}} \tag{4.22}$$

where σ_{u_i} is the standard deviation of the individual components, and N is the number of samples. The RMS of the fluctuating components is functionally the standard deviation, to calculate the uncertainty of the standard deviation Equation 4.23 is used.

$$e_{u_i,RMS} = \frac{\sigma_{u_i}}{\sqrt{2(N-1)}} \tag{4.23}$$

The only second-order statistical quantity calculated was the Reynolds shear stress, or the Turbulence Strength. The Reynolds shear stress is defined as the covariance of the velocity components, and to calculate the uncertainty of this quantity Equation 4.24 is utilized.

$$e_{\overline{u_i'u_j'}} = \sigma_{u_i}\sigma_{u_j} \cdot \sqrt{\frac{1+\varrho_{ij}}{N-1}} \tag{4.24}$$

where ϱ_{ij} is the cross-correlation coefficient, but since planar 2D PIV was employed, it can be assumed ϱ_{ij} = 0. So Equation 4.24, reduces to

$$e_{\overline{u_i'u_j'}} = \sigma_{u_i}\sigma_{u_j} \cdot \sqrt{\frac{1}{N-1}}. \tag{4.25}$$

4.3 Workflow

The experiment workflow will be covered in this section. To perform PIV on the experimental data, the high speed video was acquired is detailed in Section 4.3.1. Once the raw data was acquired, the videos were broken into *N* frames and were passed through image processing software to prepare the images for the PIV algorithm, this is explained thoroughly in Section 4.3.2. Once the images were ready to go, they were analyzed using PRANA PIV algorithm. Section 4.3.3 details the steps from taking the pre-processed images to instantaneous velocity profiles.

4.3.1 Data Collection

To collect data to be used in laser-based PIV, a few components are universally required; a a laser, reflective seeding particles in the fluid, and a camera. If a pulsed laser source is employed, a trigger/synchronizer are also needed, but in this experimental work a continuous laser was used. Depending on the type of PIV analysis to be conducted, the laser is manipulated with lenses and other optical equipment to provide the proper illumination. In this study, the point generated laser was passed through a cylindrical lens to create a planar sheet, which was then oriented vertically on the test section.

All of the optical measurements in this study employed the same Phantom Miro V711 camera. This camera utilizes a CMOS sensor which provides full resolution of 1280×800, and is capable of recording this maximum resolution at 7530 frames per second with a bit-depth of 12. Since this study was on single-phase natural circulation, the velocity of the flow was slow, this allowed lower frame rates to be used, the 400 Hz was selected as the image-sampling rate. This particular camera is outfitted with an on-board random access memory (RAM) unit with 32 Gigabytes of memory. The memory on the camera was partitioned into 4 equal bins, so that 4 distinct videos could be recorded without waiting for transferring the RAM to the computer controlling the system which takes 20-30 minutes. Each group of 4 videos, are called a dataset, and a total of 5 data sets were recorded. The specific camera settings used in the data collection are listed in Chapter 5. The partitioning method was not particularly necessary because it was decided to take the videos in rapid succession, which could have been also accomplished by recording a single long video.

The seeding particles used were solid borosilicate glass spheres, produced by Cosphoric. Ideally, a coated particle would have been used, but due to the elevated temperature and density of the FLiNaK, these glass spheres worked well. The particle size was selected such that the illuminated particles were the correct size.

4.3.2 Pre-Processing

The camera captured the optical data in the form of a proprietary video format called a .CINE file. To continue with PIV, the video file had to be broken into individual frames, and then pre-processing of the images was performed to allow the PIV software to more effectively handle the images. To aid PRANA the contrast was altered on the images, and the built in smoothing function was performed on the image set. Each image set was averaged together to get a mean intensity field, which is typically referred to as the background, which is subtracted. This helps to remove artifacts such as reflections or other local bright spots that are not from particle reflection.

4.3.3 Processing

Once the images were pre-processed using the procedure detailed in Section 4.3.2, a open source PIV processing tool PRANA was the primary tool utilized to generate the instantaneous velocity fields. This tool is based on advanced milti-pass, multi-grid processing that employs Discrete Window Offset (DWO), and a 3-point Gaussian estimator. The processing algorithm catalogues the size, intensity, and location of the particles within the interrogation window, and then scans the second image in the image pair for the particle pattern identified in the interrogation window. The user determines the search window size, interrogation window size, interrogation windows to overlap fraction. The process was repeated for 3 total passes. Table 4.2 contains the processing settings in the PRANA code for the analysis in this study.

When processing the images, the time delay between steps is customizable by the user, so long that the frame rate is sufficient that the user can down-sample the video. The particle displacement between images should be a minimum of 1 pixel[65], but around 4 pixels gives higher fidelity

Parameter	Pass 1	Pass 2	Pass 3
Multigrid Method	Bi-cubic	Bi-cubic	Bi-cubic
Search Window size (pixel)	64×128	32×64	32×64
Interrogation window size (pixel)	32×64	16×32	8×16
Interrogation window overlap	50%	75%	75%
Grid buffer	12×8	12×8	12×8
Correlation Type	RPC	RPC	RPC
Peak location Estimator	3Pt. Gaussian	3Pt. Gaussian	3Pt. Gaussian
Vector Validation	UOD Median	UOD Median	UOD Median

Table 4.2: PRANA PIV processing settings

data. To accomplish this, the the PRANA algorithm skipped 5 images, such that image 1 would be compared to image 6, image 2 with image 7, all the way for the entire image sequence. This effectively reduced the sampling rate from 400 Hz, to 80 Hz. The PRANA algorithm outputs the instantaneous velocity vectors for the horizontal $u(x,t)$ and vertical $v(x,t)$ components of the flow, and the spatial grid coordinates that the vectors are located at. Each of the outputs is formatted into an matrix, which can then be processed using the methodologies discussed in Sections 4.1.1 - 4.1.4

5. MEASUREMENTS

This section includes the results and analysis from the experimental work. The successful test which produced the results contained in this dissertation consisted of a series of 5 data sets. Each data set contains 3-4 individual recordings that were processed using the methods outlined in Section 4.2. Due to the experimental challenges with collection of data, not all of these videos are usable. Figure 5.1 contains a breakdown of the various cases explored in this document.

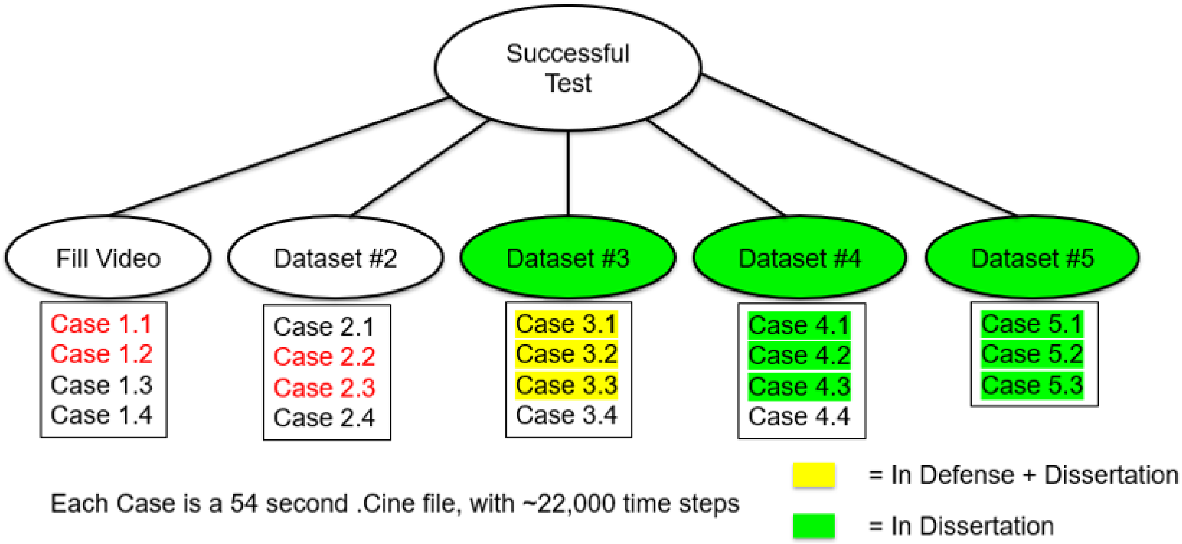

Figure 5.1: Summary of the data sets and the various cases included in this dissertation.

At the beginning of each data set, the system was insulated and could approach steady-state. The first case in each data set is immediately following the removal of the insulation, and the following cases are recorded in sequence with the minimal amount of time possible with manual actuation of the camera, with the exception of the time immediately following case 5.2 in which nearly 4 minutes elapsed before case 5.3 began recording. All of the results in this Chapter were produced in the same geometric configuration with a vertical planar laser sheet, and the primary difference is the ΔT in the overall loop, and the test section. The temperature data for the entire successful test outlined in Figure 5.1 is illustrated in Figure 5.2(a) and (b).

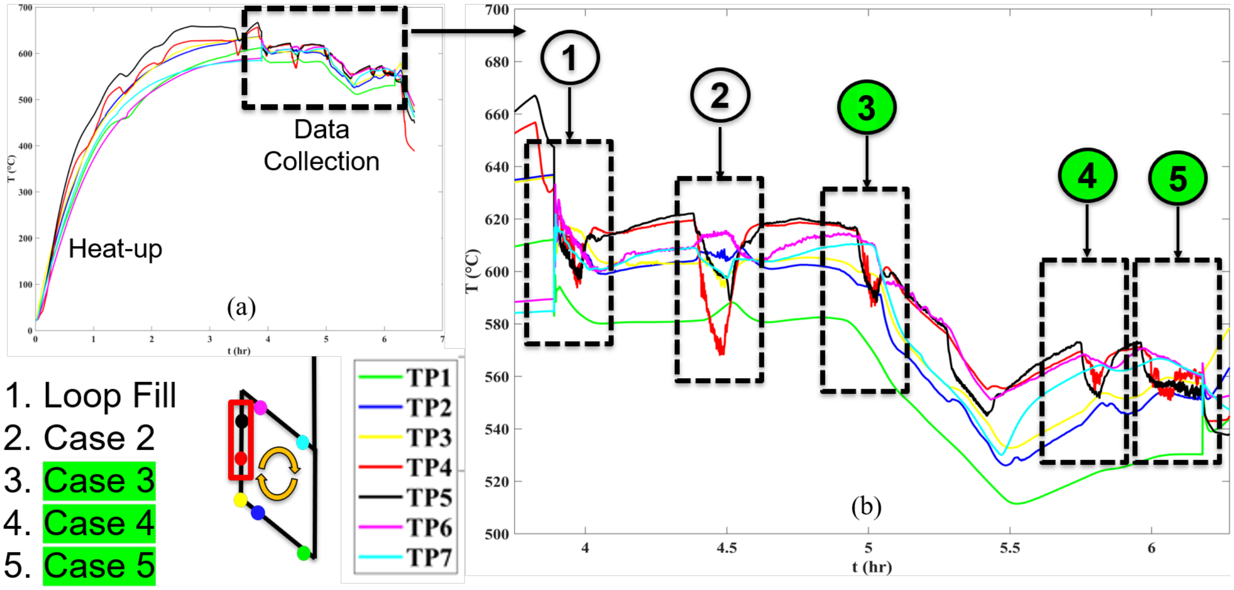

Figure 5.2: Full facility temperature probe response for entire test test on 02-03-2021

Figure 5.2(a) identifies the heat-up phase of the experiment, and the data collection phase. The data collection phase is then zoomed in on for Figure5.2(b). The dotted-line boxes are not drawn to scale, they are just a reference for the time period when the data was collected, a more detailed view of the temperature response is included in each data sets analysis Section. Table 5.1 contains the flow conditions for the usable PIV videos recorded. The Reynolds and Prandtl number are calculated with the temperature dependent properties of FLiNaK. Table 5.1 shows the ΔT for both the test section, and the overall loop. In data sets 3 and 4 where the mean flow stagnates over time, the ΔT_{TS} initially expands during the beginning of the thermal transient. Over time, ΔT_{loop} increases, and eventually an inversion of the test section temperature gradient is observed. This inversion of the temperature gradient ceases the net current, even though a large temperature gradient exists across the loop, the fluid begins to stratify in the loop. Data set 3 starts from the most stable initial temperature leading up to the image collection. Data set 3 undergoes a significant velocity decrease following case 3.3. starts at the highest temperature, it shows the largest magnitude temperature decline. The Reynolds number was calculated with Equation 4.5, and for fluid velocity, the mean velocity across the vertical mid plane was used.

This following sections of the dissertation explore the results and analysis that were derived using the PIV methodology. Since the thermal transient induced by the removal of the insulation window is impetus for the evolution of the flow, the temperature evolution of the salt is included at the beginning of each Section. Once the temperature condition has been established, the PSD's of the POD vorticity field temporal coefficients is analyzed, along with the vortex area distribution and the vortex statistics. Each combined data-set also holds a table which contains the statistical uncertainty from the PIV method for the first and second-order statistics. After the combined analysis is complete, each subsection looks at the fluid behavior of each of the cases within the data set.

case	Re	Pr	$\overline{UV}_{midplane}$ [$\frac{m}{s}$]	$\overline{T}_{TS}$ [°C]	$\overline{\Delta T}_{TS}$ [°C]	$\overline{\Delta T}_{loop}$ [°C]
3.1	91.0	8.6	0.0145	613.5	-2.8	35.8
3.2	92.7	9.0	0.0155	605.1	-6.9	36.7
3.3	84.5	9.4	0.0147	597.9	-4.2	38.2
3.4	47.2	9.7	0.0085	592.4	1.3	40.0
4.1	79.7	10.8	0.0159	574.3	-3.1	43.4
4.2	88.3	11.3	0.0183	568.0	-10.3	42.2
4.3	86.3	11.5	0.0182	564.9	-11.1	40.0
4.4	84.1	11.9	0.0183	560.0	-9.8	35.5
5.1	60.2	11.1	0.0123	570.3	-1.2	43.0
5.2	51.3	11.5	0.0108	565.1	-7.5	42.1
5.3	27.6	12.2	0.0062	555.4	3.8	36.4

Table 5.1: Fluid data for datasets 3,4,5

5.1 Data Set 3

5.1.1 Data Set 3.1 Steady State, Onset of flow instability

Data set 3 begins with steady flow that had been allowed to settle out to a consistent temperature and flow condition. Figure 5.3 shows snapshots in time at the beginning, middle, and end of the video T=$0s, 25s, 50s$. For each of the subfigures, the left image shows the vertical component of velocity at that time snapshot, and the right image shows the z-vorticity. These values were averaged over a 0.25s span, which and the time step is shown above each subfigure.

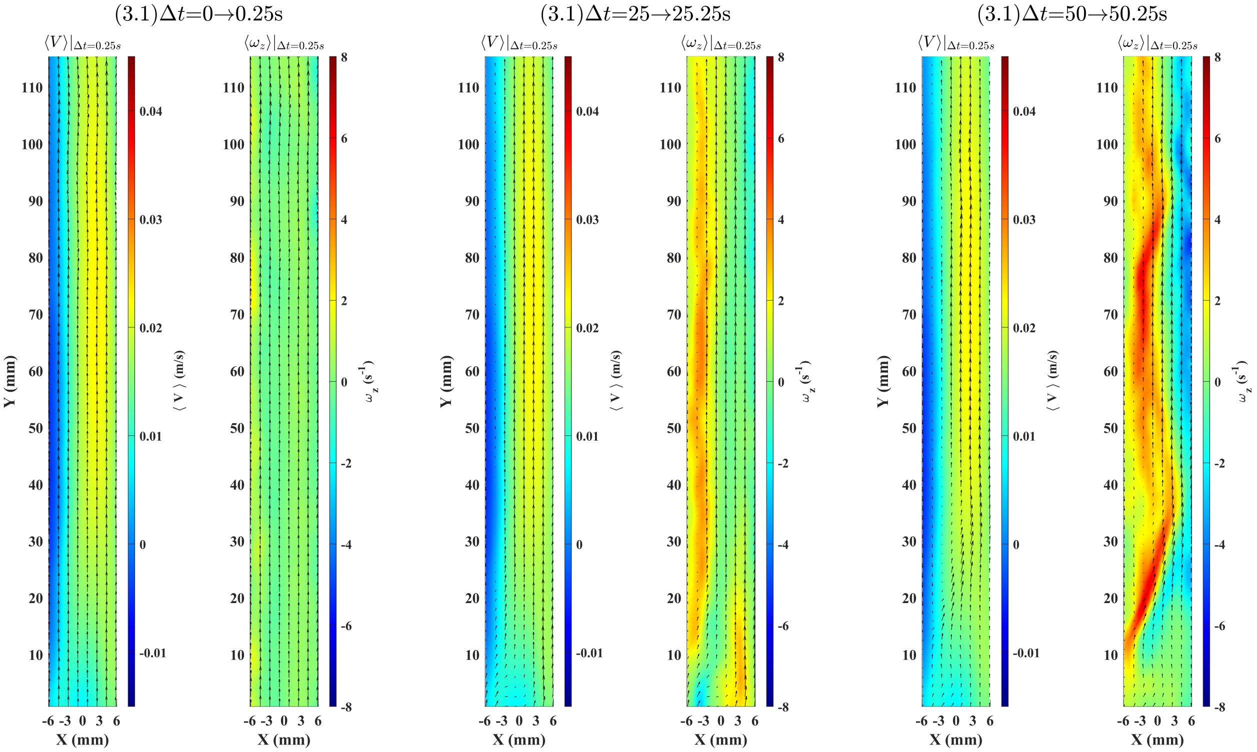

(a) Start of 3.1

(b) Middle of 3.1

(c) End of 3.1

Figure 5.3: Velocity and Vorticity fields for data set 3.1 averaged over a 0.25s span. 5.3a begins at insulation removal, and 5.3b, 5.3c show different times during the video.

Figure 5.3a shows a very uniform z-vorticity at roughly 0 which makes sense for a steady upward flow showing strong natural circulation. As time progresses and heat is lost out of the viewing windows. Non-uniform temperature gradients across the glass test section cause a hot and cold wall to form. The cold wall acts like a brake on the vertical motion of the flow and the flow along the left wall can be seen to slow down as time progresses in Figures 5.3b & 5.3c. Perhaps most interesting is the time dependent behavior of the vorticity. In the beginning, Figure 5.3a shows no vorticity, but Figure 5.3b a small ripple is seen along the left wall, which then grows into a substantial wave that seems to stay connected and traverse the whole length of the test section. This shows the onset of flow instability brought on by the temperature transient.

Since the vorticity field shows the complex flow structures brought on by the flow-instability, a reduced-order (RO) reconstruction of the vorticity field was undertaken. Using the POD analysis outlined in Chapter 4, the vorticity field was decomposed and reconstructed using various numbers of spatial modes. These modes are in decreasing order, the energy containing structures of the flow. The POD mode reconstruction allows modeling of the flow with lower computing time because the small energy containing structures of flow are omitted. As additional modes are added, it is clear that the reconstruction more closely approximates the actual vorticity field.

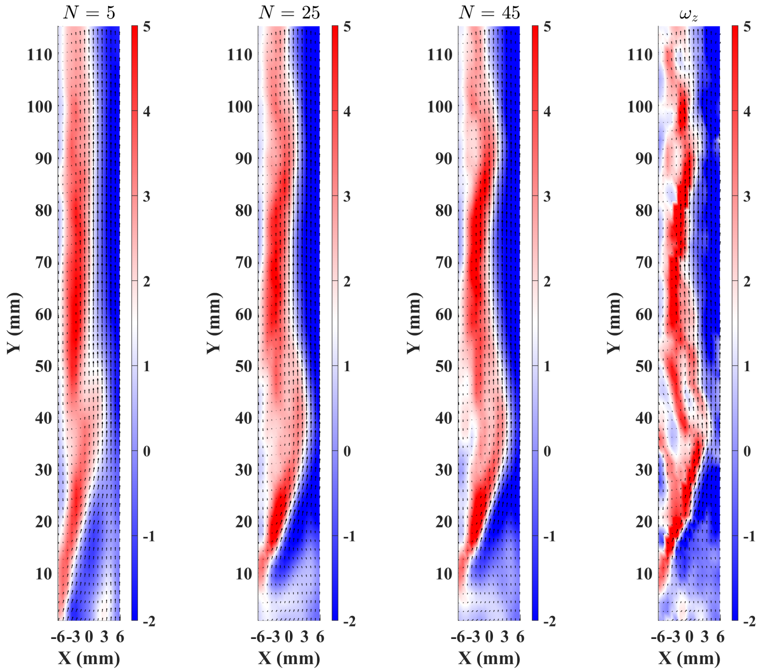

Figure 5.4: ω_z vorticity field reconstruction using N POD modes, shown with the original instantaneous vorticity snapshot at $t = 50.125s$ for Data Set 3.1.

The flow statistics were calculated using the procedure outlined in Chapter 4. Figure 5.5 shows the RMS of the fluctuating components of velocity u' and v'. For the horizontal component, there is a slight increase of this parameter in a jet emanating from the flow outlet. The vertical component shows much more action because the flow is primarily vertical. On the top of the test section, the vertical component is suppressed because the flow being cooled down by the cold wall. This is due in part to the heat guns located below the loop. The Reynolds shear stress shows much higher values for the regions that are primarily holding up the vertical component of flow.

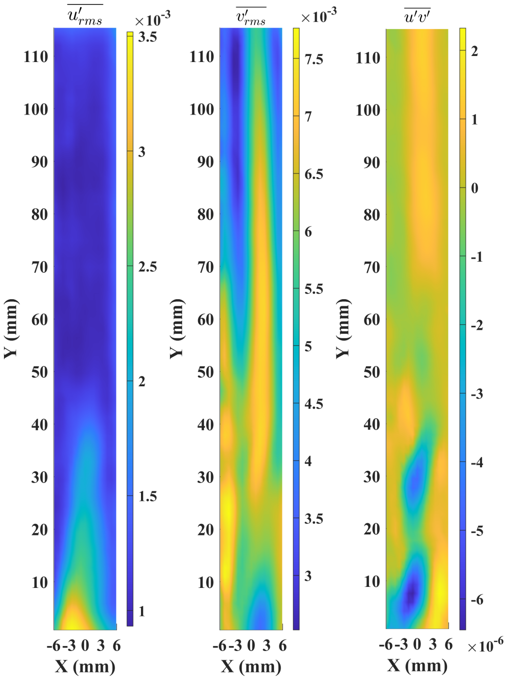

Figure 5.5: RMS u and v velocity components and Reynolds Shear Stress for Data Set 3.1.

5.1.2 Data Set 3.2 Transient Evolution

The second case in data set 3 is very interesting right off the bat. The flow has begun to separate due to the cooling time in Case 3.1 having elapsed. Figure 5.6a shows a clear flow separation on the left and right side, and interestingly enough it is strong enough to even have some flow reversal. A fluid shear boundary layer exists in the middle of the pipe, and is at an angle. The vorticity in Figure 5.6a is similar to the wave shape that was seen in Figure 5.3c. The vorticity layer seems to be connected and it bounds the stagnation layer. This makes perfect sense because in the case of flow reversal the vorticity will be high there.

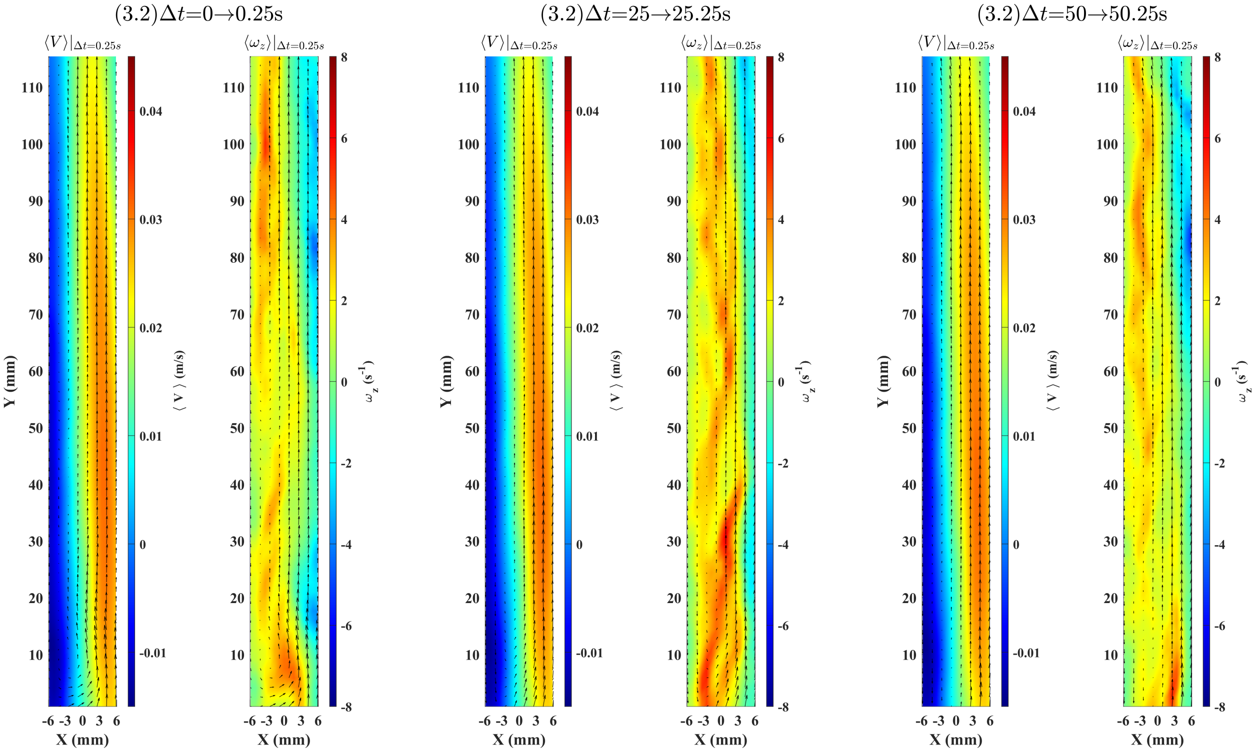
(3.2)Δt=0→0.25s

(3.2)Δt=25→25.25s

(3.2)Δt=50→50.25s

(a) Start of 3.2

(b) Middle of 3.2

(c) End of 3.2

Figure 5.6: Velocity and Vorticity fields for data set 3.2 averaged over a 0.25s span. 5.6a begins at insulation removal, and 5.6b, 5.6c show different times during the video.

Figure 5.6b continues the same evolution, the reverse flow layer can be seen to grow, and the shear layer stays in roughly the same location. The vorticity behavior is interesting because it is still a continuous layer, but the structures are not as large. There exist some small size rippling behavior in the vorticity layer. Finally Figure 5.6c whose the mean vertical flow slowing down, and the vortex field start to break down into smaller structures.

The POD reconstruction of the vorticity field was undertaken at the same time-step that Figure 5.6c. The vorticity layer that follows the fluid shear layer is clearly visible, but it is noteworthy because as the vorticity field gains complexity, the POD reconstruction is not as strong at the lower mode numbers than the simpler flow structures. This also makes sense when compared to Figure 5.13, which shows Case 3.2 having a wider kinetic energy distribution across the modes.

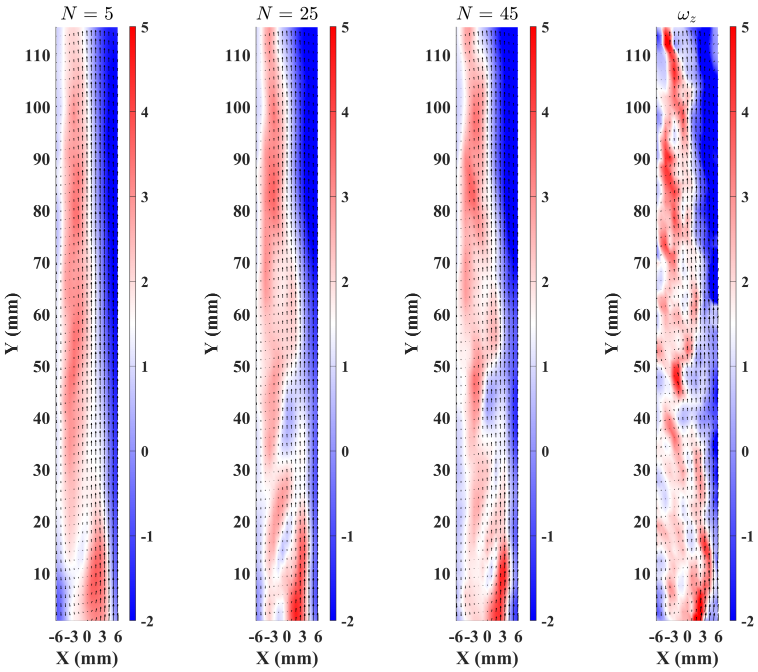

Figure 5.7: ω_z vorticity field reconstruction using N POD modes, shown with the original instantaneous vorticity snapshot at $t = 50.125s$ for Data Set 3.2.

The Reynolds flow statistics were calculated for the RMS for fluctuating velocity components as well as the turbulence strength. Similarly to in Case 3.1 Figure 5.8 shows the horizontal fluctuating component having very small values everywhere except the inlet. The vertical component shows higher magnitude in a jet from the inlet, and the turbulence strength is more uniform than the other two.

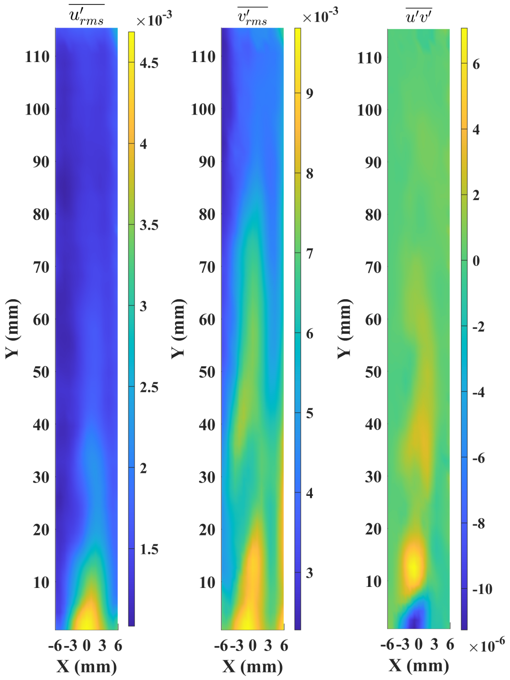

Figure 5.8: RMS u and v velocity components and Reynolds Shear Stress for Data Set 3.2.

5.1.3 Data Set 3.3, Established Unstable Flow

Case 3.3 follows the trend seen in Case 3.1 and 3.2 as a function of time, the mean vertical flow is being impaired by the flow separation and recirculation in the test section which is evident in Figure 5.9. The negative-flow layer continues to grow, and the inlet of the test section has increasingly large area fraction of it undergoing recirculation. This causes an acceleration of the positive velocity component to compensate for the effective loss of flow area, while still maintaining net current in the vertical direction.

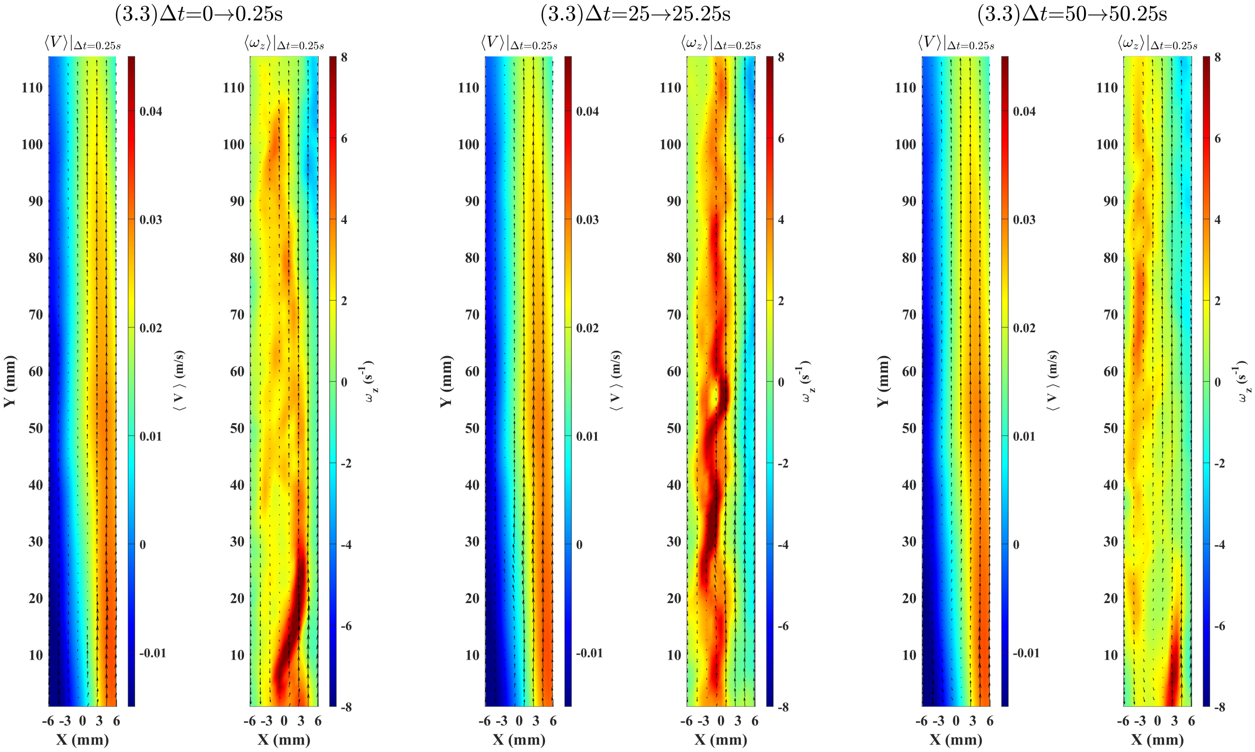

(a) Start of 3.3

(b) Middle of 3.3

(c) End of 3.3

Figure 5.9: Velocity and Vorticity fields for data set 3.3 averaged over a 0.25s span. 5.9a begins at insulation removal, and 5.9b, 5.9c show different times during the video.

The vorticity layer at the end of this case shows very interesting behavior. The vorticity layer in the middle has grown in relation to cases 3.1 and 3.2, and has smaller oscillations. At the end of the case in Figure 5.9c the vorticity layer is fractured and the vortical structures are not as coherent. There still exist some high magnitude vorticity area's which suggest that there are slugs of swirling flow moving through the test section as packets. The inlet shows vortex generation and shedding behavior.

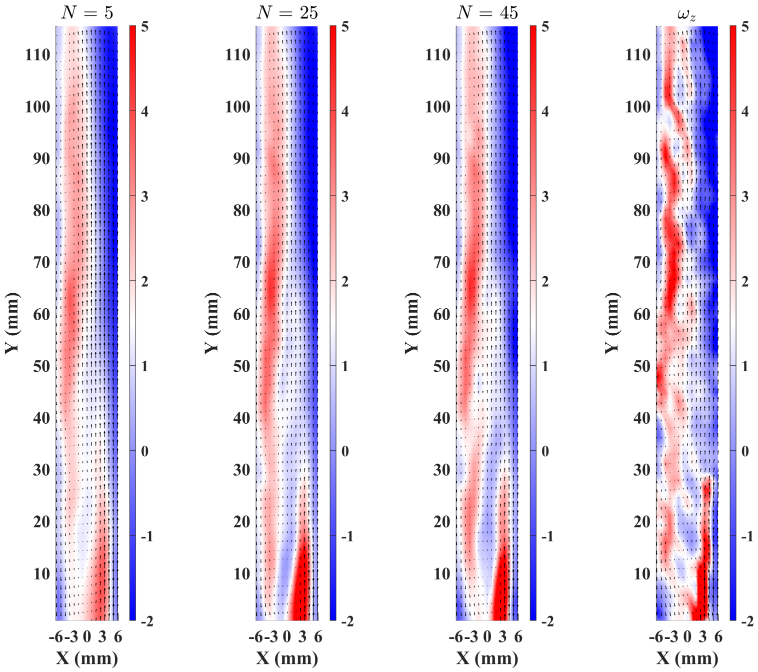

Figure 5.10: ω_z vorticity field reconstruction using N POD modes, shown with the original instantaneous vorticity snapshot at $t = 50.125s$ for Data Set 3.3.

Performing the LO POD reconstruction of the vorticity field for Case 3.3 shows significant improvements as the number of cases moves past 10. The vortex structure in this case is much more complicated than in case 3.1 so even with 45 modes being utilized, the reconstruction misses much of the fine detail.

The Reynolds statistics for case 3.3 show different behavior than the previous cases. There doesn't exist a sharp maximum area in the horizontal fluctuating component, which implies that the variations in horizontal flow decrease, which is interesting since larger vortex behavior is seen in this case. Also, in the vertical component a area of maximum fluctuation exists from the inlet directly to the right of the shear layer. The turbulence stress shows a maximum in a region of the test section where according to the vorticity plot, there exists a void in the center of two vorticies.

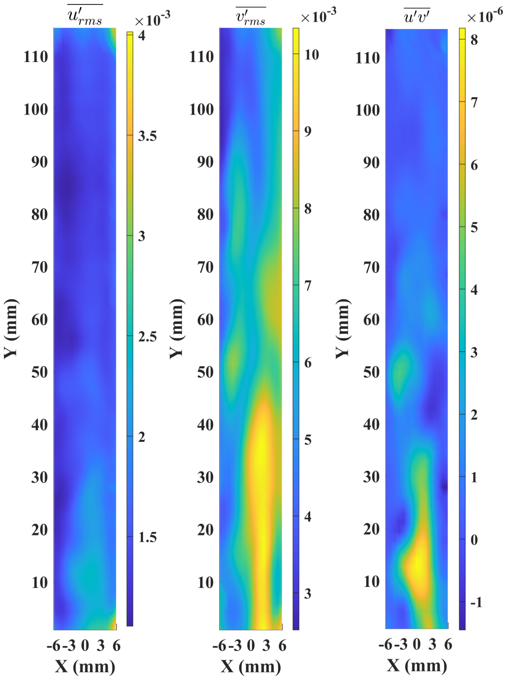

Figure 5.11: RMS u and v velocity components and Reynolds Shear Stress for Data Set 3.3.

5.1.4 Data Set 3 Combined Results

Following the removal of the insulation to initiate the video capture of the flow field for data set 3, the temperature response of the probes was initially stable for $\approx$ 8 seconds. While still in case 3.1, the temperature measurement at the top of the test section started to fall quickly, and all of the temperature probes had settled into an almost linear decrease in temperature. The internal forces on the fluid from the temperature distribution caused the flow to begin to exhibit vortex behavior, which is seen in the later PIV analysis. Roughly halfway through case 3.2 the temperature signal starts to oscillate, which leads to the conclusion that the local flow behavior was very transient. By the middle to end of 3.2, the shear layer had formed, and the cold wall was experiencing reverse flow. The vortex shedding behavior would carry variable temperature salt past the inlet and out probes TP4 and TP5, respectively. To drive the natural circulation, the largest heat addition is the heat guns directly above TP3. Once TP4 reports a lower temperature than TP3, the recirculation in the test section has grown too strong and is forcing cold fluid down into the vertical column. This effectively applies a brake to the natural circulation and halts the flow condition.

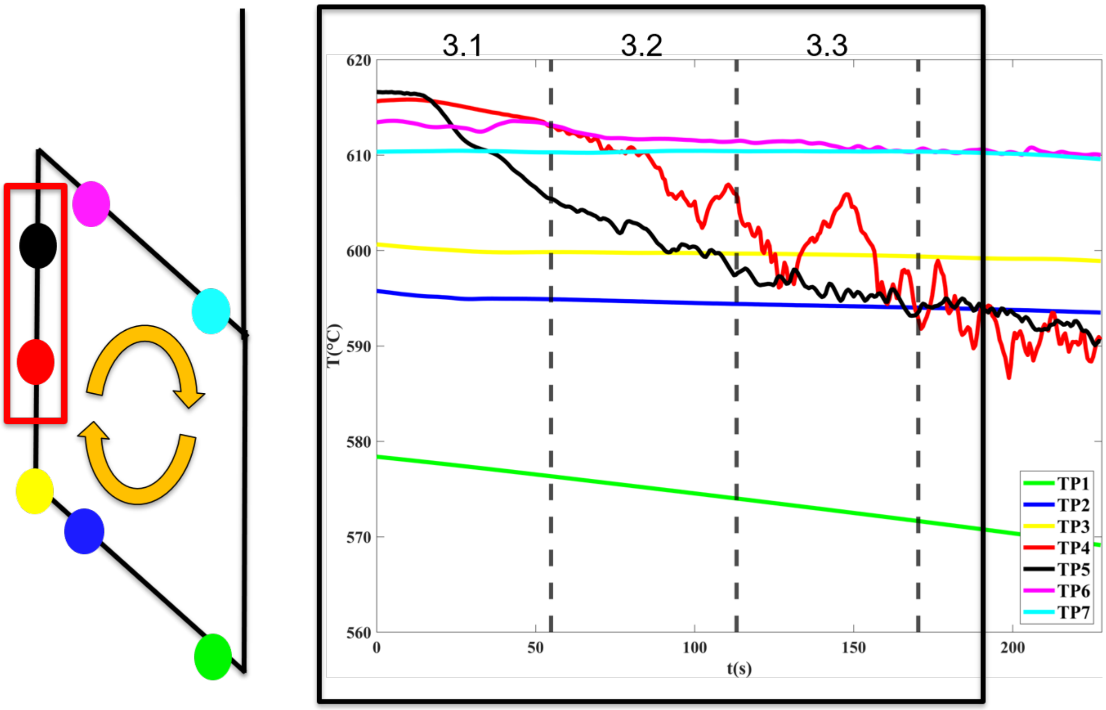

Figure 5.12: Temperature probe response for dataset 3, which was taken as a subset of the test on 02-03-2021

The POD analysis of dataset 3 was conducted on the instantaneous vorticity field. Figure 5.13 illustrates the kinetic energy contained within increasing numbers of the POD modes. The higher magnitude of the case 3.1 POD modes in Figure 5.13a, and the faster decrease of 3.1 in Figure 5.13b show that much more of the energy is contained in the first few modes of this case. This is due to the steady state nature of the first case, and the coherent flow structures contained, as the thermal transient progresses, the flow is disturbed by the density and velocity gradients from the heat losses and more modes are required to effectively capture the flow structure.

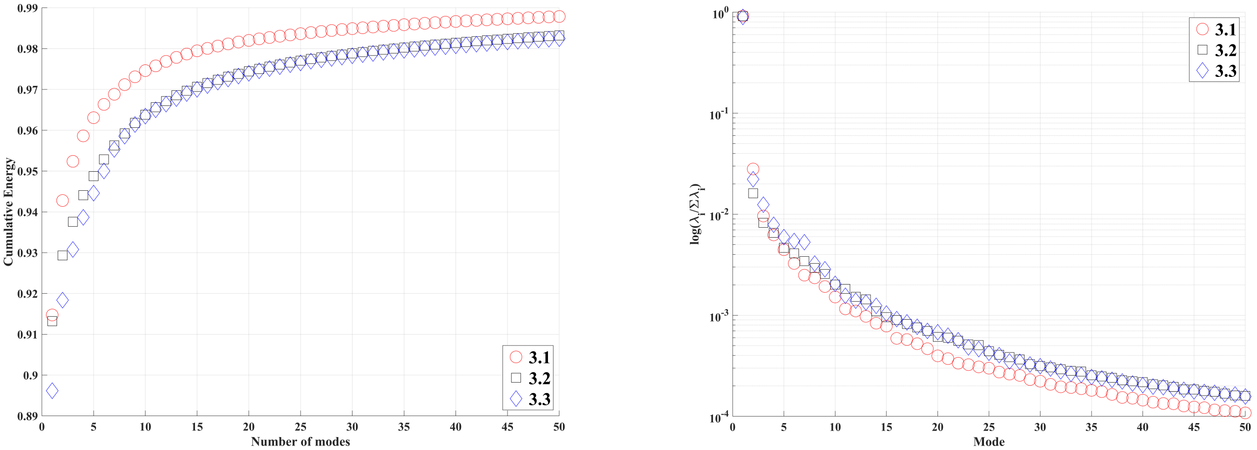

(a) ΣKE of POD Modes

(b) POD mode KE spectra

Figure 5.13: POD mode energy distribution for Data Set 3. 5.13a shows the cumulative energy as a function of POD mode, while 5.13b shows the kinetic energy spectrum of the POD modes.

The PSD for the temporal coefficients is included in Figure 5.14. In each of these cases we can see the turbulence cascade and the $\frac{-5}{3}$ power law in effect. Case 3.1 shows a tendency towards higher frequencies than the other two cases. This is due to the steadier behavior in the flow during the initial flow condition.

The energy dissipation due to the eddy size decrease that we see in Figure 5.14, is also able to seen in Figure 5.15. The vortex centroids refer to the identifed centers of the vorticies for all the cases in dataset 3, and we can see a few things in these figures. First, Case 3.1 has a very tight distribution of the vortex locations and as time goes on to case 3.2 and then 3.3 the distribution of these centers grows. Interestingly, not only does the distribution grow, the highest density area of the distribution moves towards the right of the test section. This occurs due to the fact the left wall was the side of the test section that was exposed to the air with the visualization window being open. So, as the experiment progresses, that wall becomes cooler, and moves the main jet of flow towards the center.

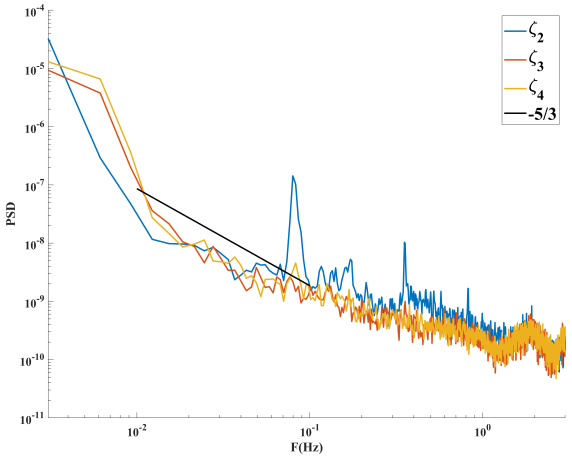

(a) 3.1

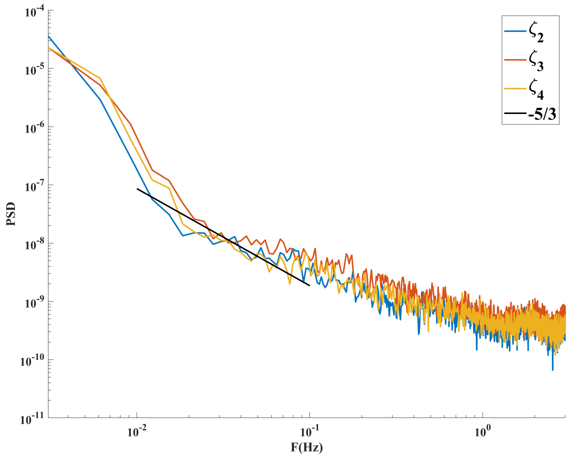

(b) 3.2

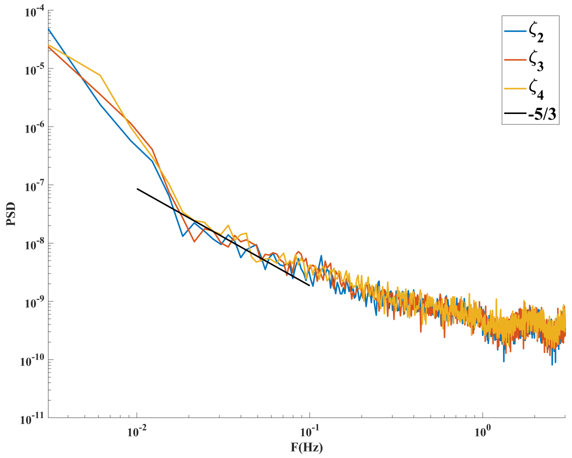

(c) 3.3

Figure 5.14: PSD computed from the POD temporal coefficients $\zeta_1, \zeta_2, \zeta_3$ and the $-\frac{5}{3}$ power dissipation slope shown for the ω_z vorticity fields obtained for Dataset 3

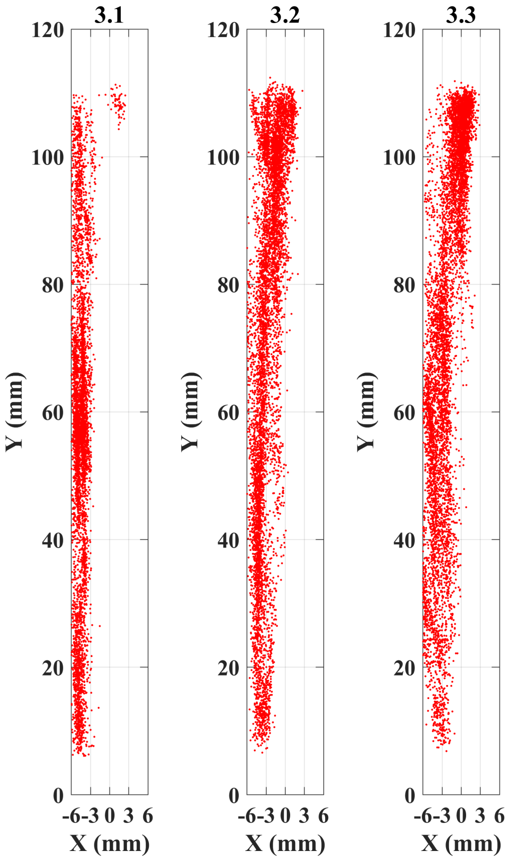

Figure 5.15: Vortex centroid locations for Data Set 3

The qualitative data from Figure 5.15 is shown numerically in Table 5.2,

Case	N_Ω	N_Ω/A_F	μ/D_h^2	σ/D_h^2
3.1	5472	3.95	0.71	0.46
3.2	7482	5.40	0.35	0.22
3.3	7715	5.57	0.36	0.24

Table 5.2: Statistical results vortices identified from PIV velocity vectors for Data Set 3

here we can see the number of vortexes monotonically increase with the cases as time progresses.

As we see in Figures 5.14 & 5.15, the number of vortexes is increasing, and due to the energy dissipation the eddy size is also decreasing. Since turbulence tends towards shorter length scales, this makes sense. The larger vortex eddys are breaking down into smaller vortices which continue this energy transport to smaller length scales. To visualize the change in the size distribution of the vortex behavior, Figure 5.16 contains histograms depicting the distribution of the vortex size. Using cutoff criteria, the vorticies are identified and their size recorded into the respective histogram giving these distributions. As the dataset progresses in cases, the small tail to the right of the distribution starts to dissappear, and in Case 3.3 is minimized.

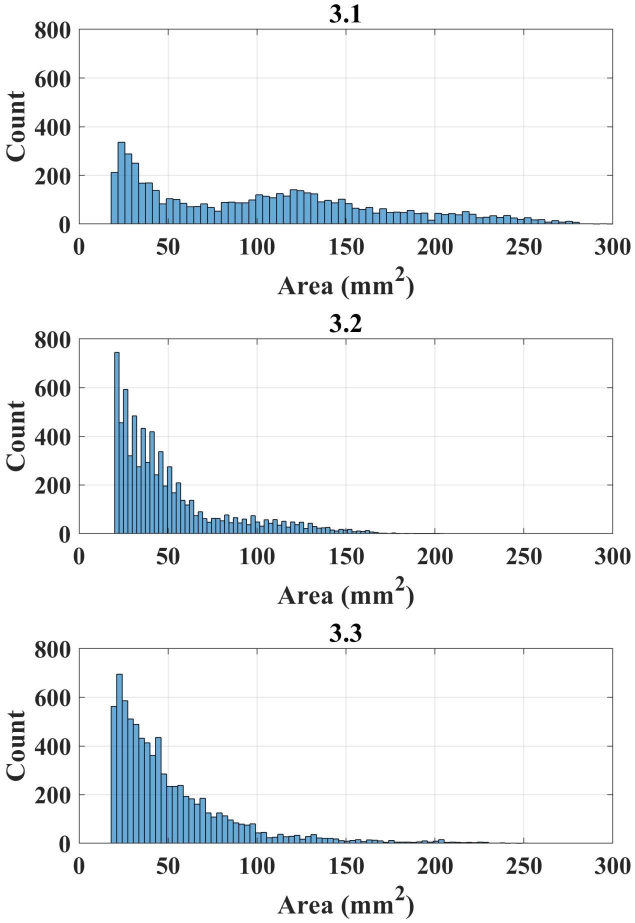

Figure 5.16: Vortex area distribution for Data Set 3

The uncertainty of the first and second order statistics from Reynolds decomposition parameters are defined in Equations 4.22-4.24. In data set 3, there was a marginal increase in uncertainty in these parameters as the normal and shear stresses increased within the flow. As expected, as the magnitude of the stresses increases, the uncertainties increase as well. The largest increase was seen in the Reynolds shear stress which is an indicator of recirculation, which was seen in the vorticity analysis. As recirculation increases more towards the end of the data set, the uncertainty increases as well.

Case	$e_{\overline{u_i}}$	$e_{\overline{v_i}}$	$e_{u_i,RMS}$	$e_{v_i,RMS}$	$e_{\overline{u_i'u_j'}}$
3.1	3.20E-03	1.32E-02	2.30E-03	9.30E-03	2.26E-05
3.2	3.80E-03	1.31E-02	2.70E-03	9.30E-03	3.58E-05
3.3	4.20E-03	1.70E-02	2.90E-03	1.20E-02	4.82E-05

Table 5.3: Uncertainty of first and second order statistics for data set 3.

5.2 Data Set 4

5.2.1 Data Set 4.1 Initially Steady

Data set 4.1 shows the cleanest initial flow conditions out of all of the data sets. The initial and velocity were effectively uniform and the beginning, and as the time with the window was opened increased the cold wall effect began to alter flow. A small vorticity layer can be seen forming in Figure 5.17b, and incrementally growing in size, but definitely in magnitude as can be seen in Figure 5.23c

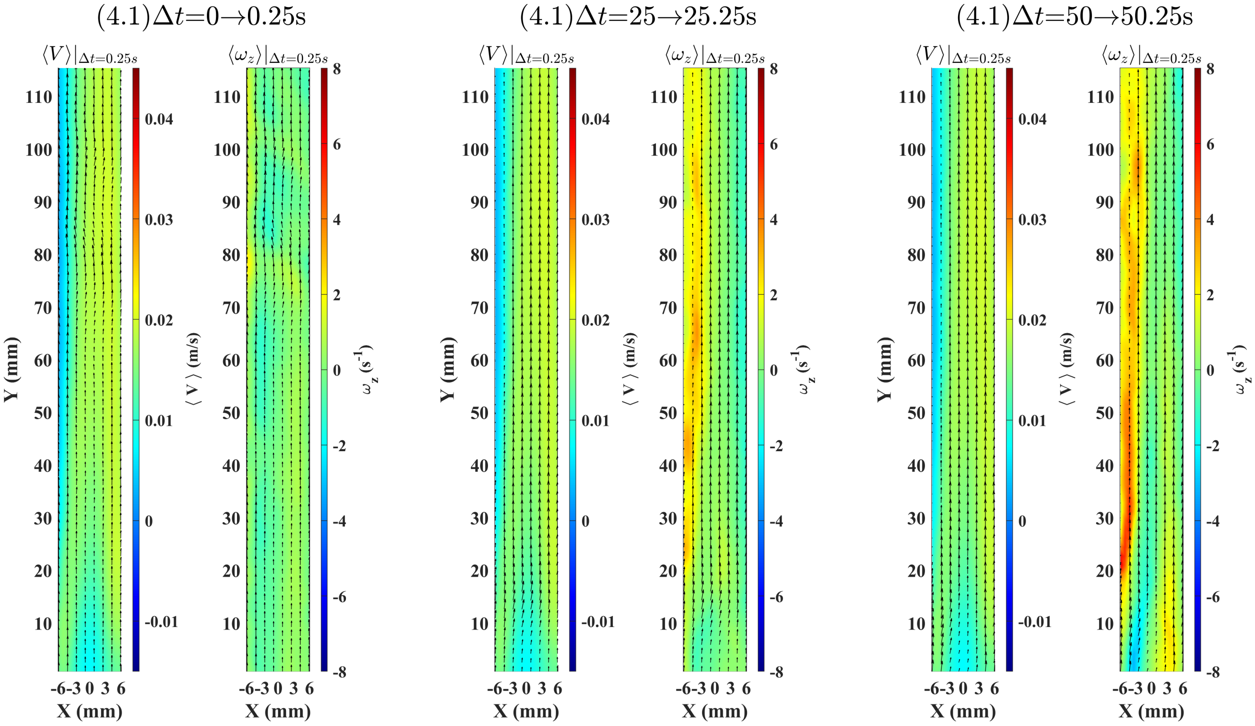

(a) Start of 4.1 (b) Middle of 4.1 (c) End of 4.1

Figure 5.17: Velocity and Vorticity fields for data set 4.1 averaged over a 0.25s span. 5.17a begins at insulation removal, and 5.17b, 5.17c show different times during the video.

Since the flow in Figure 5.17 is consistent, and much of the energy is contained in the first few POD modes, the POD reconstruction of the z-vorticity field worked well for this case. Figure 5.18 shows the incremental increase in the fidelity of the reconstruction compared to the original vorticity field. Qualitatively, it can been seen that the reconstruction works well with all modes, and only misses minor details on the original vorticity field

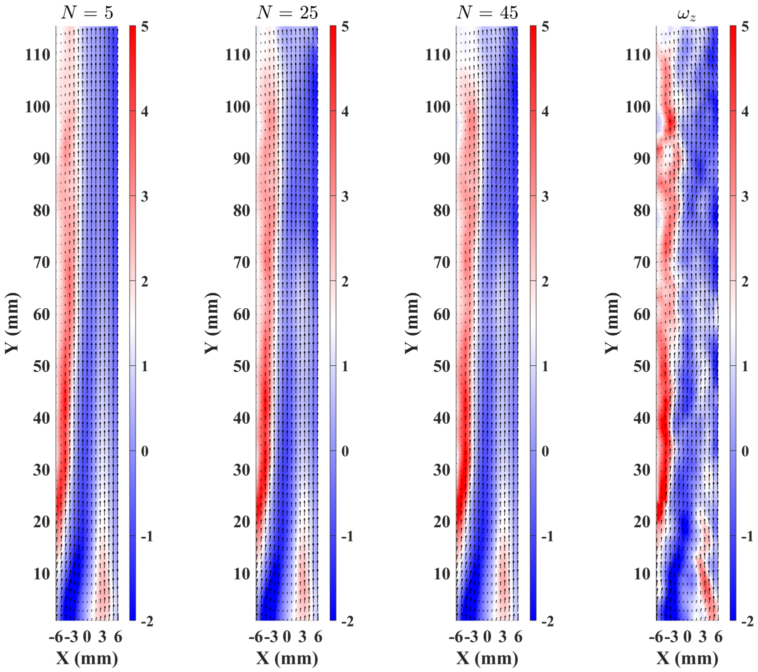

Figure 5.18: ω_z vorticity field reconstruction using N POD modes, shown with the original instantaneous vorticity snapshot at $t = 50.125s$ for Data Set 4.1.

The Reynolds Shear Stress and RMS fluctuating components clearly show that the flow is moving strongly. A stagnation layer forms diagonally from the bottom left corner to the top center for the vertical component, which implies that to the right of it is for positive flow and to the left is the braking flow that will recirculate. They shear stress tells us that there is significant mixing in the fluid as the fluid travels up the test section.

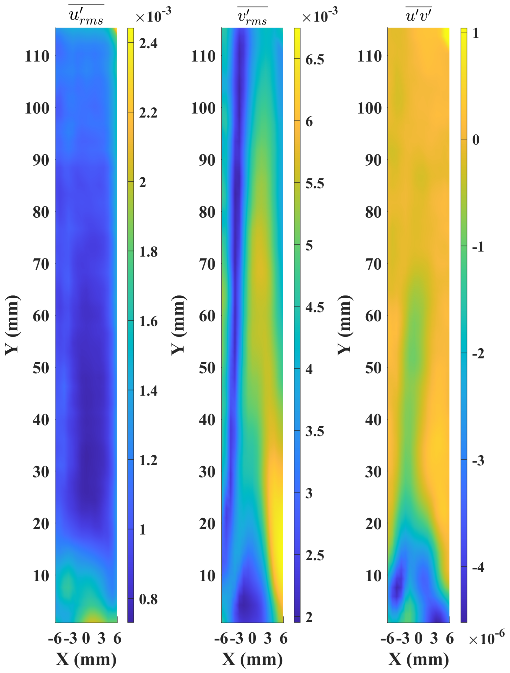

Figure 5.19: RMS u and v velocity components and Reynolds Shear Stress for Data Set 4.1.

5.2.2 Data Set 4.2 Evolution

The transition from the initially quasi-steady case to the stronger transient, the vertical fluid velocity accelerates as the cold wall starts to brake the fluid passing along that wall. This effectively chokes the flow area and forces the flow to accelerate up the hot wall to maintain the flow. The effect of this braking is the shearing between the two fluids that are moving in opposite directions, which induces vortex creation at this interface. In the vorticity fields shown in Figure 5.20, the max vorticity region grows in width and moves more toward the center as the cold wall increases its effect.

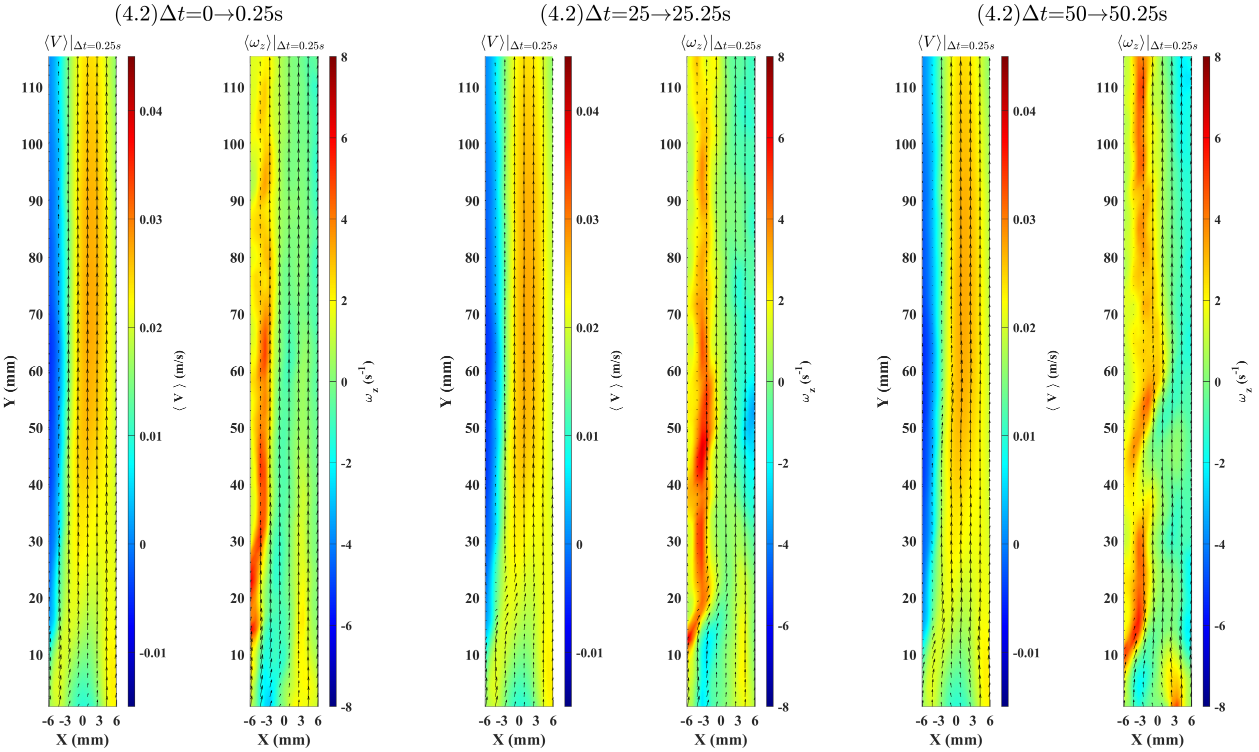

(a) Start of 4.2 (b) Middle of 4.2 (c) End of 4.2

Figure 5.20: Velocity and Vorticity fields for data set 4.2 averaged over a 0.25s span. 5.20a begins at insulation removal, and 5.20b, 5.20c show different times during the video.

The LO reconstruction of the POD fields for Case 4.2 worked well, since there was a clear structure to the flow, much of the energy was contained in these dominant flow structures. This fact allows the flow to be effectively modeled with reduced order modeling. Figure 5.21

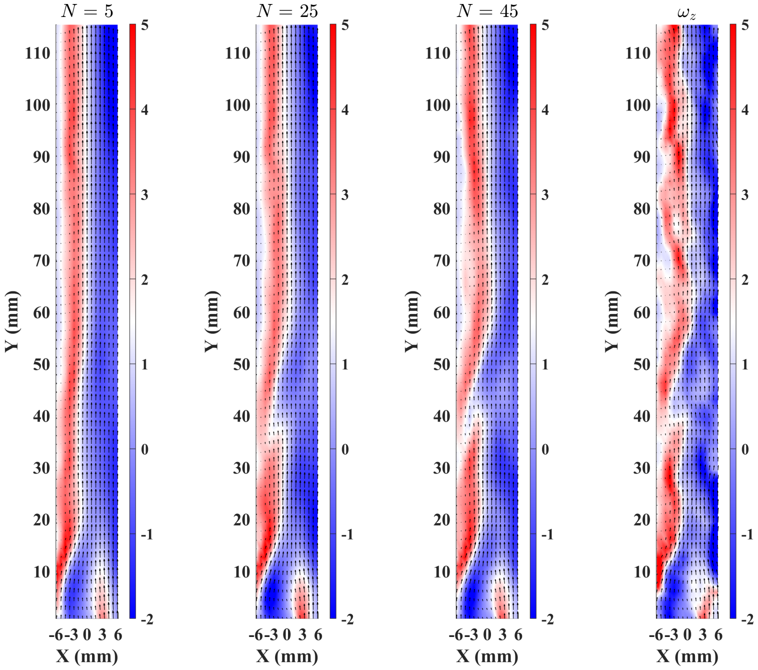

Figure 5.21: ω_z vorticity field reconstruction using N POD modes, shown with the original instantaneous vorticity snapshot at $t = 50.125s$ for Data Set 4.2.

With the strongly positive flow, and the large amount of vortex creation happening in the channel, the Reynolds shear stress is going to be high, as seen in Figure 5.22. The RMS of the fluctuating component show horizontal movement at the base of the shear layer, and significant movement vertically on either size of the shear layer. This makes sense for a region that has a stagnation in the center, and opposing directially fluids on either size of it.

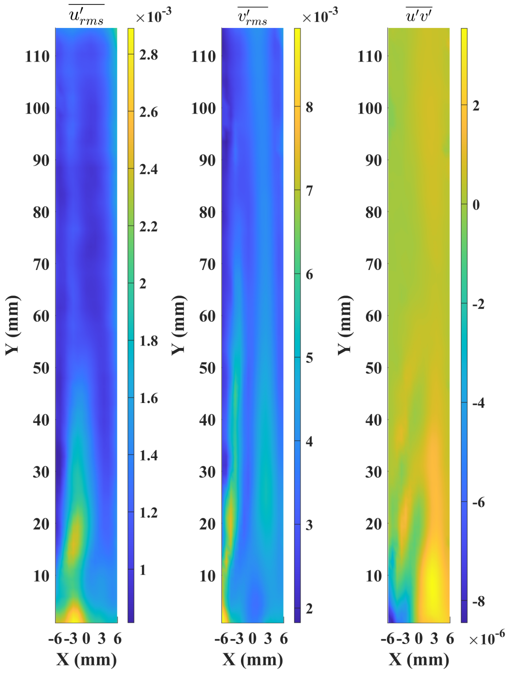

Figure 5.22: RMS u and v velocity components and Reynolds Shear Stress for Data Set 4.2.

5.2.3 Data Set 4.3 Established Unstable Flow

As the flow continues in Data Set 3, the flow maintains its strong net current, so the positive flow must accelerate which we see in Figure 5.23. The velocity boundary layer between the two flow directions can be seen moving back and forth at the inlet, exhibiting flow oscillations, but then the stratified flow corrects its behavior as it moves up the channel. There are local areas of very high vorticity, but they are small. This implies geometrically small vorticies containing significant energy.

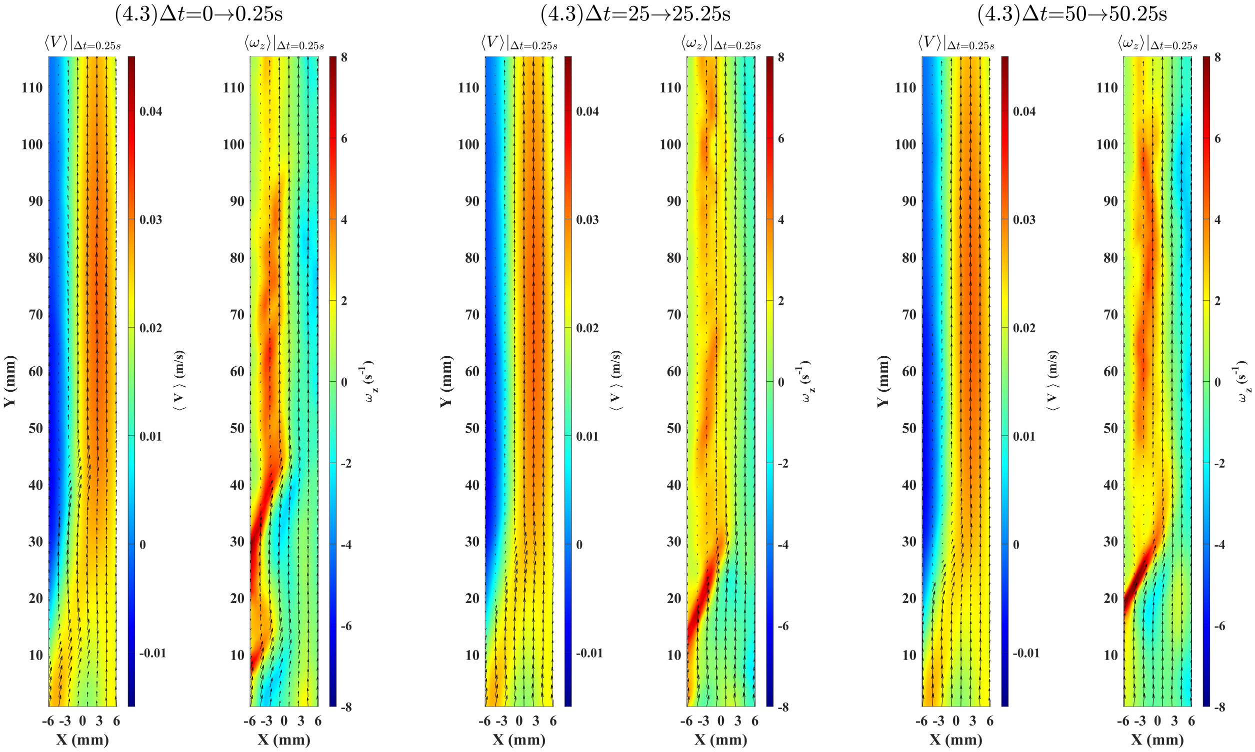

(a) Start of 4.3
(b) Middle of 4.3
(c) End of 4.3

Figure 5.23: Velocity and Vorticity fields for data set 4.3 averaged over a 0.25s span. 5.23a begins at insulation removal, and 5.23b, 5.23c show different times during the video.

Since the flow in Case 4.3 has clearly defined boundaries with the stagnation layer and the recirculation layer, there are few dominant energy containing structures. These coherent flow structures are captured by the first few POD modes, making the LO POD reconstruction an effective technique. Figure 5.24 shows the clear improvement in the reconstruction with the addition of POD modes. The main structure is clearly visible in the section of Figure 5.24 depicting N=25 modes.

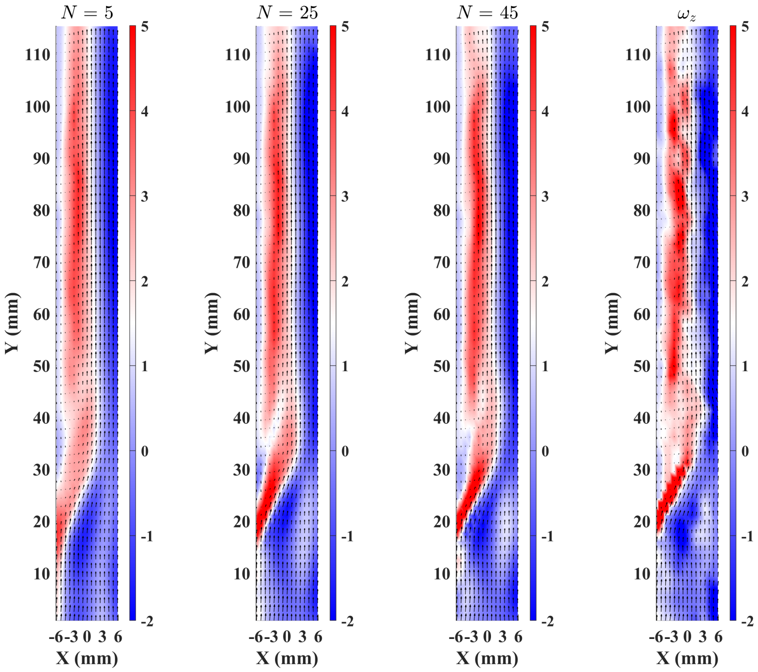

Figure 5.24: ω_z vorticity field reconstruction using N POD modes, shown with the original instantaneous vorticity snapshot at $t = 50.125s$ for Data Set 4.3.

The Reynolds statistics clearly identify the region of very high vorticity with all three parameters studied. The RMS fluctuating components show a high magnitude area at the bottom of the test section in the counter-flow shear boundary layer. The vertical component contains the angle that is seen in the bottom knee area shown in the vorticity plots of Figures 5.23b and 5.23c. The Reynolds shear stress is maximized in the bottom left side of the test section which contains a fast flowing vertical flow section that has the negative flow on top of it. This causes a flow re-direction, yielding high shear stresses. This local flow behavior indicates a very complicated 3D flow, and that the plane of measurements taken only gave a glimpse into a very complex system.

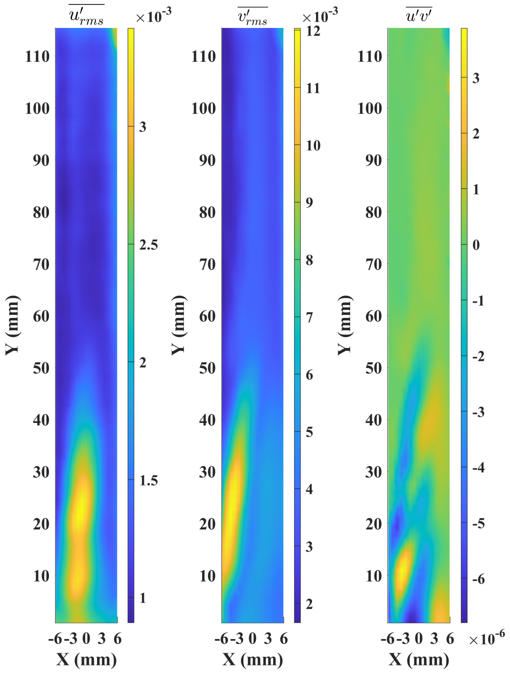

Figure 5.25: RMS u and v velocity components and Reynolds Shear Stress for Data Set 4.3.

5.2.4 Data Set 4 Combined Results

Similar to the other two data sets, data set 4 begins with an almost stable slight cooling, which accelerates $\approx$ 10 seconds into the transient. The cooling rate at the top of the test section again drops off quickly, until about halfway through the second video at which point it levels out at a linear decline. Unique to this case, the test section probes both stayed higher than TP3 for the duration of the test, which is why the strong net current was observed for the entire data set. Interestingly, at the same temporal step where the test section cooling slowed, the probes at TP2 and TP3 saw an increase in temperature. I believe that the recirculation in the test section, with the still positive net current allowed the fluid in the sections of the loop where heat was added in to absorb more heat.

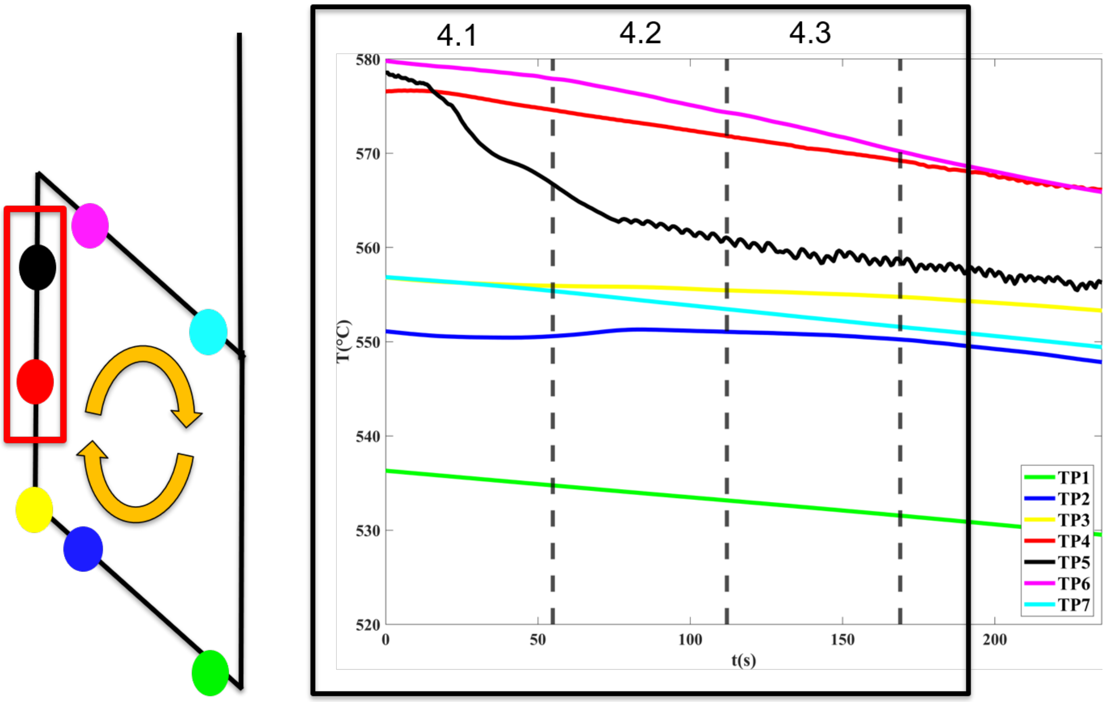

Figure 5.26: Temperature probe response for dataset 4, which was taken as a subset of the test on 02-03-2021

The POD kinetic energy spectra and summation of the kinetic energy shows similar behavior for data set 4 that was observed for data set 3. The first case in the set approaches the asymptotic values the fastest, but in Figure 5.27b, the red indicators for case 4.1 decrease rapidly, but level off unexpectedly.

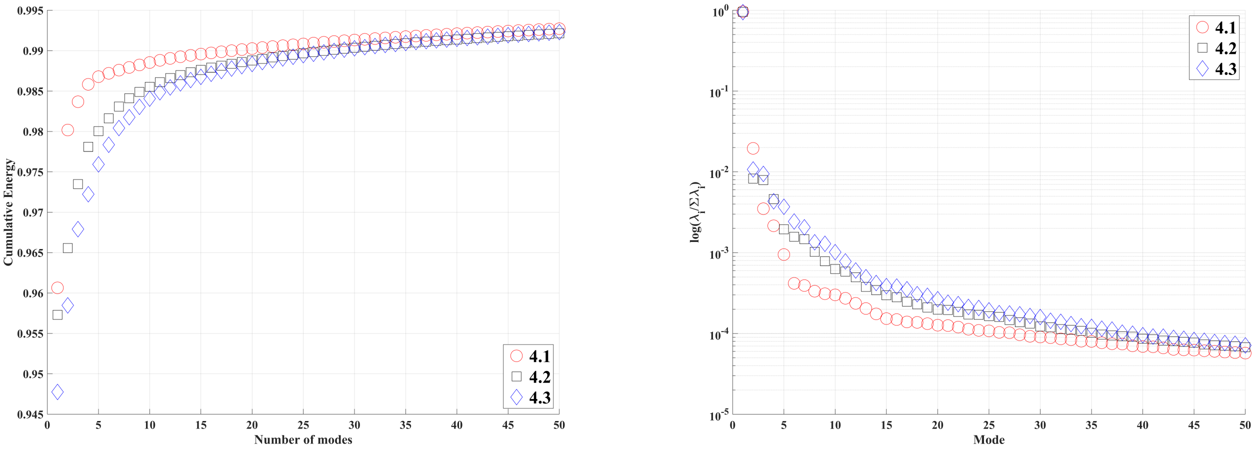

(a) ΣKE of POD Modes

(b) POD mode KE spectra

Figure 5.27: POD mode energy distribution for Data Set 4. 5.27a shows the cumulative energy as a function of POD mode, while 5.27b shows the kinetic energy spectrum of the POD modes.

The PSDs for data set 4, show the expected $\frac{-5}{3}$ power dissipation law, but in this case there exists multiple dominant frequencies. In case 4.1, two dominant frequencies for one temporal coefficient. In case 4.2 there were a few peaks but it wasn't as clean. Case 4.3 shows a collapsing of the dominant frequencies so that all three modes were in sync. These dominant frequencies likely contributed to the extended evolution of the vortex are distribution.

For data set 4, the vortex population and distribution are similar to data set 3. Following the initialization of the case the number of vorticies increases, and their size decreases. This follows along with kinetic energy dissipation, and the complexity introduced by the thermal transient. The growth of the vortex population is higher than in data set 3, and their spatial distribution is much smaller.

Case	N_Ω	N_Ω/A_F	μ/D_h^2	σ/D_h^2
4.1	5006	3.62	0.84	0.60
4.2	6022	4.35	0.74	0.37
4.3	7597	5.49	0.50	0.30

Table 5.4: Statistical results vortices identified from PIV velocity vectors for Data Set 4

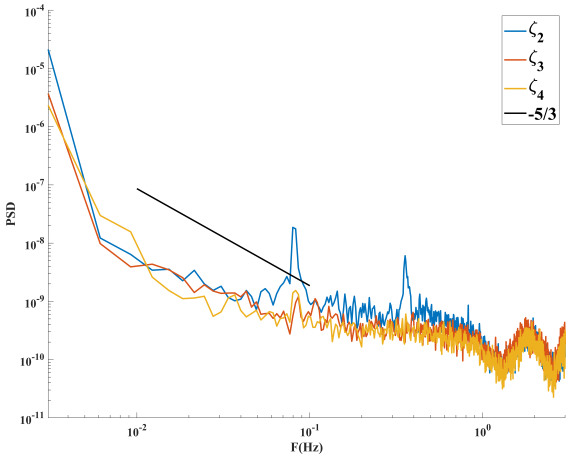

(a) 4.1

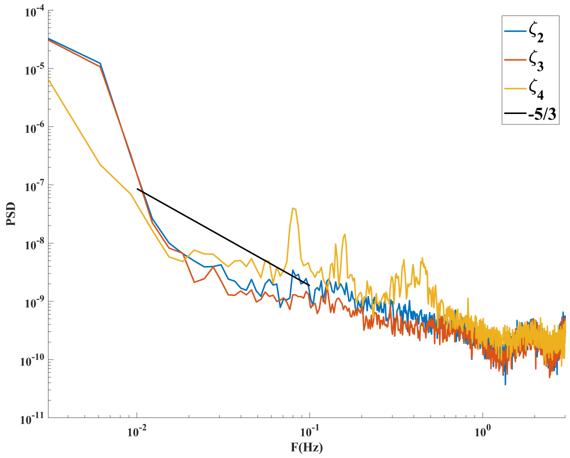

(b) 4.2

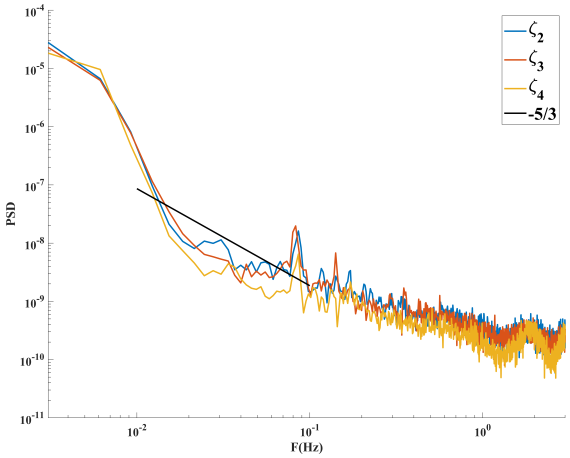

(c) 4.3

Figure 5.28: PSD computed from the POD temporal coefficients $\zeta_1, \zeta_2, \zeta_3$ and the $-\frac{5}{3}$ power dissipation slope shown for the ω_z vorticity fields obtained for data set 4

Interestingly, Case 4.1 exhibits a very tightly distributed vortex patter along the lower left wall, and the upper right center. This tells us a few things, firstly this flow is highly 3D, so many vorticies are moving in and out of the visualization frame. Secondly, with the tightness of these vorticies to the wall, this indicates that the flow was very stable and coherent in the positive direction start.

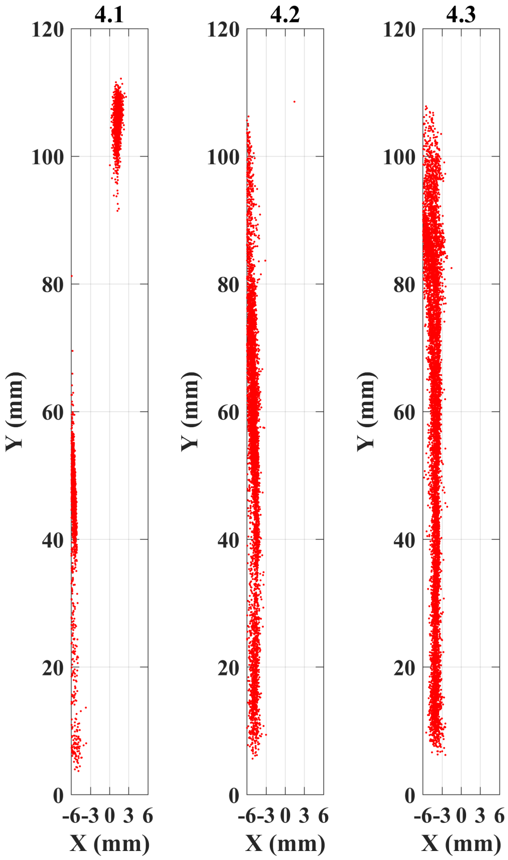

Figure 5.29: Vortex centroid locations for Data Set 4

The distribution width grows in data set 4 as seen before in data set 3. The width of the vortex layer is much smaller in data set 4 though. This can be attributed to the faster average velocity and a much stronger natural circulation. Case 4.3 shows the vortex distribution actually pulling off of the cold wall and moving toward the velocity shear layer where flow recirculation occurs. .

The vortex distribution is not as uniformly distributed that was seen in data set 3. The vortex size distribution was much more bi-modal in this case. As time progressed and the eddys could settle out to smaller and smaller sizes, the distribution moved incrementally towards the exponential decay curve seen in Case 3.3. Case 4.1 is much more bi-modal than case 4.2. In case 4.2 the distribution starts off flatter at the low and high end, which is interesting because it has more vorticies, and the middle of its peaks contains a large number of medium vorticies. Case 4.3 starts to approach the decay curve as seen in data set 3.

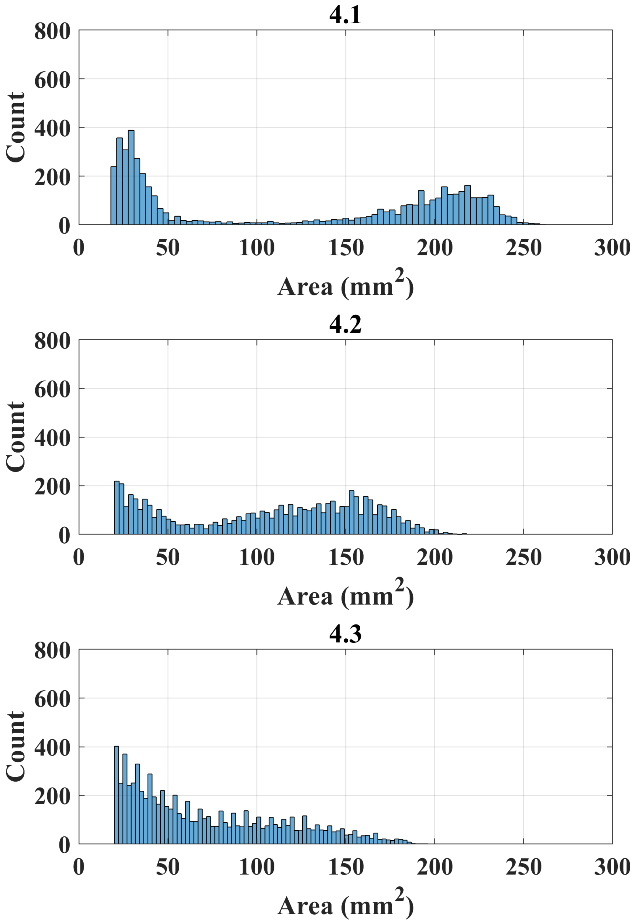

Figure 5.30: Vortex area distribution for Data Set 4

The statistical uncertainties for this data set remained very stable. The velocity magnitudes did not vary to a large degree, so the calculations didnt vary much between cases. The sole uncertainty that saw significant variation is the Reynolds stress uncertainty in Table 5.5. As Reynolds Stress increases due to the strong recirculation about the shear layer, and the vortex shedding the magnitude of the uncertainty likewise increases.

Case	$e_{\overline{u_i}}$	$e_{\overline{v_i}}$	$e_{u_i,RMS}$	$e_{v_i,RMS}$	$e_{\overline{u_i'u_j'}}$
4.1	2.30E-03	9.00E-03	1.60E-03	6.40E-03	1.12E-05
4.2	2.40E-03	6.90E-03	1.70E-03	4.90E-03	1.18E-05
4.3	2.60E-03	7.60E-03	1.90E-03	5.30E-03	1.50E-05

Table 5.5: Uncertainty of first and second order statistics for data set 4.

5.3 Data Set 5

5.3.1 Data Set 5.1 Initially Steady

Similar to Case 3.1, the initial recording shows uniform flow in the positive direction. The magnitude is considerably lower for this case, and the cold wall at the top left side of the test section is visible from the beginning. This is likely due to the shorter wait time for this case to reach steady state, along with the lower average temperature in the loop. The vorticity at the beginning is also nearly zero, which implies a steady upward flow.

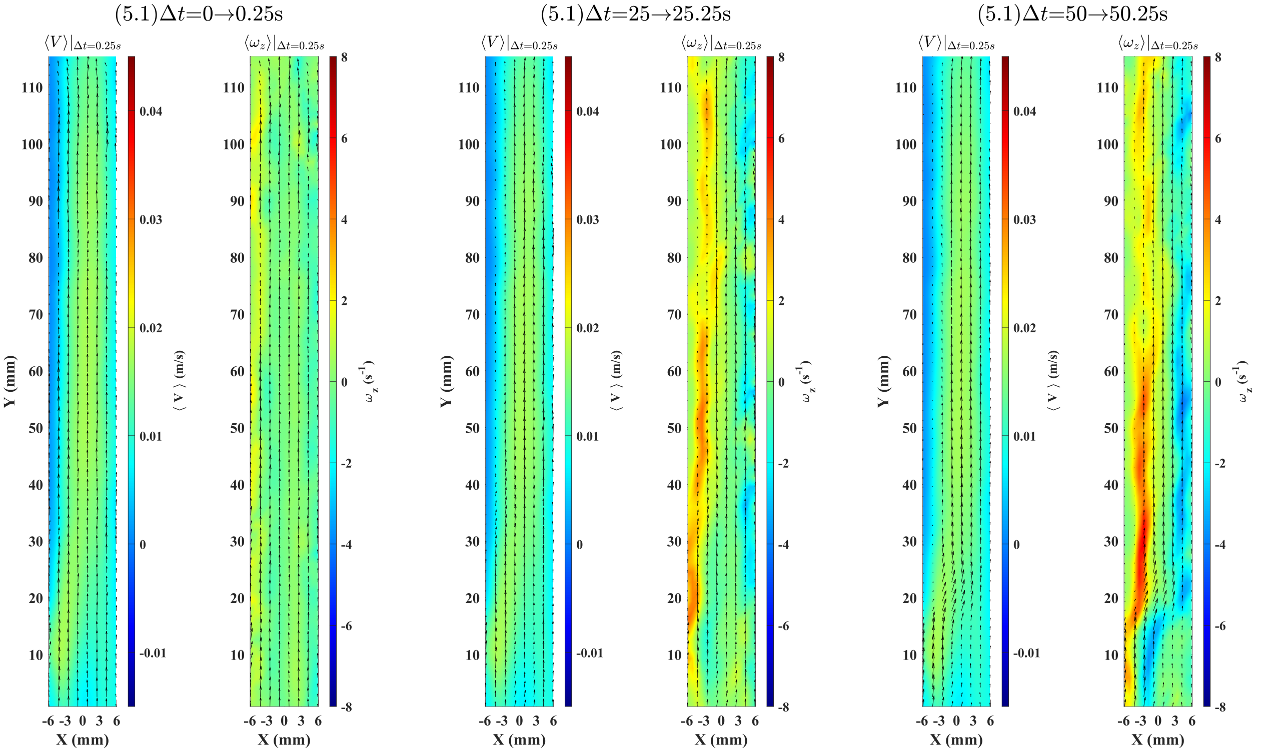
(5.1)Δt=0→0.25s

(5.1)Δt=25→25.25s

(5.1)Δt=50→50.25s

(a) Start of 5.1

(b) Middle of 5.1

(c) End of 5.1

Figure 5.31: Velocity and Vorticity fields for data set 5.1 averaged over a 0.25s span. 5.31a begins at insulation removal, and 5.31b, 5.31c show different times during the video.

As time moves forward though, the same shear layer behavior seen above begins again and vortical structures begin to form along a shear layer near the center of pipe. Interestingly, the right side of the pipe in data set 5 also shows a boundary layer.

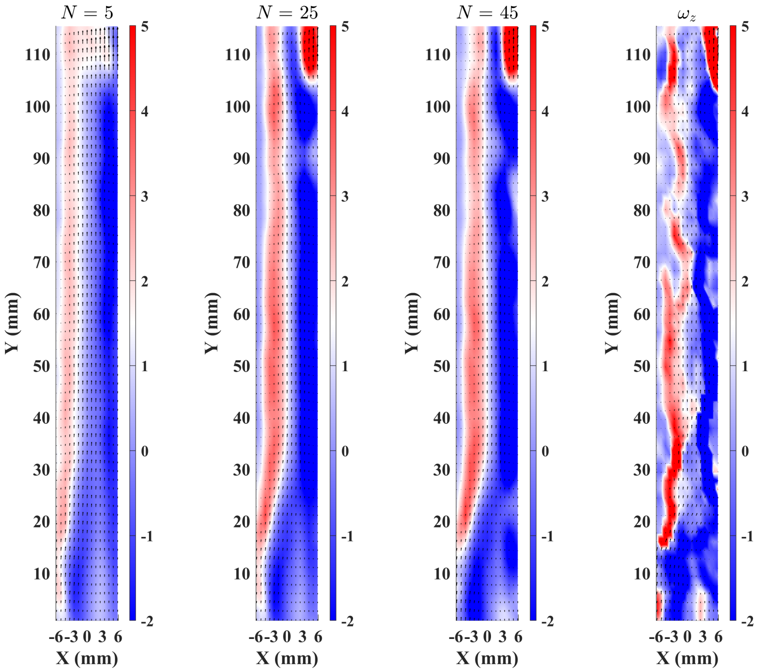

Figure 5.32: ω_z vorticity field reconstruction using N POD modes, shown with the original instantaneous vorticity snapshot at $t = 50.125s$ for Data Set 5.1.

Since the flow in Case 5.1 was slowing down and had much less velocity, the turbulent changes in the flow were lower. This fact is what caused the KE plots in Section 5.3.4 to have be much flatter. Since there were no dominant flow structures, much more of the energy was contained in tiny eddys which is why the LO POD reconstruction misses much of the detail, even with 45 notes.

Perhaps the most illustrative analysis tool for the loss of consistent flow Reynolds statistical parameters. In Figure 5.33, the RMS fluctuating component of the horizontal and vertical velocity vectors are nearly 0 for the entire test region. With these values nearly 0, it is a a strong indicator that the flow is either very statistically consistent which is not likely at such low Re numbers.

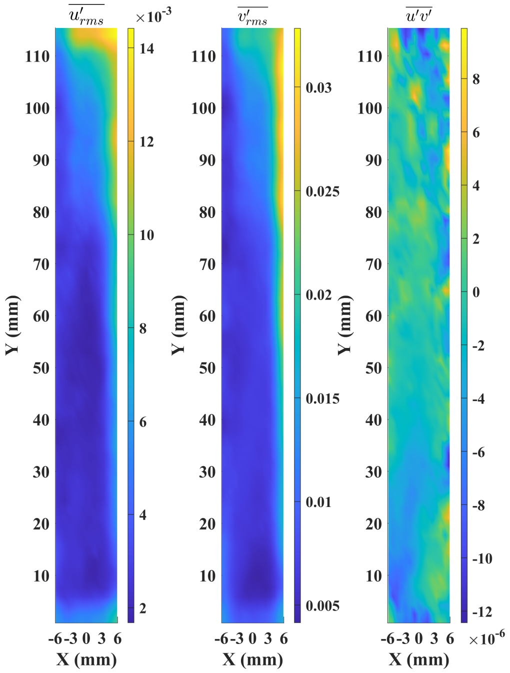

Figure 5.33: RMS u and v velocity components and Reynolds Shear Stress for Data Set 5.1.

5.3.2 Data Set 5.2 Evolution

Following the stagnant case 5.1, Figure 5.34 shows the evolution of the velocity and vorticity field for case 5.2. Figure 5.34a depicts the cold wall on the left side which has been repeatedly seen, and a boundary shear layer traveling up the center of the pipe. As time progresses though, the magnitude of the vorticity in that boundary layer dissipates and the velocity distribution is nearly unchanged. This leads the conclusion that the flow is nearly stagnant in the loop, and that this behavior is from local natural circulation or recirculation within the test section and the visualization region has lost communication with the overall loop.

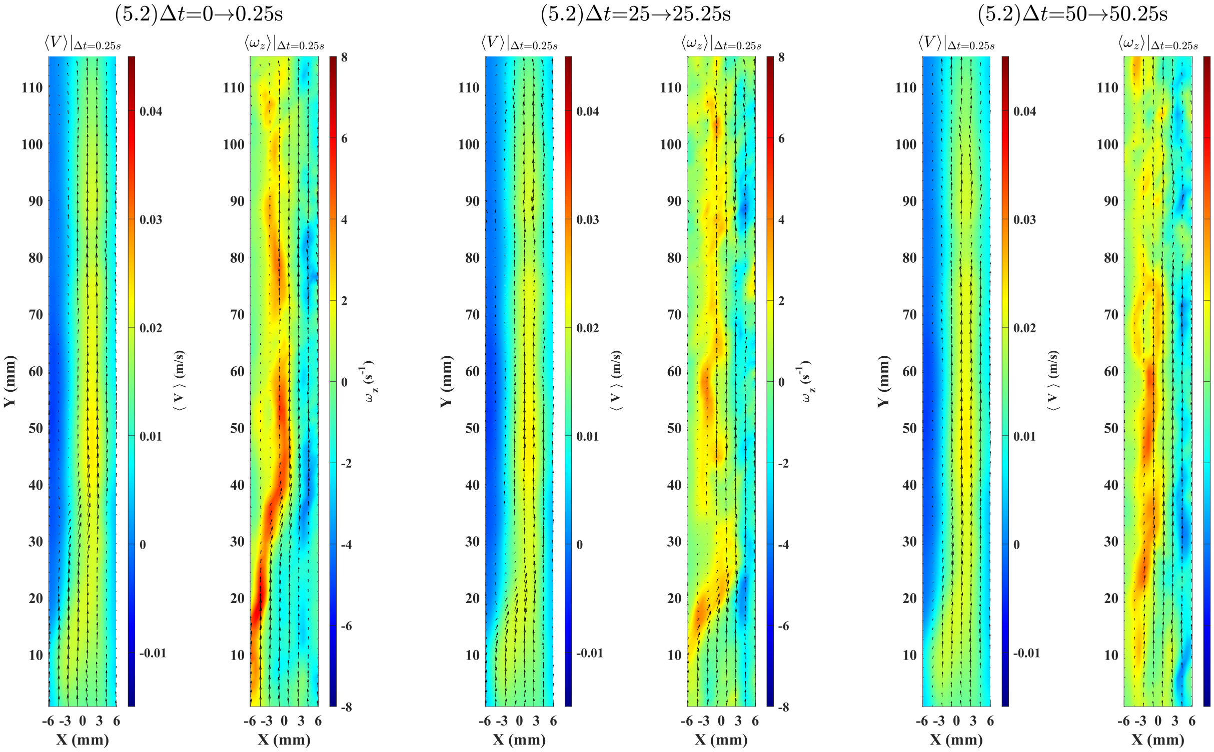

(a) Start of 5.2

(b) Middle of 5.2

(c) End of 5.2

Figure 5.34: Velocity and Vorticity fields for data set 5.2 averaged over a 0.25s span. 5.34a begins at insulation removal, and 5.34b, 5.34c show different times during the video.

Similar to case 5.1, the reconstruction for the POD spatial modes of the vorticity decomposition does not do well for this case. This reconstruction also illuminates the stagnant nature of the flow. Figure 5.35 shows the reconstruction with various numbers of POD modes and the original. There exists much more detail in the original vorticity field, and the reconstruction very coarsely approximates it.

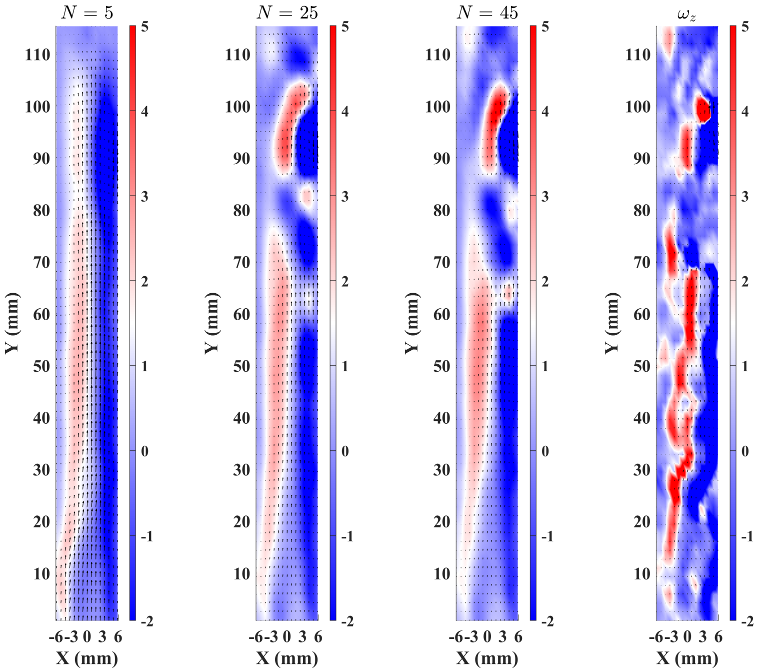

Figure 5.35: ω_z vorticity field reconstruction using N POD modes, shown with the original instantaneous vorticity snapshot at $t = 50.125s$ for Data Set 5.2.

The Reynolds parameters for this stagnant flow are not as interesting as the other cases. The Reynolds Shear Stress is nearly uniform in the test section, and there is a small region where the fluctuating components are non-zero. This is likely a small local recirculating region and not caused by overall bulk flow.

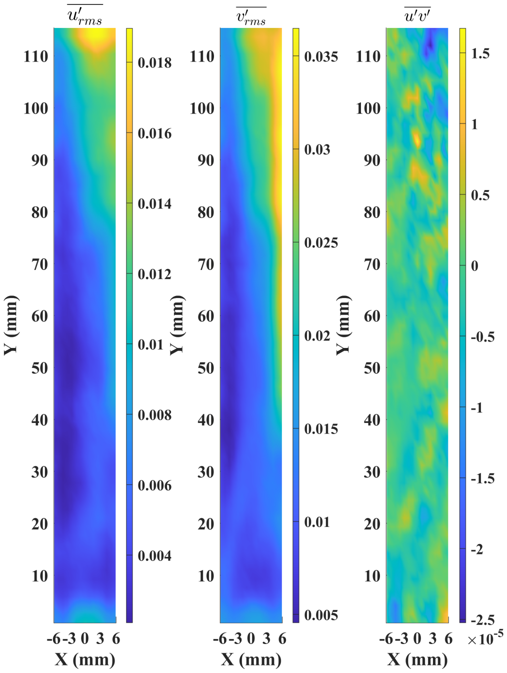

Figure 5.36: RMS u and v velocity components and Reynolds Shear Stress for Data Set 5.2.

5.3.3 Data Set 5.3 Established Unstable Flow

The final time-step analyzed has interesting results. Case 5.3 has the largest flow bifurcation between the hot and cold wall. A small region in the center has some vortex behavior, but they do not dominate the flow, or the energy as they do in the cases with stronger flow. The flow rate calculated for this case is listed in Table 5.1, and was effectively 0.

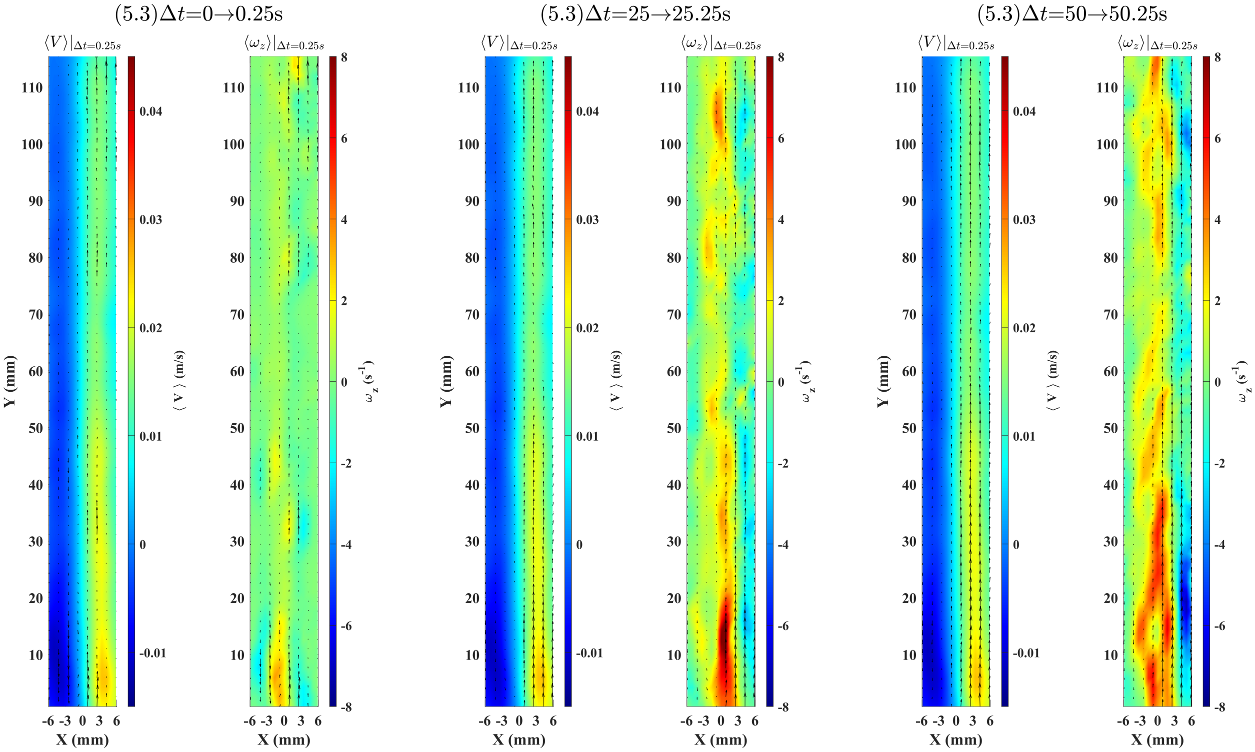

(a) Start of 5.3 (b) Middle of 5.3 (c) End of 5.3

Figure 5.37: Velocity and Vorticity fields for data set 5.3 averaged over a 0.25s span. 5.37a begins at insulation removal, and 5.37b, 5.37c show different times during the video.

Since the flow was so slow and did not have a coherent structure, there are many more flow structures that contribute without the dominant few that follow the flow. This causes the LO reconstruction of the POD vorticity fields to poorly approximate the flow field. Even with 45 modes the reconstruction is poor.

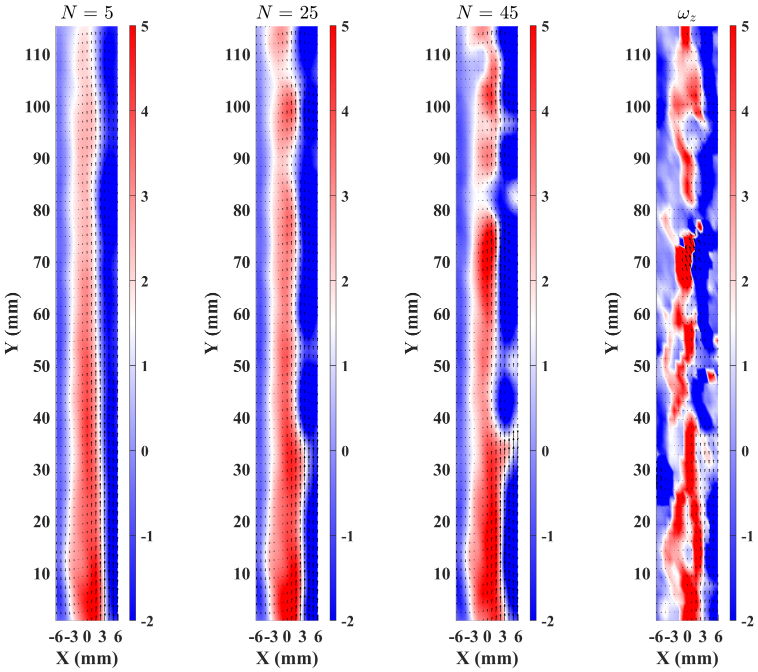

Figure 5.38: ω_z vorticity field reconstruction using N POD modes, shown with the original instantaneous vorticity snapshot at $t = 50.125s$ for Data Set 5.3.

Similar to Case 5.2, the Reynolds Statistical Parameters don't tell us much in this case. The shear stress is nearly uniform at 0, which implies very little variation in flow, and they RMS fluctuating velocity only takes significant values are the top wall, which is most likely a local phenomenon.

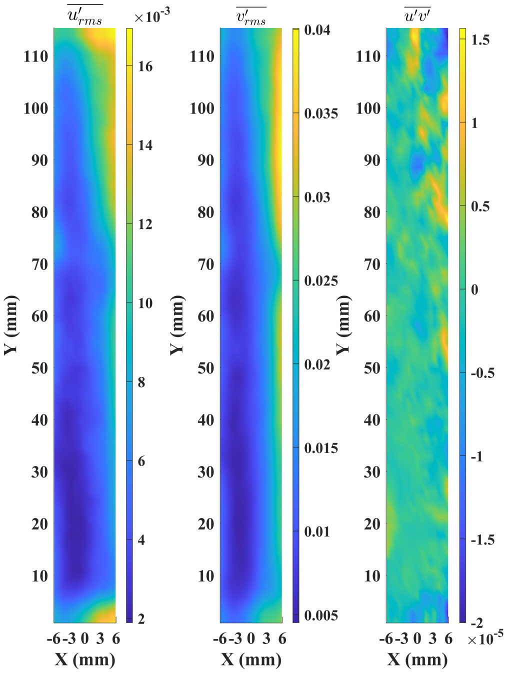

Figure 5.39: RMS u and v velocity components and Reynolds Shear Stress for Data Set 5.3.

5.3.4 Data Set 5 Combined Results

Data set 5 produced a similar thermal response to cases 3.1 and 3.2, where 5.1 and 5.2 shared the initially flat temperature response with TP5 being the highest temperature. After $\approx$ 10 seconds or so, TP5 sees a sharp drop in temperature until roughly the end of 5.1, at which point both 5.1 and 5.2 see a roughly linear response. Due to technical difficulties, a nearly 4 minute gap exists in the recording between 5.2 and 5.3, the temperature response shows some transient behavior in the middle of that gap, but from 250 seconds towards the end, both TP4 and TP5 are lower temperature than TP3 which implies that the natural circulation is ceased. The probes see wild oscillations which can be attributed to the local recirculating fluid in the test section.

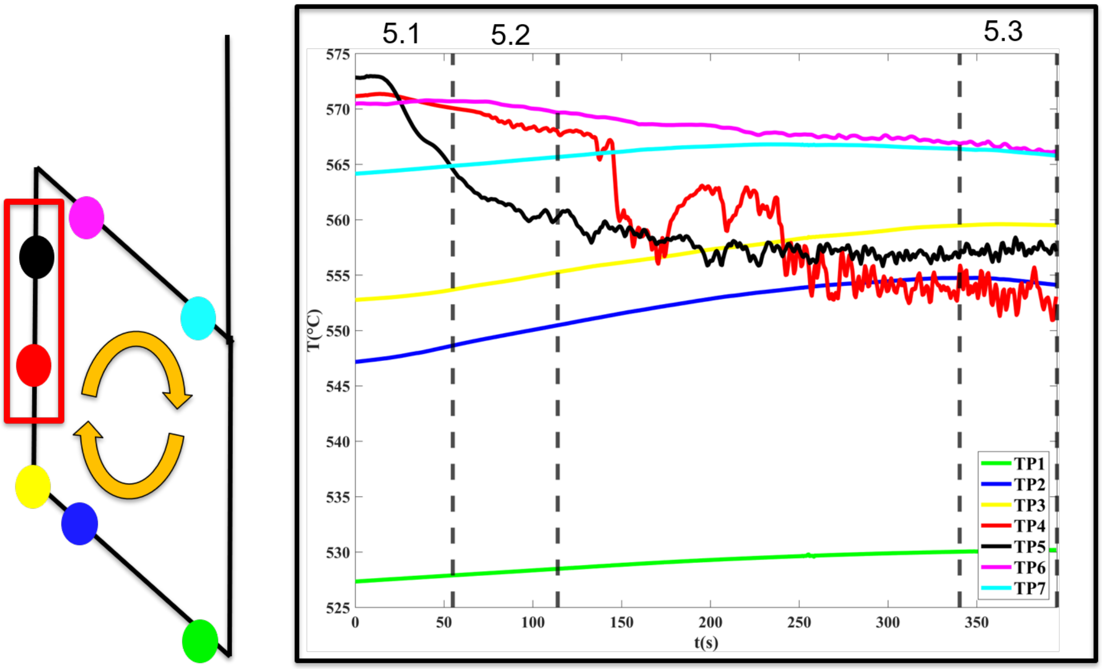

Figure 5.40: Temperature probe response for data set 5, which was taken as a subset of the test on 02-03-2021

Data set 5 in shows the flattest response in the KE spectra for the POD spatial modes. The spectra for the various cases were very similar to each other. The flow behavior in this case was substantially different then the other two data sets, and this will be seen repeatedly in the data to come.

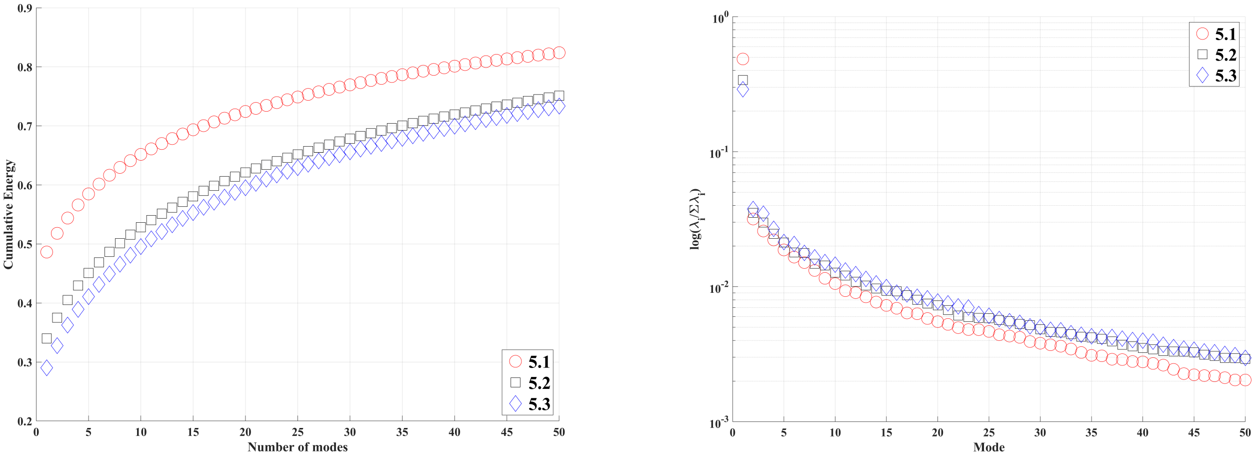

(a) ΣKE of POD Modes (b) POD mode KE spectra

Figure 5.41: POD mode energy distribution for Data Set 5. 5.41a shows the cumulative energy as a function of POD mode, while 5.41b shows the kinetic energy spectrum of the POD modes.

Besides the information in Table 5.1, implying that Data set 5 had lost its self-sustaining natural circulation, the PSD's contained in Figure 5.42a help to confirm this. The only one of the cases that substantially contains the $\frac{-5}{3}$ power law is Case 5.3 and can be seen in Figure 5.42c. Even in this figure, a small region follows this power law, but the other cases within the data set have some issues. The PSD are effectively flat for all frequencies which implies a lack of flow. There are no dominant frequencies which are expected within a flowing system, also, there is no real dissipation. The lack of energy dissipation with the plots being flat are likely a function of noise within the signal.

Data set 5 still has the increase in vortex population as seen before, but the vortex population for data set 3 and data set 4 are significantly higher. If we look at Table 5.1, the velocity of the fluid is lower, and decreasing through the test.

When the vortex centroid locations are identified for data set 5 in Figure 5.43, there is still some structures in the vortex distribution, but there is not the dominant coherence that was seen in earlier cases. The flow was slowing down and the lack of positive net flow allows the vorticies to distribute through the pipe rather than in a layer. The few high density areas of the centroid locations correspond to regions that have previously been likely vortex locations, but data set 5

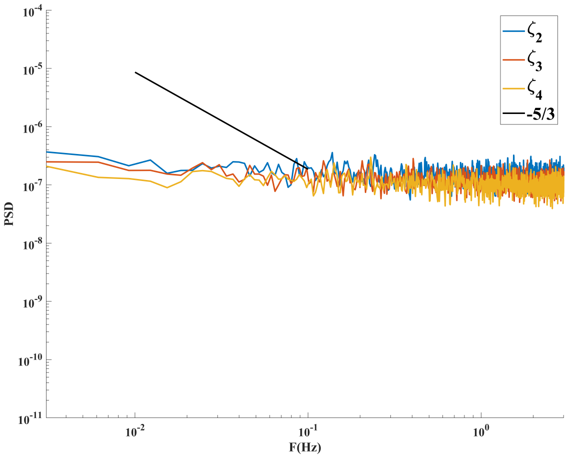

(a) 5.1

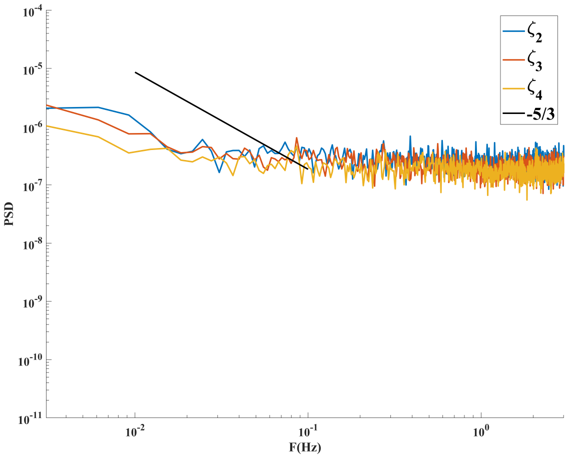

(b) 5.2

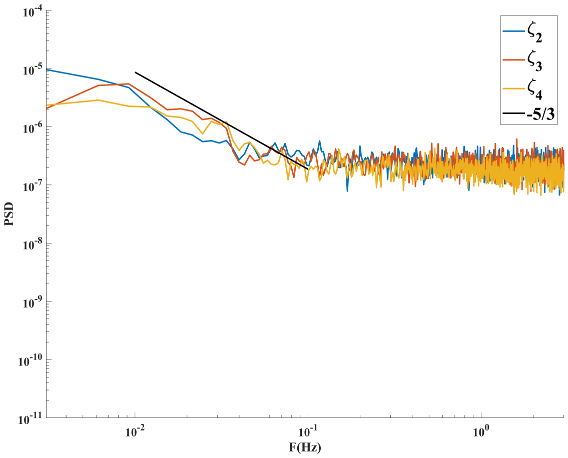

(c) 5.3

Figure 5.42: PSD computed from the POD temporal coefficients $\zeta_1, \zeta_2, \zeta_3$ and the $-\frac{5}{3}$ power dissipation slope shown for the ω_z vorticity fields obtained for data set 5

Case	N_Ω	N_Ω/A_F	μ/D_h^2	σ/D_h^2
5.1	1830	1.32	0.19	0.06
5.2	2181	1.58	0.19	0.06
5.3	2292	1.66	0.19	0.06

Table 5.6: Statistical results vortices identified from PIV velocity vectors for Data Set 5

contains much more vortex activity in the entire test section.

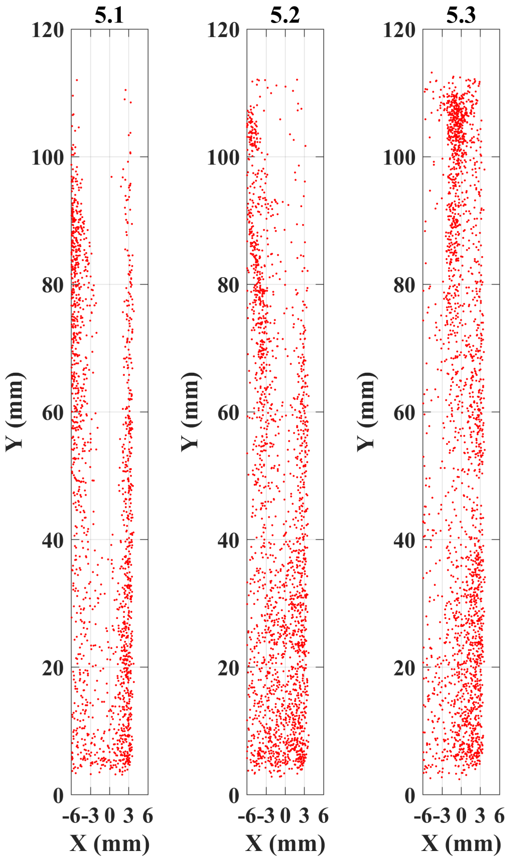

Figure 5.43: Vortex centroid locations for Data Set 5

Even though the vortex are not being co-located like in data set 3 and data set 4, the vortex area distributions start off with the decay curve that was seen at the Case 3.3 and 4.3, since data set 5 does not have a dominant flow structure generating new large vorticies, the system was allowed to dissipate its energy down and populated the lower bins of the histograms.

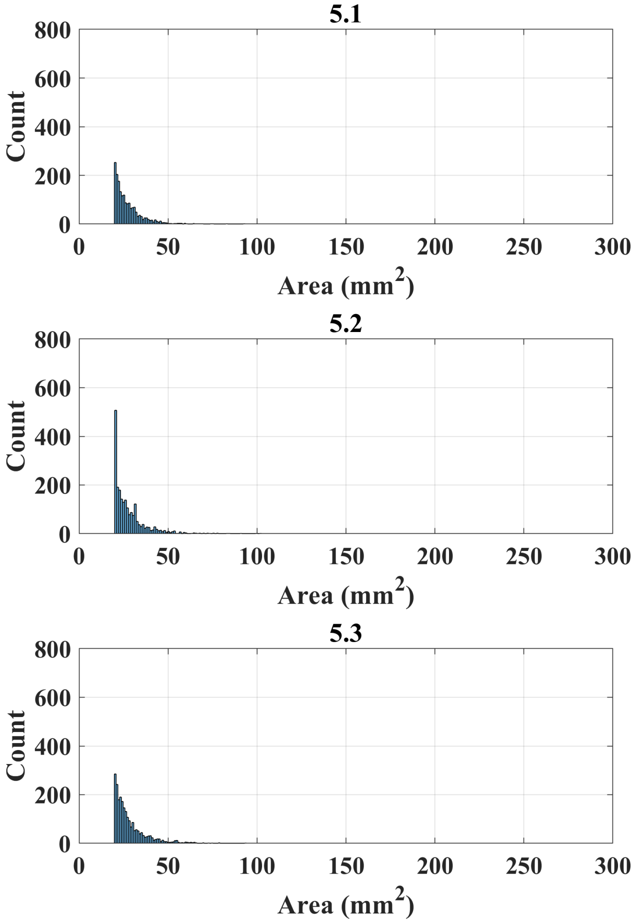

Figure 5.44: Vortex area distribution for Data Set 5

Table 5.7 contains the first and second order statistical uncertainty from the PIV calculation. As the flow begins to break down from 5.1 to 5.2, a 50-100% increase in uncertainty is reported, which then continues again from 5.2-5.3. These large uncertainties owe to the loss of the dominant flow condition. As the flow breaks down and loses its coherent structure the magnitude of the fluctuating components begin to die out, leading to larger uncertainties in the parameters.

Case	$e_{\overline{u_i}}$	$e_{\overline{v_i}}$	$e_{u_i,RMS}$	$e_{v_i,RMS}$	$e_{\overline{u'_i u'_j}}$
5.1	1.23E-02	3.01E-02	8.70E-03	2.13E-02	7.90E-04
5.2	2.00E-02	4.59E-02	1.42E-02	3.25E-02	1.40E-03
5.3	3.00E-02	7.12E-02	2.12E-02	5.04E-02	2.00E-03

Table 5.7: Uncertainty of first and second order statistics for data set 5.

6. CONCLUSIONS

The objective of the work presented was to demonstrate that 2D2C PIV can be effectively used in flowing high-temperature molten salt applications. In this aim, the project was a success. First of a kind data was collected and analyzed, and a procedure was developed for the construction and installation of optically clear piping in a molten-salt loop.

The complexity of the transient flow flow phenomena experienced was a surprise to the researchers, and upon investigation a multitude of analysis techniques were used to understand the evolution of the flow. This unexpectedly complex flow was a both enhances this study, because it shows the applicability of this method in more complex systems, but it also provided some serious hurdles on the construction and operation side that needed to be cleared.

The value of this work lies primarily in the follow-on work that can follow. The expansion of PIV into very-high temperature fluid systems, particularly molten salts offers new and exciting possibilities for researchers as the demand for advanced reactor, and renewable technologies increases. As the safety and reliability of these new systems and designs must be proven, and the computational tools developed, the ability to benchmark and validate complex flow phenomenon in novel fluids with complex behaviors is paramount.

REFERENCES

[1] P. Sabharwall, M. Ebner, M. Sohal, P. Sharpe, M. Anderson, K. Sridharan, J. Ambrosek, L. Olson, and P. Brooks, “Molten Salts for High Temperature Reactors,” Tech. Rep. INL/EXT-10-18090, Idaho National Laboratory, 2010.

[2] R. O. Scarlat and P. F. Peterson, “The current status of fluoride salt cooled high temperature reactor (FHR) technology and its overlap with HIF target chamber concepts,” *Nuclear Instruments and Methods in Physics Research, Section A: Accelerators, Spectrometers, Detectors and Associated Equipment*, vol. 733, pp. 57–64, 2014.

[3] Westinghouse Electric Company, “AP1000 Design Control Document 5 . Reactor Coolant System and Connected Systems,” tech. rep., Nuclear Regulatory Comission, Washington D.C., 2000.

[4] C. W. Forsberg, P. F. Peterson, and P. S. Pickard, “Molten-salt-cooled advanced high-temperature reactor for production of hydrogen and electricity,” *Nuclear Technology*, vol. 144, no. 3, pp. 289–302, 2003.

[5] S. Benhamadouche, “On the use of (U)RANS and LES approaches for turbulent incompressible single phase flows in nuclear engineering applications,” *Nuclear Engineering and Design*, vol. 312, pp. 2–11, 2017.

[6] J. Fang, R. Hu, M. Gorman, L. Zou, G. Hu, and T. Hua, “SAM Enhancements and Model Developments for Molten-Salt-Fueled Reactors,” tech. rep., Argonne National Laboratory, 2020.

[7] X. He, *Validation of the TRACE Code for the System Dynamic Simulations of the Molten Salt Reactor Experiment and the Preliminary Study on the Dual Fluid Molten Salt Reactor*. Dissertation, Technische Universität München, 2016.

[8] L. Zou, D. Nunez, and R. Hu, "Development and Validation of SAM Multi-dimensional Flow Model for Thermal Mixing and Stratification Modeling," tech. rep., Argonne National Laboratory, 2020.

[9] T. K. Tuoc, *TURBULENT TRANSPORT NEAR THE WALL IN NEWTONIAN AND NON-NEWTONIAN PIPE FLOW*. Phd thesis, University of Canterbury, 1992.

[10] Y. A. Hassan and E. E. Dominguez-Ontiveros, "Flow visualization in a pebble bed reactor experiment using PIV and refractive index matching techniques," *Nuclear Engineering and Design*, 2008.

[11] N. Goth, *ANALYSIS OF EXPERIMENTAL PIV/PTV MEASUREMENTS ON A MATCHED-INDEX-OF-REFRACTION 61-PIN WIRE-WRAPPED HEXAGONAL FUEL BUNDLE*. Phd dissertation, Texas A&M University, 2018.

[12] R. Muyshondt, T. D. Nguyen, Y. A. Hassan, and N. K. Anand, "Experimental Measurements of the Wake of a Sphere at Subcritical Reynolds Numbers," *Journal of Fluids Engineering*, vol. 143, no. 6, pp. 1–19, 2021.

[13] K. Yuki, M. Okumura, H. Hashizume, S. Toda, N. B. Morley, and A. Sagara, "Flow visualization and heat transfer characteristics for sphere-packed pipes," *Journal of Thermophysics and Heat Transfer*, vol. 22, no. 4, pp. 632–648, 2008.

[14] M. Delgado, S. Lee, Y. A. Hassan, and N. K. Anand, "Flow visualization study at the interface of alternating pitch tube bundles in a model helical coil steam generator using particle image velocimetry," *International Journal of Heat and Mass Transfer*, vol. 122, pp. 614–628, 2018.

[15] M. Rosenthal, *An Account of Oak Ridge National Laboratory's Thirteen Nuclear Reactors*, vol. 2009. 2010.

[16] L. McNeese, "Molten-Salt Reactor Program," tech. rep., Oak Ridge National Laboratory, 1975.

[17] D. F. Williams, L. M. Toth, and K. T. Clarno, *Assessment of Candidate Molten Salt Coolants for the Advanced High-Temperature Reactor (AHTR)*. No. March, 2006.

[18] N. R. Quintanar, T. Nguyen, R. Vaghetto, and Y. A. Hassan, “Natural circulation flow distribution within a multi-branch manifold,” *International Journal of Heat and Mass Transfer*, vol. 135, pp. 1–15, 2019.

[19] R. Duffey, “Natural convection and natural circulation flow and limits in advanced reactor concepts,” pp. 49–65, 2002.

[20] S. B. Seo, I. C. Bang, H. Ninokata, and A. Cammi, “Application of adjoint-based sensitivity analysis to natural circulation of high-Pr fluid inside heat transport system,” *Nuclear Engineering and Design*, vol. 381, no. June, p. 111349, 2021.

[21] U. Rohatgi and R. Duffey, “Natural circulation and stability in advanced plants: the Galilean law,” *Conf-940518–2*, 1989.

[22] K. Britsch, M. Anderson, P. Brooks, and K. Sridharan, “Natural circulation FLiBe loop overview,” *International Journal of Heat and Mass Transfer*, vol. 134, pp. 970–983, 2019.

[23] A. Srivastava, A. Borgohain, S. Jana, R. Bagul, R. Singh, N. Maheshwari, D. Belokar, and P. Vijayan, “EXPERIMENTAL AND THEORETICAL STUDIES IN MOLTEN SALT NATURAL CIRCULATION LOOP (MSNCL),” tech. rep., BHABHA ATOMIC RESEARCH CENTRE, MUMBAI, INDIA, 2014.

[24] G. L. Yoder, D. Heatherly, D. Williams, J. Caja, M. Caja, Y. Elkassabgi, J. Jordan, and R. Salinas, *Liquid Fluoride Salt Experiment Using a Small Natural Circulation Cell.* No. April, 2014.

[25] L. Chapdelaine, *EXPERIMENTAL AND COMPUTATIONAL STUDY OF STATIC SOLIDIFICATION OF MOLTEN FLUORIDE SALTS FOR REACTOR COOLANT APPLICATION.* PhD thesis, UNIVERSITY OF WISCONSIN-MADISON, 2017.

[26] P. Sabharwall, E. S. Kim, M. Mc Kellar, and N. Anderson, “Process Heat Exchanger Options for Fluoride Salt High Temperature Reactor Piyush Sabharwall,” *Office*, no. April, 2011.

[27] J. Sherwood, “Thermal-hydraulic Optimization of the Heat Exchange Between a Molten Salt Small Modular Reactor and a Super-critical Carbon Dioxide Power Cycle,” 2020.

[28] J. Ambrosek, M. Anderson, K. Sridharan, and T. Allen, “Current status of knowledge of the fluoride salt (FLiNaK) heat transfer,” *Nuclear Technology*, vol. 165, no. 2, pp. 166–173, 2009.

[29] E. S. Chaleff, T. Blue, and P. Sabharwall, “Radiation heat transfer in the Molten Salt FLiNaK,” *Nuclear Technology*, vol. 196, no. 1, pp. 53–60, 2016.

[30] X. Sun, H. C. Lin, and S. Zhang, “Prandtl Number of Different Fluids • Liquid Salts • Water,” 2017.

[31] Y. S. Jeong, S. B. Seo, and I. C. Bang, “Natural convection heat transfer characteristics of molten salt with internal heat generation,” *International Journal of Thermal Sciences*, vol. 129, no. January, pp. 181–192, 2018.

[32] C. Fiorina, A. Cammi, L. Luzzi, K. Mikityuk, H. Ninokata, and M. E. Ricotti, “Thermal-hydraulics of internally heated molten salts and application to the Molten Salt Fast Reactor,” *Journal of Physics: Conference Series*, vol. 501, no. 1, 2014.

[33] O. Arora, B. Lancaster, S. R. Yang, R. Vaghetto, and Y. Hassan, “Advanced flow and temperature measurements in a forced convection molten salt test loop,” *Annals of Nuclear Energy*, vol. 159, p. 108269, 2021.

[34] D. Chavez, O. Arora, D. Holler, R. Vaghetto, and Y. Hassan, “Response time of thermowells for corrosive, high-temperature experiments,” *Transactions of the American Nuclear Society*, vol. 121, no. 2, pp. 1673–1676, 2019.

[35] R. Serrano-ópez, J. Fradera, and S. Cuesta-López, “Molten salts database for energy applications,” *Chemical Engineering and Processing - Process Intensification*, vol. 73, pp. 87–102, 2013.

[36] O. Reynolds, “An experimental investigation of the circumstances which determine whether the motion of water in parallel channels shall be direct or sinuous and of the Society, The Royal Transactions, Philosophical Society, Royalaw of resistance in parallel channels,” *Soci-*

ety, The Royal Transactions, Philosophical Society, Royal, vol. 174, no. 1883, pp. 935–982, 1883.

[37] S. Kline, W. Reynolds, F. Schraub, and P. Runstadler, "The structure of turbulent boundary layers By," *Journal of Fluid Mechanics*, vol. 30, pp. 741–773, 1967.

[38] S. Pope, *Turbulent Flows*. Cambridge University Press, 2000.

[39] A. J. Majda and A. L. Bertozzi, *Vorticity and Incompressible Flow*. Cambridge Texts in Applied Mathematics, Cambridge University Press, 2001.

[40] O. Reynolds, "On the Dynanmical Theory of Incomypressible Viscous Fluids and the Determination of the Criterion," *Philosophical Transactions of the Royal Society of London*, vol. 186, pp. 123–164, 1894.

[41] J. L. Lumley, "The structure of inhomogeneous turbulent flows," *Atmospheric Turbulence and Radio Wave Propagation*, 1967.

[42] P. J. Holmes, J. L. Lumley, G. Berkooz, J. C. Mattingly, and R. W. Wittenberg, "Low-dimensional models of coherent structures in turbulence," *Physics Report*, vol. 287, no. 4, pp. 337–384, 1997.

[43] G. Taylor, "The spectrum of turbulence," *Proc. R. Soc. Lond. A*, vol. 164, pp. 476–490, 1938.

[44] T. Nguyen, R. Vaghetto, and Y. Hassan, "Experimental investigation of turbulent wake flows in a helically wrapped rod bundle in presence of localized blockages," *Physics of Fluids*, vol. 32, no. 7, 2020.

[45] T. Nguyen, R. Muyshondt, Y. A. Hassan, and N. K. Anand, "Experimental investigation of cross flow mixing in a randomly packed bed and streamwise vortex characteristics using particle image velocimetry and proper orthogonal decomposition analysis," *Physics of Fluids*, vol. 31, no. 2, 2019.

[46] S. Lee and Y. A. Hassan, “Experimental study of flow structures near the merging point of two parallel plane jets using PIV and POD,” *International Journal of Heat and Mass Transfer*, vol. 116, pp. 871–888, 2018.

[47] L. Sirovich, “Turbulence and the dynamics of coherent structures. III. Dynamics and scaling,” *Quarterly of Applied Mathematics*, vol. 45, no. 3, pp. 583–590, 1987.

[48] A. Kolmogorov, “Dissipation of Energy in the Locally Isotropic Turbulence,” *Proc*, vol. 434, no. 1890, pp. 15–17, 1991.

[49] P. D. Welch, “The Use of Fast Fourier Transform for the Estimation of Power Spectra: A Method Based on Time Averaging Over Short, Modified Periodograms,” *IEEE Transactions on Audio and Electroacoustics*, vol. 15, no. 2, pp. 70–73, 1967.

[50] D. J. Schneck and F. J. Walburn, “Pulsatile blood flow in a channel of small exponential divergence - Part II: Steady streaming due to the interaction of viscous effects with connected inertia,” *Journal of Fluids Engineering, Transactions of the ASME*, vol. 98, no. 4, pp. 707–713, 1976.

[51] D. Telionis, *Unsteady Viscous Flows*. New York: Springer-Verlag, 1 ed., 1981.

[52] Z. S. She, E. Jackson, and S. A. Orszag, “Intermittent vortex structures in homogeneous isotropic turbulence,” *Nature*, vol. 344, no. 6263, pp. 226–228, 1990.

[53] A. Eckstein and P. P. Vlachos, “Digital particle image velocimetry (DPIV) robust phase correlation,” *Measurement Science and Technology*, vol. 20, no. 5, 2009.

[54] R. D. Keane and R. J. Adrian, “Theory of cross-correlation analysis of PIV images,” *Applied Scientific Research*, vol. 49, no. 3, pp. 191–215, 1992.

[55] J. Westerweel, *Digital Particle Image Velocimetry: Theory and Application*. PhD thesis, Delft University of Technology, 1993.

[56] M. Raffel, C. E. Willert, S. Wereley, and J. Kompenhans, *Particle Image Velocimetry*. Springer-Verlag Berlin Heidelberg, 2 ed., 2007.

[57] C. Tropea, A. Yarin, and J. Foss, *Springer Handbook of Experimental Fluid Mechanics*. Springer-Verlag Berlin Heidelberg, 2007.

[58] A. Gabriele, A. N. Tsoligkas, I. N. Kings, and M. J. Simmons, "Use of PIV to measure turbulence modulation in a high throughput stirred vessel with the addition of high Stokes number particles for both up- and down-pumping configurations," *Chemical Engineering Science*, vol. 66, no. 23, pp. 5862–5874, 2011.

[59] A. A. Campagnole dos Santos, M. Childs, T. D. Nguyen, and Y. A. Hassan, "Convergence study and uncertainty quantification of average and statistical PIV measurements in a matched refractive index 5×5 rod bundle with mixing vane spacer grid," *Experimental Thermal and Fluid Science*, vol. 102, no. May 2018, pp. 215–231, 2019.

[60] C. F. Matozinhos, G. C. Tomaz, T. Nguyen, A. A. dos Santos, and Y. Hassan, "Experimental measurements of turbulent flows in a rod bundle with a 3-D printed channel-type spacer grid," *International Journal of Heat and Fluid Flow*, vol. 85, no. July, p. 108674, 2020.

[61] P. Sabharwall, T. Conder, R. Skifton, C. Stoots, and E. S. Kim, "PIV Uncertainty Methodologies for CFD Code Validation at the MIR Facility," Tech. Rep. December, Idaho National Laboratory, 2013.

[62] A. Sciacchitano, "Uncertainty quantification in particle image velocimetry," *Measurement Science and Technology*, vol. 30, no. 9, 2019.

[63] J. J. Charonko and P. P. Vlachos, "Estimation of uncertainty bounds for individual particle image velocimetry measurements from cross-correlation peak ratio," *Measurement Science and Technology*, vol. 24, no. 6, 2013.

[64] A. Sciacchitano and B. Wieneke, "PIV uncertainty propagation," *Measurement Science and Technology*, vol. 27, no. 8, 2016.

[65] R. J. Adrian, "Particle-imaging techniques for experimental fluid mechanics," *Annual Review of Fluid Mechanics*, vol. 23, no. 1, pp. 261–304, 1991.